Characterization and Modeling of Irradiation Induced Nanoclusters in Ferritic-Martensitic and Zirconium-Niobium Alloys.

A Dissertation
Presented in Partial Fulfillment of the Requirements for the
Degree of Doctor of Philosophy
with a
Major in Materials Science and Engineering
in the
College of Graduate Studies
University of Idaho
by
Saheed Bayonle Adisa

Major Professor: Matthew Swenson, Ph.D.
Committee Members: Indrajit Charit, Ph.D.; Krishnan Raja, Ph.D.; Eric Aston, Ph.D.
Department Administrator: Eric Aston, Ph.D.

December 2020

Authorization to Submit Dissertation

This dissertation of Saheed Bayonle Adisa, submitted for the degree of Doctor of Philosophy with a Major in Materials Science and Engineering and titled "Characterization and Modeling of Irradiation Induced Nanoclusters in Ferritic-Martensitic and Zirconium-Niobium Alloys" has been reviewed in final form. Permission, as indicated by the signatures and dates below, is now granted to submit final copies to the College of Graduate Studies for approval.

Major Professor: _____ Date: _____
Matthew Swenson, Ph.D.

Committee Members: _____ Date: _____
Indrajit Charit, Ph.D.

_____ Date: _____
Krishnan Raja, Ph.D.

_____ Date: _____
Eric Aston, Ph.D.

Department Administrator: _____ Date: _____
Eric Aston, Ph.D.

Abstract

The objective of this dissertation is to characterize, and model irradiation induced solute clustering in commercially ferritic-martensitic alloys (T91, HCM12A, and HT9) and Zr-1 % Nb alloys following ions or neutron irradiations and also to prescribe the required temperature shift for ion irradiations to emulate neutron irradiation. Ferritic-martensitic alloys are irradiated with Fe^{2+} or neutrons to a dose of 3 dpa at 500 °C and 370 °C while Zr- 1 %Nb alloy is irradiated with Kr^{2+} or neutrons irradiated to 5 dpa at 310 °C. Irradiation induced segregation and nanocluster morphology are analyzed using atom probe tomography. The size and number density in each F/M alloys differ with ions or neutron irradiation while the morphology of Nb-rich nanoclusters following Krypton irradiation is comparable to that seen after neutron irradiation. Two distinct models (Cluster dynamic and NHM model) are utilized to simulate nanocluster evolution in F/M alloys and they both predicted a negative temperature shift will be needed for ion irradiation to emulate neutron irradiation damage.

Acknowledgements

This thesis wouldn't have been possible without the contribution of some people whom I appreciate so much and would like to acknowledge.

I would like to express my sincere gratitude to my major supervisor Dr. Matthew Swenson for believing in me from day one. His support, guidance, patience and vast knowledge has been very helpful to the completion of my study. He encourages me when I am down, he literally thought me how to organize my files and keep data, give me a task that I feel it's impossible to accomplish, and he always say he knows I can do it, all these together make me a better scientist today. I would also like to thank Dr, Charit, Dr. Raja, and Dr. Eric Aston for their mentorship, they are always giving me listening ears anytime I need assistance.

I would thank all the team in the Microscopy and Characterization Suite at the Centre for advanced energy studies (CAES). Jatu Burns, I always feel she is the best on the FIB, Megha Dubey she has also been very helpful, she is always worried about my long distance travel from Moscow to Idaho Falls, and Yaqiao Wu, he is a true leader he helped me to understand the LEAP process. I am very grateful to you all.

This research was sponsored in part by the US Nuclear Regulatory Commission Grants NRC-HQ-84-15-G-0025, and supported by the U.S. Department of Energy, Office of Nuclear Energy under DOE Idaho Operations Office Contract DE-AC07-05ID14517 as part of the Nuclear Science User Facilities experiments 13-419, 18-1210, 18-1400, and 19-1765.

Dedication

I dedicate this dissertation to the almighty God who is the author and the finisher of my faith, to my beloved wife, Gbemisola Adisa, my children Obafemi Adisa and Abigail Adisa, and to my parents, Mr & Mrs. Adisa

Table of Contents

List of Tables

List of Figures

Chapter 1: Introduction

The need for the development of advanced nuclear materials bas become very important in order to meet the need of global energy supply, environment, and security. Thorough research and development will help to resolve technical cost, security, safety, and other regulatory issues. The future nuclear reactor will require structural materials that will be able to withstand the aggressive nuclear environment and last longer than today fleet of commercial power reactors. A significant improvement in thermal, chemical, and radiation stability is needed to increase the life of the nuclear reactor to 80-100 years. It is worthy to note that future reactors will operate at higher temperature (up to 700 °C) and will be exposed to more doses (hundreds of dpa) than the current reactors. The combination of high temperature and high doses will pose a challenge to the material performance. It is therefore necessary to develop advance structural materials that will be able to withstand the severe environment. Ferritic-martensitic (F/M) and zirconium-niobium alloys are leading candidate materials for advanced nuclear reactor applications due to their low thermal neutron absorption cross-section, improved irradiation stability and mechanical properties [1,2].

Ferritic-martensitic (F/M) alloys, a b.c.c alloy which includes T91, HCM12A, and HT9 are leading candidates for advanced nuclear reactors due to their low ductile-to-brittle transition temperature (DBTT) shift, high temperature creep resistance, thermal shock resistance, low swelling, and reduced creep rate under 600 °C [1–13]. However, irradiation can cause microstructural changes and the evolution of precipitates such as the Si-Mn-Ni-rich and Cu rich clusters which can become obstacle to dislocation glide leading to irradiation induce hardening or embrittlement [14–19], potentially rendering the alloys

unsuitable for advanced reactor applications. Si-Mn-Ni rich nanoclusters are formed in F/M alloys under irradiation as a result of the coupling between migrating point defects while Cu-rich nanoclusters are formed because of its low solubility in F/M alloys.

The performance of Zr alloys as cladding materials in both light water and heavy water reactor applications is attributed of their low thermal neutron absorption cross-section, good corrosion resistance at high temperature, and high resistance to irradiation induced swelling and creep [21,22]. A recent development of Zr-based alloys containing niobium is based on empirical findings from the performance of earlier alloy systems to improve the resistance to irradiation growth and corrosion. It has been found that alloying with small amounts of niobium (less than 5 wt%) improves the corrosion resistance of the material without increasing the rate of hydrogen pickup [23]. It has been established that irradiation induces Nb-rich precipitates which act as a barrier to the diffusion of point defects and dislocation loops [20]. Therefore, it is important to have a clear understanding of how the microstructures of these alloys will evolve with long-term irradiation.

In order to expedite the understanding of irradiation effects in candidate alloys, charged particle irradiations are frequently used to emulate neutron irradiation damage in candidate materials [21–27] . Charge particle irradiation requires few hours to reach 1 – 10 dpa range while it will take neutrons irradiation 1-3 years to reach a significant damage level. Charge particles irradiation has little or no residual radioactivity and do not require any special instruments or precaution in handling samples, thus saving the cost of irradiation and post-irradiation characterization. However, the dose rate and damage cascade morphologies differ widely between ions and neutrons, and there is a limited understanding of the significance of these physical differences and how they affect resultant microstructures and

mechanical properties of candidate alloys. In a recent analysis of F/M alloys HCM12A, G-phase and Cu-rich clusters were found to be larger in size following ion irradiations to ~3 dpa at 500 °C compared to neutron irradiation at the same temperature and dose as shown in Fig. 1.1 [28]. However, the data is inconsistent with Mansur invariance theory [29] which has been the basis for selecting conditions for charge particles irradiation to emulate neutrons damage for years, which says that higher does rate irradiation requires increase temperature to emulate lower dose rate evolution of defect clusters. The invariance theory might be true for defects cluster and not for solute clusters. Therefore, it is important to understand the conditions that will be required for ion irradiation to reasonably emulate neutron irradiation with reference to solute clusters.

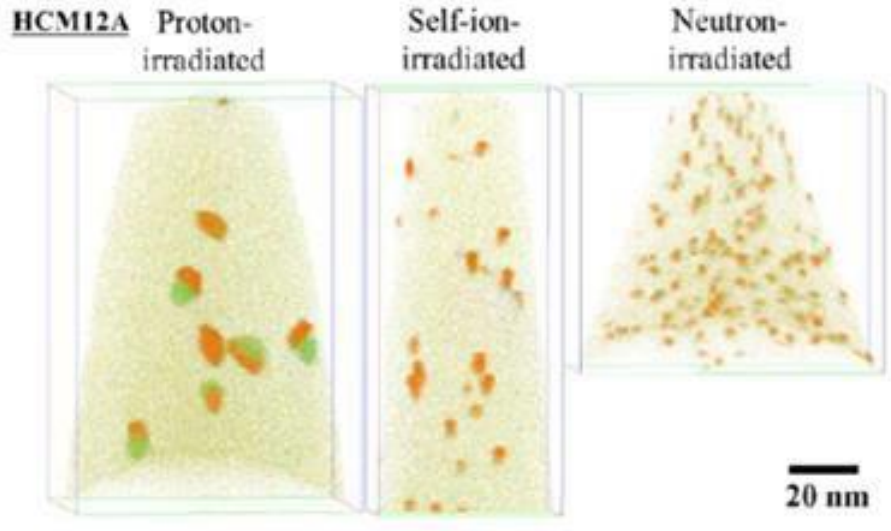

Figure 1.1. Atom probe maps of F/M alloy HCM12A irradiated to ~3 dpa at 500°C, filtered to show elements Si, Mn, Ni, P, and Cu [28]

The objective of this dissertation is to characterize, and model irradiation induced solute clustering in commercially ferritic-martensitic alloys and Zr-1 % Nb alloy following

ions or neutron irradiation as well as the temperature shift requirement for ion irradiation to emulation neutron irradiation. The second chapter of this work covers characterization of Nb-rich nanoclusters in a Zr-1%Nb alloy irradiated with either 1 MeV Kr^{2+} or fast neutrons at similar dose and temperature. Chapter 3 presents detailed study of the effect of dose rate on microstructural evolution in ferritic-martensitic alloy T91 after neutrons or Fe^{2+} irradiation to a common dose 3 dpa at 500 °C. Evaluation of temperature shift requirement prescribed by the cluster dynamic and NHM model for Fe^{2+} to emulate neutron irradiation in T91, HCM12A, and HT9 are presented in Chapter 4. Conclusions and future work are provided in Chapter 5.

Literature Cited

[1] T. Allen, K. Djamel, J.P. Wharry, Z. Jiao, Characterization of microstructure and property evolution in advanced cladding and duct: Materials exposed to high dose and elevated temperature, J. Mater. Res. (2015). doi:10.1557/jmr.2015.99.

[2] D.S. Gelles, Microstructural examination of commercial ferritic alloys at 200 dpa, J. Nucl. Mater. 237 (1996) 293–298. doi:10.1016/S0022-3115(96)00222-X.

[3] P. Dubuisson, D. Gilbon, J.L. Seran, Microstructural evolution of ferritic-martensitic steels irradiated in the fast breeder reactor Phénix, J. Nucl. Mater. 205 (1993) 178–189. doi:10.1016/0022-3115(93)90080-I.

[4] O. Anderoglu, J. Van Den Bosch, P. Hosemann, E. Stergar, B.H. Sencer, D. Bhattacharyya, Phase stability of an HT-9 duct irradiated in FFTF, J. Nucl. Mater. 430 (2012) 194–204. doi:10.1016/j.jnucmat.2012.06.038.

[5] J. Van Den Bosch, O. Anderoglu, R. Dickerson, M. Hartl, P. Dickerson, J.A. Aguiar, P. Hosemann, M.B. Toloczko, S.A. Maloy, SANS and TEM of ferritic – martensitic steel T91 irradiated in FFTF up to 184 dpa at 413 °C, J. Nucl. Mater. 440 (2013) 91–97. doi:10.1016/j.jnucmat.2013.04.025.

[6] R.L. Klueh, D.R. Harries, High-Chromium Ferritic and Martensitic Steels for Nuclear Applications, ASTM, 2001.

[7] X. Jia, Y. Dai, Microstructure in martensitic steels T91 and F82H after irradiation in SINQ Target-3, J. Nucl. Mater. 318 (2003) 207–214. doi:10.1016/S0022-3115(03)00101-6.

[8] G. Gupta, Z. Jiao, A.N. Ham, J.T. Busby, G.S. Was, Microstructural evolution of proton irradiated T91, J. Nucl. Mater. 351 (2006) 162–173. doi:10.1016/j.jnucmat.2006.02.028.

[9] E.R. Reese, M. Bachhav, P. Wells, T. Yamamoto, G.R. Odette, E.A. Marquis, On α′ precipitate composition in thermally annealed and neutron-irradiated Fe- 9-18Cr alloys, J. Nucl. Mater. 500 (2018) 192–198. doi:10.1016/j.jnucmat.2017.12.036.

[10] P. Ampornrat, G.S. Was, Oxidation of ferritic-martensitic alloys T91, HCM12A and HT-9 in supercritical water, J. Nucl. Mater. 371 (2007) 1–17. doi:10.1016/j.jnucmat.2007.05.023.

[11] P.J. Maziasz, Formation and stability of radiation-induced phases in neutron-irradiated austenitic and ferritic steels, J. Nucl. Mater. 169 (1989) 95–115. doi:10.1016/0022-3115(89)90525-4.

[12] J.J. Kai, R.L. Klue, Microstructural analysis of neutron-irradiated martensitic steels, J. Nucl. Mater. 230 (1996) 116–123. doi:10.1016/0022-3115(96)00165-1.

[13] B.H. Sencer, J.R. Kennedy, J.I. Cole, S.A. Maloy, F.A. Garner, Microstructural stability of an HT-9 fuel assembly duct irradiated in FFTF, J. Nucl. Mater. 414 (2011) 237–242. doi:10.1016/j.jnucmat.2011.03.050.

[14] Z. Jiao, V. Shankar, G.S. Was, Phase stability in proton and heavy ion irradiated ferritic-martensitic alloys, J. Nucl. Mater. 419 (2011) 52–62. doi:10.1016/j.jnucmat.2011.08.020.

[15] J.P. Wharry, Z. Jiao, V. Shankar, J.T. Busby, G.S. Was, Radiation-induced segregation and phase stability in ferritic-martensitic alloy T 91, J. Nucl. Mater. 417 (2011) 140–144. doi:10.1016/j.jnucmat.2010.12.052.

[16] J.W.P. Schmelzer, A.S. Abyzov, J. Moller, Nucleation versus spinodal decomposition in phase formation processes in multicomponent solutions, J. Chem. Phys. 6900 (2004). doi:10.1063/1.1786914.

[17] G.R. Odette, G.E. Lucas, Embrittlement of Nuclear Reactor Pressure Vessels, J. Miner. Met. Mater. Soc. (2001) 18–22. doi:10.1007/s11837-001-0081-0.

[18] K. Fukuya, Current understanding of radiation-induced degradation in light water reactor structural materials, J. Nucl. Sci. Technol. 3131 (2013). doi:10.1080/00223131.2013.772448.

[19] J.E. Zelenty, Understanding thermally induced embrittlement in low copper RPV steels utilising atom probe tomography, Mater. Sci. Technol. (2016). doi:10.1179/1743284714Y.0000000718.

[20] M. Topping, A. Harte, T.Ungar, C. P.Race, S. Dumbill, P. Frankel, M. Preuss, The effect of irradiation temperature on damage structures in proton-irradiated zirconium alloys., J. Nucl. Mater. 514 (2019) 358–367. doi:10.1016/j.jnucmat.2018.12.006.

[21] M.J. Swenson, J.P. Wharry, The comparison of microstructure and nanocluster evolution in proton and neutron irradiated Fe-9%Cr ODS steel to 3 dpa at 500 °C, J. Nucl. Mater. 467 (2015) 97–112. doi:10.1016/j.jnucmat.2015.09.022.

[22] C. Pareige, V. Kuksenko, P. Pareige, Behaviour of P, Si, Ni impurities and Cr in self ion irradiated Fe-Cr alloys - Comparison to neutron irradiation, J. Nucl. Mater. 456 (2015) 471–476. doi:10.1016/j.jnucmat.2014.10.024.

[23] A.M. Monterrosa, Z. Jiao, G.S. Was, The influence of helium on cavity evolution in ion-irradiated T91, J. Nucl. Mater. 509 (2018) 707–721. doi:10.1016/j.jnucmat.2018.06.033.

[24] Z. Jiao, J. Michalicka, G.S. Was, Self-ion emulation of high dose neutron irradiated microstructure in stainless steels, J. Nucl. Mater. 501 (2018) 312–318. doi:10.1016/j.jnucmat.2018.01.054.

[25] R. Rayaprolu, S. Möller, C. Linsmeier, S. Spellerberg, Simulation of neutron irradiation damage in tungsten using higher energy protons, Nucl. Mater. Energy. 9 (2016) 29–35. doi:10.1016/j.nme.2016.09.008.

[26] G.S. Was, J.T. Busby, T. Allen, E.A. Kenik, A. Jenssen, S.M. Bruemmer, J. Gan, A.D. Edwards, P.M. Scott, P.L. Andresen, Emulation of neutron irradiation effects with protons : validation of principle, J. Nucl. Mater. 300 (2002) 198–216. doi:10.1016/S0022-3115(01)00751-6.

[27] Z. Jiao, G.S. Was, Precipitate evolution in ion-irradiated HCM12A, J. Nucl. Mater. (2012) 105–111. doi:10.1016/j.jnucmat.2011.12.017.

[28] M.J. Swenson, J.P. Wharry, Nanocluster irradiation evolution in Fe-9%Cr ODS and ferritic-martensitic alloys, J. Nucl. Mater. 496 (2017) 24–40. doi:10.1016/j.jnucmat.2017.08.045.

[29] L.K. Mansur, Theory of transitions in dose dependence of radiation effects in structural alloys, J. Nucl. Mater. 206 (1993) 306–323. doi:10.1016/0022-3115(93)90130-Q.

Chapter 2: Evaluation of Nb-rich clustering in a Zr-1.0% Nb alloy following ion or neutron irradiation at 310 °C using atom probe tomography.

Abstract

The addition of Nb solutes to Zr-based alloys are hypothesized to improve corrosion resistance and inhibit irradiation growth. In this study, a Zr-1.0%Nb alloy is irradiated with either Kr^{2+} ions or neutrons, each to 5 dpa at 310 °C. Radiation-induced Nb-rich nanoclusters are present following each irradiation, while matrix reduction of Nb solute suggests that Nb migrates from the matrix upon irradiation to coalesces as nanoclusters. Kr^{2+} irradiation induces nanoclusters that are similar in size, density, and composition to those observed following neutron irradiation, suggesting that Kr^{2+} irradiation is a reasonable emulation of neutron irradiation.

Introduction

Zirconium-based alloys are commonly used as cladding materials in current light water reactors (LWRs), pressurized water reactors (PWRs), and boiling water reactors (BWRs) due to their low thermal neutron absorption cross section, good corrosion resistance at high temperature, and high resistance to irradiation induced swelling and creep [1,2]. More recent development of Zr-based alloys containing additions of niobium have shown that Nb can inhibit irradiation-induced growth [3,4] and improve corrosion resistance, and Zr-Nb alloys exhibit excellent mechanical properties because of the fine microstructure from different thermal annealing treatments [5,6].

Irradiation growth (sometimes referred to as “linear growth”) is an irradiation-induced phenomena in which a crystal of h.c.p. zirconium elongates along the <a> axis and shrinks along the <c> axis without any significant change in volume [7]. Irradiation growth is of great concern because it influences the structural integrity of Zr-based components [8–10]. Recent studies have shown that formation of <c> loops is directly associated with the mechanism of irradiation growth [3,7,11] and that Nb-rich nanoclusters have the potential to impede <c> loop formation. Francis et al. found that irradiation-induced Nb-rich clusters appears to inhibit <a> loop growth, which in turn limits the formation of <c> loops. These observations were made following neutron irradiation of a Low-Sn Zirlo^{TM} (which contains Nb solutes) to a dose of 18 dpa at 350°C [7], and comparing to prior results from proton irradiation of a Zr alloy without Nb solutes. M. Topping, et al. also conducted proton irradiation on two alloys with varying amounts of Nb to ~2 dpa at three different irradiation temperatures (280, 350, and 450 °C). The alloy without Nb (Zircaloy-2) exhibited a substantial increase in <c> loop sizes with increasing temperature, while the alloy with Nb solutes (Low-Sn Zirlo^{TM}) demonstrated very little change in <c> loop sizes across the same temperature range. These results suggest that Nb-rich nanoclusters may act as a barrier to loops coalescing and coarsening.

Meanwhile, the addition of Nb is also shown to improve the corrosion resistance of Zr-based alloys due to the formation of passive oxide on the surface [12–15], but ideally when Nb concentration in the matrix is low [4,16] or at the equilibrium concentration of the matrix [4]. Prior to irradiation, any Nb content above the solubility limit (~0.3-0.4 at% [17]) will typically precipitate in the form of Laves phases or β-Nb phases [18]. Upon irradiation, several studies have shown Nb to be redistributed from these phases through either ballistic

mixing or radiation-enhanced diffusion back into the matrix, creating a supersaturated composition [12,19,20]. In this condition, the over-dissolved Nb solutes are observed to reprecipitate in the form of small Nb-rich nanoclusters, which are often found to be needle-shaped [3,7,16,21,22] and can be as long as 20 – 100 nm [4]. Through the re-precipitation of the Nb solutes, the matrix composition is reduced to a level at or around the solubility limit or even lower, which is ideal for resisting corrosion. In at least one study, the matrix composition of Nb is shown to decrease with increasing irradiation dose [4]. As a result, the irradiation-induced development of Nb-rich nanoclusters can potentially produce a two-fold benefit: 1) inhibiting <c> loop formation and irradiation growth, and 2) improving corrosion resistance through optimizing the amount of Nb in solid solution. However, it is also likely that Nb-rich clusters can act as barriers to dislocation motion [3,22] leading to irradiation-induced embrittlement. Therefore, it is important to have a clear understanding of the mechanisms governing Nb-rich nanocluster evolution in Zr-based alloys and how they will evolve with long-term irradiation.

Charged particle irradiations, including heavy ions, are widely used to emulate neutron effects in candidate materials. Ions deliver high damage rates in short experimental time frames, at lower costs, and with little or no residual radioactivity. However, the dose rate and damage cascade morphologies differ widely between ions and neutrons. Currently, there is limited understanding of the significance of these physical differences and how they influence the resultant microstructure and mechanical properties of target alloys [23–26]. A few prior studies have compared ion and neutron irradiation effects on Nb-rich cluster evolution in Zr-based alloys. Z. Yu, et al. conducted proton irradiation on several Zr-xNb model alloys up to 1 dpa at 350 °C [16], and compared the results with those in ref. [12]

following neutron irradiation to 4 dpa at similar temperatures. This study found that neutron irradiation induces smaller and denser Nb-rich clusters than the proton irradiation experiments, and this difference is hypothesized to be due to differences in solute recoil distances (i.e. cascade morphology). The authors in [16] suggest that proton irradiation can be a good emulation of neutron irradiation if the irradiation parameters are optimized. Z. Lu, et al. later acknowledged this comparison is done with the proton irradiation conducted at a slightly higher temperature (i.e. a positive temperature shift), but the required temperature shift is not well understood for Zr-Nb alloys [4]. In another study, M. Topping, et al. conducted proton irradiation in Low-Sn Zirlo^{TM} to 2 dpa at irradiation temperatures of 280 °C and 450 °C [3]. They find that Nb-rich clusters following 450 °C irradiation are coarser than following 280 °C irradiation. They also acknowledge that temperature shift theory [27,28] suggests proton irradiation should be conducted with a temperature shift ~40 °C higher to emulate in-reactor irradiation effects on microstructure. However, they also suggest that alternate shifts may exist for different microstructural features, or may even be dependent on the specific alloy studied. Regardless, a lot more investigation is needed to fully elucidate how charged particle irradiations should be parameterized to accurately emulate neutron irradiation effects on Nb-rich nanocluster evolution.

The objective of this study is to characterize Nb solute migration and Nb-rich clustering in a Zr-1.0%Nb alloy irradiated with either 1 MeV Kr^{2+} ions or fast neutrons at similar dose and temperature (5 dpa at 310 °C). Atom probe tomography is used to quantify any solute cluster morphology or segregation observations prior to and following each irradiation, as well as to identify solute concentration changes which can help elucidate solute migration behavior. Comparison of the results between each irradiation and their

effects on solute redistribution enables a partial evaluation of the effects of irradiating particle and irradiation dose rate on a Zr-1.0%Nb alloy.

Methods and Materials

Material and Irradiations

The material investigated in this study is recrystallised Zr-1.0%Nb supplied by Westinghouse Electric Corporation, with composition measured by inductively coupled plasma atomic emission spectroscopy (ICP-AES) and provided in Table 2.1. Specimens were acquired from the same heat of recrystallised Zr-1.0%Nb which were oxidized in an autoclave at 360 °C, followed by irradiation with either fast neutrons or 1 MeV Kr^{2+} ions, each to 5 dpa at 310 °C. The same specimens were previously characterized via transmission electron microscopy (TEM) in [29], investigating microstructure changes in both the metal matrix and the oxide corrosion layer.

Table 2.1. Chemical composition of RXA Zr-1.0%Nb alloy in this study.

-	Zr	C	Nb	Fe	Sn	Cr	O
wt%	Bal.	0.1	0.91	0.08	0.01	< 0.01	~1.00
at%	Bal.	0.72	0.89	0.12	0.01	<0.02	~5.44

Irradiation with 1 MeV Kr^{2+} ions at 310 °C was conducted on an ~3 mm TEM disc in the Intermediate Voltage Electron Microscope (IVEM) -Tandem user facility in Argonne National Laboratory using a defocused beam. Displacement damage is calculated using the Stopping and Range of Ions in Matter (SRIM) software [30] in the “Quick Calculation”

(Kinchin-Pease) mode (Fig. 2.1) using a displacement energy of 40 eV for Zr [7]. The dose rate for 1 MeV Kr^{2+} ions was 6 x 10^{11} ions/cm^2/sec (~8.3 x 10^{-4} dpa/s) [29], and the accumulated dose is ~5 dpa at the damage peak which is ~0.20 - 0.25 μm deep into the surface. Neutron irradiation was conducted on a sheet surveillance coupon exposed for one cycle (540 days) in the Vogtle reactor at ~310 °C. The fast neutron (E > 1 MeV) fluence is estimated to be 4.35 x 10^{25} n/m^2 (at 2.14 x 10^{-7} dpa/s), which is also 5 dpa.

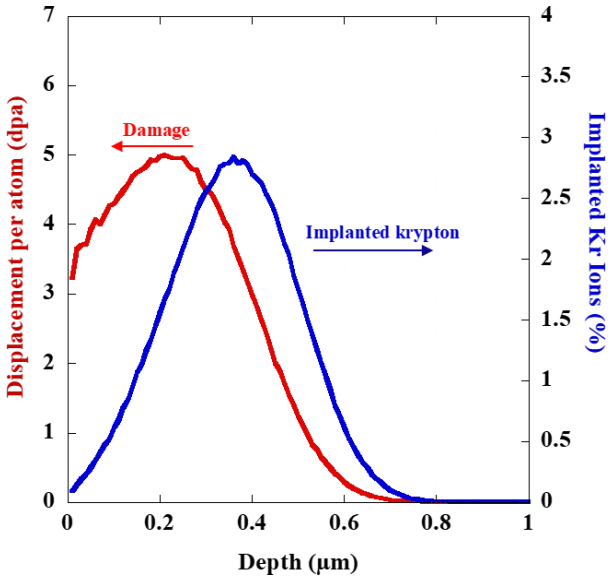

Figure 2.1. SRIM simulation of damage and ion implantation profiles for 1 MeV Kr2+ ions incident normal to Zr alloy in “Quick Calculation (K-P)” mode.

Atom Probe Tomography

Atom probe tomography is a common technique used to complement TEM, particularly for characterizing the morphology of nanoclusters within alloys as it can provide increased resolution of nanoscale phases over TEM [31]. Needle-shaped samples were prepared from the Kr^{2+} ion-irradiated, neutron-irradiated, and reference as-received

specimens using focused ion beam (FIB) milling on an FEI Quanta 3D 200i dual-beam scanning electron microscope at the Center for Advanced Energy Studies (CAES). The samples from the as-received and Kr^{2+} ion-irradiated specimen were fabricated from the bulk TEM disc using conventional techniques for sample wedge liftout, mounting, and partitioning into 6-10 separate needles. For the neutron irradiated sample, first stage FIB in situ liftout was done in the active laboratories in Studvik, Sweden by Pia Tejland. There was no prior oxide polishing before liftout, i.e. the whole oxide thickness was retained during liftout. Two TEM lamella were prepared in the size of around 10 μm × 10μm × 2μm, the activity value is very low due to the small sample volume, so that they can be easily transported in plastic sample box to Oxford for final FIB thinning and detailed analysis. However, in the case of APT samples for the neutron-irradiated specimen, the only material available to the authors was one of the residual TEM lamellae from the previous study in [29] which was mounted within a v-shaped post on a copper grid. As a result, APT sample needles were fabricated from the supporting posts on each side of the TEM lamellae, as illustrated in Fig. 2.2. For each side, the thick post was initially milled away from the thin TEM window. Next, the Omniprobe™ was welded to the end of the post, followed by cutting away the post from the grid with the ion beam. Once these steps were completed, the samples were mounted and partitioned on the local electrode atom probe (LEAP) coupon similar to conventional methods. Using this procedure, we successfully acquired multiple needles from each side of the lamellae. After mounting onto the coupons, the tips for all of the LEAP samples from each specimen were milled using annular ring patterns to a tip radius ≤50 nm, consistent with the methods described in [32].

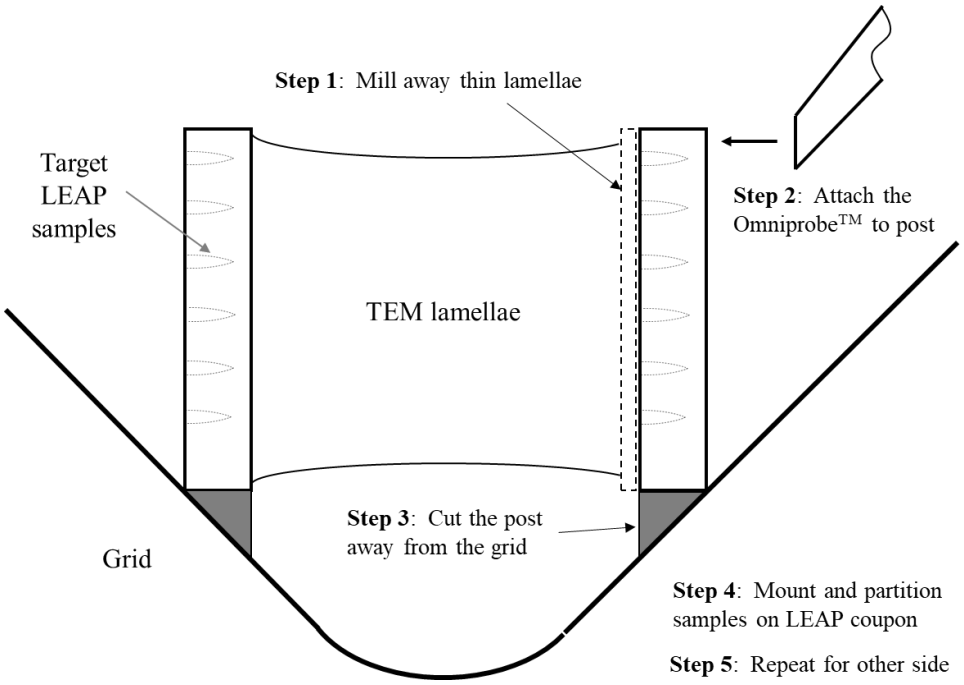

Figure 2.2. Sketch of the process to harvest LEAP needles from the support posts of a TEM lamellae mounted to a grid. This process is used for neutron-irradiated Zr-1.0%Nb samples.

Each LEAP sample was analyzed using a Cameca LEAP 4000X HR at CAES. Zirconium-based alloys are known to oxidize very quickly in atmospheric conditions, even during the short duration of transfer from the FIB to the LEAP chambers. This oxidation can embrittle the thin LEAP needles and introduce risk of fracture during evaporation. With this in mind, evaporation was conducted in laser mode at a temperature of 50 K, with a pulse repetition rate of 200 kHz, and a laser pulse energy of 50 pJ. The data from each evaporation is reconstructed and analyzed using the Integrated Visualization and Analysis Software (IVAS) Version 3.8.4. Reconstruction was done using default k-factors of 3.30 and an evaporation field of 28 V/nm, while the image compression factor (ICF) values for each reconstruction were chosen using the pole indexing module in IVAS. Unfortunately,

automatic pole indexing from the detector histogram was often unreliable at perfectly matching the visible poles. Instead, the manual band option was used for initiating the indexing by drawing bands on the visible detector histogram. With a few bands present, the software could then index the crystallographic poles more reliably. A representative example of the pole indexing is provided in Fig. 2.3. Once indexed, IVAS identifies an appropriate estimate of the ICF parameter for reconstruction. The ICF values used in this study ranged between 1.52 and 1.58 for each data set. Reconstruction of each needle is created using "Voltage" mode in IVAS, with each reconstruction visually compared to the corresponding SEM image of the sample tip to ensure the overall shape is consistent. The elements were identified via their mass-to-charge ratios and the overall isotope abundance of the species known to be present in the composition of the alloy. Isotopic peaks for Zr^{2+}/Zr^{3+} are found at 30, 30.3, 30.7, 31.3, 32, 45, 45.5, 46, 47, 48 Da, while clear evidence of ZrH^{2+} is also found in peaks 47.5 and 48.5 Da. Using the expected isotope abundance for Zr, peak deconvolution is possible for all of surrounding Zr peaks, and also for peak 46.5 Da which contains both Nb^{2+} and ZrH^{2+}. Deconvolution of the peak at 46.5 Da enables a reasonably accurate estimation of the Niobium concentration in each of the LEAP samples. Molecular ion ZrO^{2+} was also detected at 53, 53.5 and 55 Da, this is expected because of the oxidation of the needles that occurred during the transfer time from the FIB to the LEAP which is obvious at the tip of each reconstructed needles. There is peak overlap in the mass spectrum between ZrO^{2+} and Fe^{2+} at 54 Da. This was resolved by using the peak decomposition tool available on IVAS software, the allocation of peaks was decided by comparing the decomposed abundance with the expected abundance of the elemental isotopes. The peaks are assigned to the isotope whose decomposed abundance matches with the expected abundance. The

decomposed abundant of Fe^{+} is 31.83 % while the expected abundance is 5.84 %. For ZrO^{2+}, the decomposed abundance and the expected abundance are 17.10% and 17.21% respectively, which is a good match. For this reason, we assigned the peak 54 Da to ZrO^{+}.

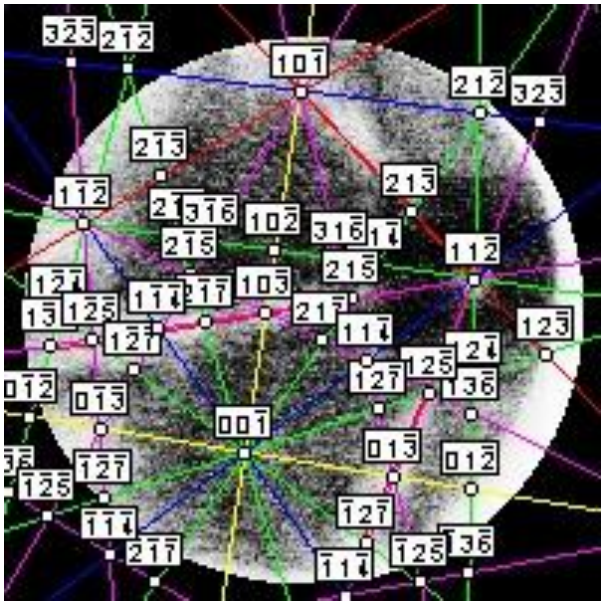

Figure 2.3. A representative example of pole indexing using IVAS version 3.8.4 for a Zr-1.0%Nb LEAP data set.

Cluster analysis is performed on each reconstruction using the maximum separation method [33]. Successful use of this technique is dependent on proper selection of the d_{max} and N_{min} parameters for cluster analysis. This technique requires iteration between the N_{min} (minimum number of solute atoms that can form a cluster) and d_{max} (the maximum separation distance between atoms in the cluster). These two parameters (d_{max} and N_{min}) must be carefully selected to minimize the chance of identifying statistically random clusters and also to reduce the chance of multiple clusters being counted as one [34]. The d_{max} and N_{min} values for this study range from 0.80 – 1.21 nm and 15 – 20 ions, respectively. Each result is

visually inspected to confirm the identified clusters are consistent with those identified with isosurfaces created with an ~3 - 4% concentration threshold, and with clusters visible in the reconstruction images. The cluster radii, number densities, and volume fraction under different irradiation conditions were determined from data in the IVAS cluster analysis output .cvs file for each sample. For each cluster, the Guinier diameter was calculated using accepted techniques in [34–36]. The nanocluster number density (N_{nc}) was determined by counting the total number of clusters identified in all tips and dividing by the total analyzed volume in all characterized tips from that specimen. The volume fraction of clusters (f_v) is found by counting the total number of atoms in the measured clusters and dividing by the total number of atoms in the combined reconstructed volumes. The IVAS output file also includes a detailed composition of each cluster and the matrix, enabling simple determination of the average cluster composition and the overall matrix composition (c_m^i) for each solute species, i.

Results and Discussion

APT Characterization

To our knowledge, APT is less commonly used on Zr-based alloys, likely due to concerns about rapid oxidation of the sample needles during the transfer time between the FIB and the LEAP equipment for analysis. This oxidation can make the samples more brittle, limiting the amount of atomic evaporation possible in the LEAP before fracture of the sample needle. In this study, several of the needles fabricated also experienced early fracture. The usable LEAP data sets ranged in size from 2.2 million to 14.9 million ion counts per needle,

providing enough data to reconstruct a few needles and conduct cluster analysis for each specimen.

Representative three-dimensional APT reconstructions for each of the Zr-1.0%Nb specimens are provided in Fig. 2.4. There is no evidence of any Nb-rich nanoclusters observed in the unirradiated specimen. However, a homogenous distribution of Nb-rich clusters is found after both Kr^{2+} and neutron irradiation to 5 dpa. Following Kr^{2+} irradiation, a total of 237 clusters are identified with an average size of 3.33 ± 0.04 nm and a number density of 2.42 x 10^{23} m^{-3}. Meanwhile, with less analysis region available following neutron irradiation, a total of 16 clusters are identified with an average size of 2.96 ± 0.30 nm and 1.13 x 10^{23} m^{-3} number density. A quantitative summary of the cluster analysis allowing for direct comparison across each irradiation is presented in Table 2.2 and Fig. 2.5. The size of the clusters in this study are slightly larger than those observed by Topping, et al., who reported Nb-rich clusters sizes of 1.9 ± 1.0 nm and 2.5 ± 0.9 nm following proton irradiation to 2 dpa at 280 °C and 450 °C, respectively [3].

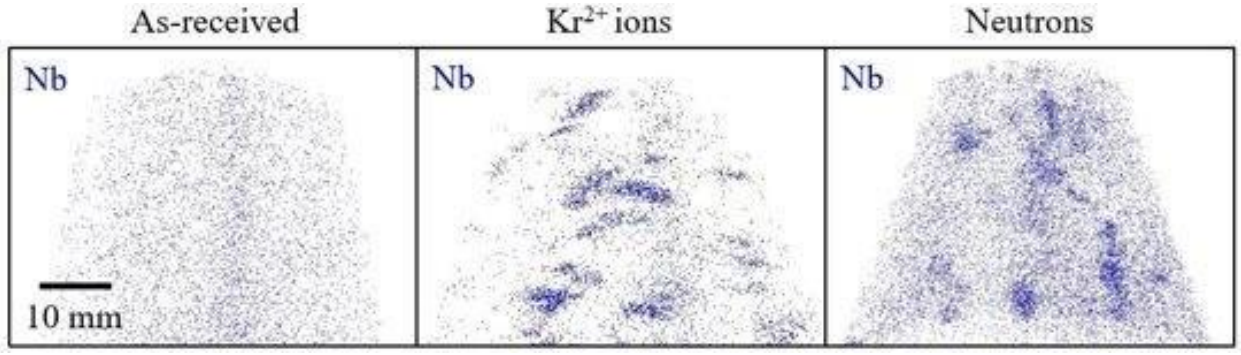

Figure 2.4. Atom probe tomography images of Nb solute distributions in the matrix of Zr-1.0%Nb alloy. Irradiation with 1 MeV Kr2+ ions or fast neutrons resulted in comparable Nb-rich cluster morphologies.

Table 2.2. Summary of APT cluster analysis for Zr-1.0%Nb.

APT Summary	**As-received**	**Kr^{2+} irradiated (5 dpa, 310 °C)**	**Neutron-irradiated (5 dpa, 310 °C)**
# of needles	6	6	2
Analysis volume, V_T (nm^3)	1,197,802	958,894	142,138
Nb-rich nanoclusters			
# of clusters measured	0	237	16
Average Guinier diameter, D_G (nm)	-	3.33	2.96
Standard deviation for D_G	-	±0.64	±1.22
Std. dev. of the mean for D_G	-	±0.04	±0.30
Number Density, N_{nc} (m^{-3})	-	2.42×10^{23}	1.13×10^{23}
Volume fraction, f_v	-	0.36%	0.20%
Average Nb Composition (at%)	-	23.2%	48.2%
Standard deviation for Nb Comp.	-	±10.8%	±19.1%
Std. dev. of the mean for Nb Comp.	-	±0.7%	±4.8%
Average cluster aspect ratio	-	1.97 ± 0.86	1.62 ± 0.49
Matrix Composition (c_m^i)			
Nb, c_m^{Nb} (at%)	0.45	0.34	0.34
Fe, c_m^{Fe} (at%)	0.15	0.14	0.11
Cr, c_m^{Cr} (at%)	0.01	0.03	0.03

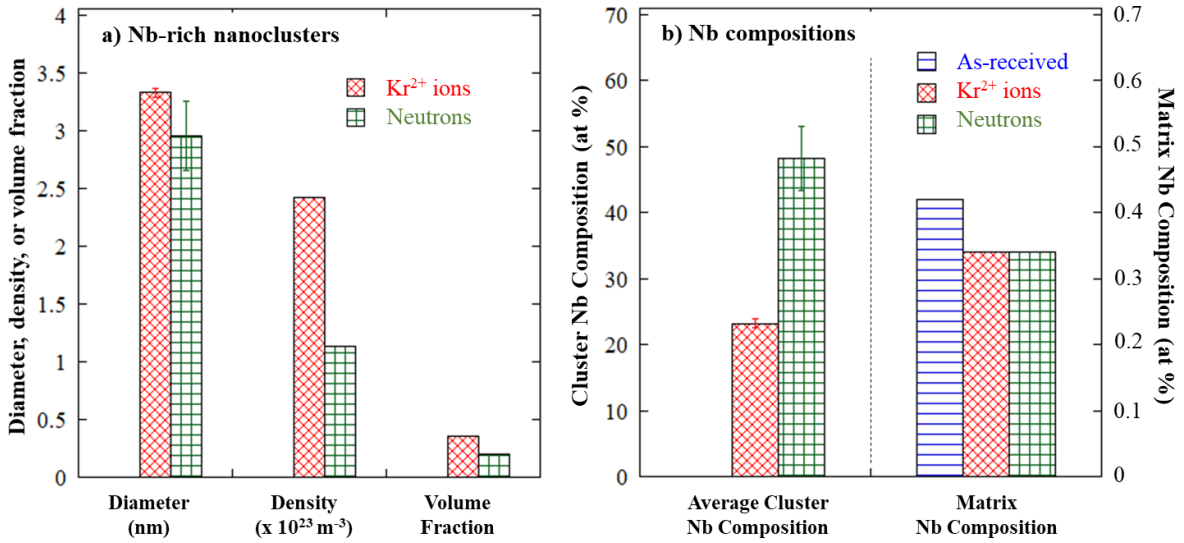

Figure 2.5. Quantitative data summarizing the comparison between the a) Nb-rich nanocluster morphology, and b) Nb composition distributions for each of the specimens studied.

The aspect ratio of the Nb-rich nanoclusters is estimated by comparing the maximum value for R_{gx}, R_{gy}, and R_{gz} (from the IVAS output file) and the minimum value of the three. Using this simplistic approach, the average aspect ratio is found to be 2.0:1 and 1.6:1 following Kr^{2+} and neutron irradiation, respectively. Given the relatively random orientations of R_{gx}, R_{gy}, and R_{gz} these ratios should be taken as a minimum, but still suggest that the nanoclusters are generally elongated in shape, consistent with the irradiation-induced needle-like Nb-rich platelets reported in previous studies [4,7,12,19,21,37].

Cluster analysis enables measurement of the composition for each of the Nb-rich nanoclusters. Following Kr^{2+} irradiation, the average Nb content in the nanoclusters is 23.2 ± 0.7 at% Nb, while the Nb content after neutron irradiation is 48.2 ± 4.8% (Table 2.2). These

values are measured without any adjustment for trajectory aberrations, which are expected to be present from the LEAP process. These values are also consistent with those found by Z. Yu, et al., who measured the Nb content of irradiation-induced Nb-rich platelets using a STEM/EDS linescan in a Zr-1.0%Nb alloy and found values ranging ~15 – 40 at% [16].

Similar to the cluster compositions, the IVAS cluster analysis also enables evaluation of the composition in the matrix of each specimen (Table 2.2). The Nb in solid solution in the as-received samples is determined to be ~0.45 at%, consistent with prior studies confirming the solubility limit of Nb in α-Zr is between 0.20 % - 0.49 % [17,38]. However, the Nb content in the matrix is shown to possibly decrease slightly to 0.34 at% following each irradiation to 5 dpa, while the volume fraction of Nb-rich clusters is found to be 0.36 % and 0.20 % at (Table 2.2) following Kr^{2+} ion or neutron irradiation, respectively. The decrease in Nb content confirm that Nb solutes are migrating from the matrix to the Nb-rich clusters upon irradiation. Several prior studies have reported that the reduction of Nb in the matrix could help increase reactor corrosion resistance as a result of irradiation damage to the metal matrix [16,39]. The apparent evidence of reduced Nb content in solid solution following irradiation appears to support the notion that irradiation could have a positive influence on the corrosion resistivity of the alloy.

In the as-received sample, there is evidence of grain boundary segregation of Fe and Cr observed in one of the reconstructions (Fig. 2.6a). Hudson and Smith [40] observed similar segregation of Fe (via APT) in an unirradiated Zr-1.0%Nb alloy and attributed it to the large radius mismatch between Fe and Zr. Francis, et al. also reported segregation of Fe to the grain boundary in unirradiated, Low-Sn Zirlo^{TM} (Zr-1.0% Nb) [41]. The additional segregation of Cr in this study may be due to both Fe and Cr having similar atomic radii. A

representative linescan across a grain boundary in the as-received specimen and the corresponding concentration profiles are shown in Fig. 2.6b and Fig. 2.6c, respectively. Enrichments are observed with ΔFe ~0.15 at% and ΔCr ~0.11 at%, while Zr is seen to deplete with ΔZr ~-7.5 at%. The specimens irradiated with either Kr^{2+} ions or neutrons to 5 dpa at 310 °C do not exhibit evidence of Fe and Cr enrichment at the grain boundary, but this may also be due to the lack of any LEAP samples intersecting a grain boundary.

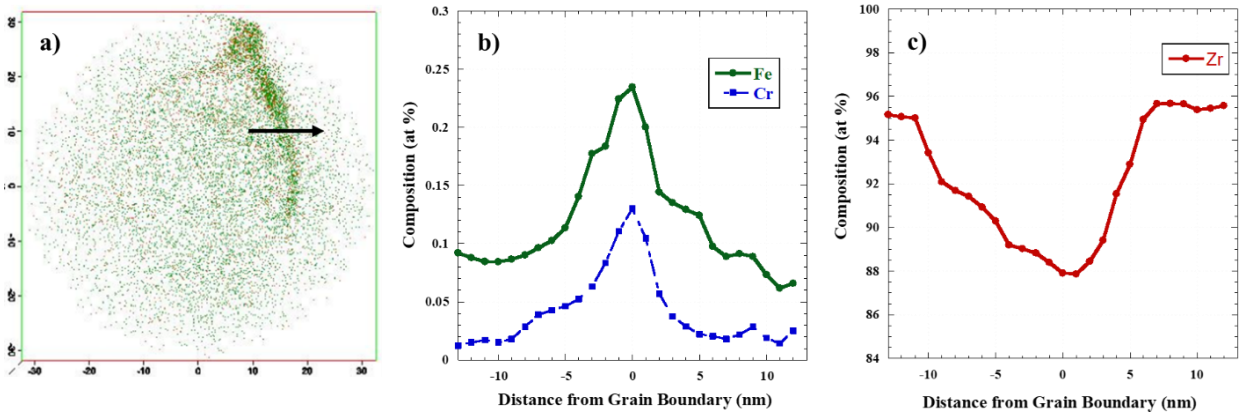

Figure 2.6. Linescan and concentration profiles for Fe, Cr, and Zr across a grain boundary in as-received Zr-1.0%Nb alloy.

Kr^{2+} ions and neutron irradiation comparison

For evaluating Kr^{2+} ion irradiation as an effective surrogate for neutron irradiation, we can compare the results for Nb-rich nanocluster evolution following each irradiation, illustrated and tabulated in Fig. 2.4 and Table 2.2, respectively. Following each irradiation, Nb-rich nanoclusters are observed with comparable size, number density, volume fraction, Nb composition, and aspect ratio. However, Kr^{2+} irradiation appears to potentially yield

slightly larger, more numerous, and more elongated clusters, but the limited analysis region for these measurements make it difficult to firmly draw this conclusion. Overall, the results suggest that Kr^{2+} irradiation is a reasonably good emulation of neutron irradiation to 5 dpa at 310 °C for Nb-rich cluster evolution, but the Kr^{2+} irradiation can potentially be parameterized to offer a closer match in nanocluster morphology.

The formation of irradiation-induced nanoclusters is hypothesized to be dependent on two primary competing mechanisms: ballistic dissolution and radiation-enhanced diffusion-driven growth. Higher dose rate (Kr^{2+} ion) irradiation is expected to induce a higher rate of radiation-enhanced diffusion, favoring coarsening of Nb-rich nanoclusters. This may explain why nanoclusters are slightly larger after Kr^{2+} irradiation. Meanwhile, in the case of Zr-based alloys, the effects of ballistic dissolution may apply to redistribution of Nb solutes attempting to cluster. At the same time, the rate of generation and coalescence of point defects may also influence the nucleation of solute clusters, similar to other alloys systems.

The invariance theory can be used to further probe the significance of dose rate in the evolution of Nb-rich nanoclusters in Zr-1.0%Nb alloys. Mansur's invariance theory suggests that a temperature shift is necessary to produce consistent microstructures when irradiating with varying dose rates [27]. These microstructures are bound by two mechanisms of point defect loss: 1) mutual recombination, and 2) diffusion to sinks. The temperature shifts for both the recombination and diffusion-limited regimes are calculated for a reference irradiation at 310 °C and 2.14×10^{-7} dpa/s (our neutron irradiation conditions) are illustrated in Fig. 2.7. The vacancy migration and formation energies used are 1.43 eV [44] and 1.92 eV [45], respectively for an h.c.p. Zr-based alloy. At the Kr^{2+} ion irradiation dose rate (8.33×10^{-4} dpa/s), the recombination-dominated regime estimates a temperature shift of $\Delta T = +39$ °C.

For comparison, similar dose rate variations in b.c.c. Fe-based alloys estimate the recombination-dominated temperature shift to be ~60 - 70 °C [46], suggesting that h.c.p. Zr-based alloys may inherently be less sensitive to dose rate and temperature changes than their b.c.c. Fe-based alloy counterparts. This may explain the results herein, which appear to indicate that Kr^{2+} irradiation to low dose is a reasonable surrogate for in-reactor neutron irradiation at the same temperature and dose.

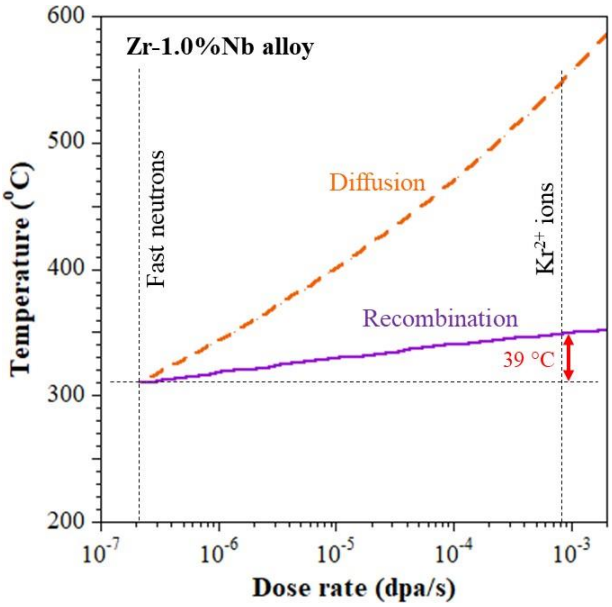

Figure 2.7. Temperature shift for irradiation induced solute clustering at different dose rates

Conclusions

In summary, A Zr-1.0%Nb alloy is irradiated with either Kr^{2+} ions or in-reactor neutrons, each to 5 dpa at 310 °C. Radiation-induced Nb-rich nanoclusters are present following each irradiation, which could serve as a barrier to irradiation growth. Evidence of solute migration suggests that Nb is redistributed from the native β-Nb precipitates to the matrix upon irradiation, then coalesce into new Nb-rich nanoclusters. Finally, in the context

of Nb-rich nanoclusters, Kr^{2+} irradiation induces nanoclusters that is similar in size, density, composition, and aspect ratio to those observed following neutron irradiation at similar dose and temperature, suggesting that Kr^{2+} irradiation is a reasonable emulation of neutron irradiation. Simple evaluation of dose rate sensitivity using the invariance theory predicts that only a small temperature shift may be needed for Kr^{2+} to accurately emulate neutron irradiation.

Literature Cited

[1] A.T. Motta, A. Couet, R.J. Comstock, Annu. Rev. Mater. Res. 45 (2015) 311–343.

[2] R.B. Adamson, C.E. Coleman, M. Griffiths, J. Nucl. Mater. 523 (2019) 540–545.

[3] M. Topping, A. Harte, T.Ungar, C. P.Race, S. Dumbill, P. Frankel, M. Preuss, J. Nucl. Mater. 514 (2019) 358–367.

[4] Z. Yu, A. Couet, M. Bachhav, J. Nucl. Mater. 516 (2019) 100–110.

[5] T.R. Allen, R.J.M. Konings, A.T. Motta, Compr. Nucl. Mater. 5 (2012) 49–68.

[6] Y. Matsukawa, S. Kitayama, K. Murakami, Y. Shinohara, K. Yoshida, H. Maeno, H.L. Yang, T. Toyama, K. Yasuda, H. Watanabe, A. Kimura, H. Muta, S. Yamanaka, Y.F. Li, Y. Satoh, S. Kano, H. Abe, Acta Mater. 127 (2017) 153–164.

[7] E. Francis, R.P. Babu, A. Harte, T.L. Martin, P. Frankel, D. Jädernäs, J. Romero, L. Hallstadius, P.A.J. Bagot, M.P. Moody, M. Preuss, Acta Mater. (2018).

[8] G.J.C. Carpenter, D.O. Northwood, J. Nucl. Mater. (1975) 260–266.

[9] R.B. Adamson, in: ASTM Int., ASTM International, West Conshohocken, PA, 2000, pp. 15–31.

[10] C.H. Woo, Radia. Eff. Defects Solids (1998) 145–169.

[11] M.Griffiths, R.W.Gilbert, J. Nucl. Mater. 150 (1987) 169–181.

[12] S. Doriot, D. Gilbon, J.L. Bechade, M.H. Mathon, L. Legras, J.P. Mardon, J. ASTM Int. (2005) 1–24.

[13] V. Shishov, A. Nikulina, V. Markelov, M. Peregud, A. Kozlov, S. Averin, S. Kolbenkov, A. Novoselov, Zircon. Nucl. Ind. Elev. Int. Symp. STP16192S. West Conshohocken, PA ASTM Int. (1996) 603–622.

[14] V.M. G. Kobylyansky, A. Novoselov, A. Obukhov, Z. Ostrovsky, V. Shishov, M. Peregud, J. ASTM Int. (2011) 1–14.

[15] Y. Etoh, S. Shimada, J. Nucl. Sci. Technol. 3131 (2012).

[16] Z. Yu, C. Zhang, P. Voyles, L. He, X. Liu, K. Nygren, A. Couet, Acta Mater. (2019).

[17] J.P. Abriata, J.C. Bolcich, Bull. Alloy Phase Diagrams 3 (1982) 34–44.

[18] M. Cottura, E. Clouet, Acta Mater. 144 (2018) 21–30.

[19] A. Harte, R.P. Babu, C.A. Hirst, T.L. Martin, P.A.J. Bagot, M.P. Moody, P. Frankel, J. Romero, L. Hallstadius, E.C. Darby, M. Preuss, J. Nucl. Mater. 510 (2018) 460–471.

[20] G. He, J. Liu, K. Li, J. Hu, A.H. Mir, S. Lozano-Perez, C. Grovenor, J. Nucl. Mater. 526 (2019) 151738.

[21] J. Ribis, S. Doriot, F. Onimus, J. Nucl. Mater. 511 (2018) 18–29.

[22] A. Harte, R.P. Babu, C.A. Hirst, T.L. Martin, P.A.J. Bagot, M.P. Moody, P. Frankel, J. Romero, L. Hallstadius, E.C. Darby, M. Preuss, J. Nucl. Mater. 510 (2018) 460–471.

[23] C. Pareige, V. Kuksenko, P. Pareige, J. Nucl. Mater. 456 (2015) 471–476.

[24] Z. Jiao, J. Michalicka, G.S. Was, J. Nucl. Mater. 501 (2018) 312–318.

[25] R. Rayaprolu, S. Möller, C. Linsmeier, S. Spellerberg, Nucl. Mater. Energy 9 (2016) 29–35.

[26] G.S. Was, J.T. Busby, T. Allen, E.A. Kenik, A. Jenssen, S.M. Bruemmer, J. Gan, A.D. Edwards, P.M. Scott, P.L. Andresen, J. Nucl. Mater. 300 (2002) 198–216.

[27] L.K. Mansur, J. Nucl. Mater. 206 (1993) 306–323.

[28] G.S. Was, Fundamentals of Radiation Materials Science, Springer, New York, 2007.

[29] J. Hu, A. Garner, P. Frankel, M. Li, M. Kirk, S. Lozano-Perez, M. Preuss, C. Grovenor, Acta Mater. 173 (2019) 313–326.

[30] R.E. Stoller, M.B. Toloczko, G.S. Was, A.G. Certain, S. Dwaraknath, F.A. Garner, Nucl. Instruments Methods Phys. Res. Sect. B Beam Interact. with Mater. Atoms 310 (2013) 75–80.

[31] S. Lozano-perez, Mater. Oper. Asp. Plant Life Manag. (2010) 389–416.

[32] K. Thompson, D. Lawrence, D.J. Larson, J.D. Olson, T.F. Kelly, B. Gorman, Ultramicroscopy 107 (2007) 131–139.

[33] J.M. Hyde, E.A. Marquis, K.B. Wilford, T.J. Williams, Ultramicroscopy 111 (2011) 440–447.

[34] M.J. Swenson, J.P. Wharry, J. Nucl. Mater. 496 (2017) 24–40.

[35] M.K. Miller, R. Forbes, Atom Probe Tomography: The Local Electrode Atom Probe, Springer, New York, 2014.

[36] C.A. Williams, E.A. Marquis, G.D.W.S. A. Cerezo, J. Nucl. Mater. (2010) 37–45.

[37] S. Saini, N. Gayathri, S.K. Sharma, A. Devi, A.P. Srivastava, S. Neogy, P. Mukherjee, P.K. Pujari, J. Nucl. Mater. 528 (2020) 151894.

[38] O.T.Woo, M. Griffiths, J. Nucl. Mater. 384 (2009) 77–80.

[39] J. Hu, A. Garner, P. Frankel, M. Li, M.A. Kirk, S. Lozano-Perez, M. Preuss, C. Grovenor, Acta Mater. 173 (2019) 313–326.

[40] D. Hudson, G.D.W. Smith, Scr. Mater. 61 (2009) 411–414.

[41] E.M. Francis, A. Harte, P. Frankel, S.J. Haigh, D. Jädernäs, J. Romero, L. Hallstadius, M. Preuss, J. Nucl. Mater. 454 (2014) 387–397.

[42] C. Coleman, G.W. R. Gilbert, in: Pittsburgh, Pittsburgh, 1980, pp. 587–599.

[43] P. LEI, R. Guang, L. Chenwei, Y. Chao, L. Dong, L. Jianxin, W. Yizhen, J. Xu, Materials (Basel). (2017) 1–11.

[44] A. Couet, L. Borrel, J. Liu, J. Hu, C. Grovenor, Corros. Sci. 159 (2019).

[45] X. Zhu, X. Gao, H. Song, G. Han, D. Lin, Mater. Des. 119 (2017) 30–37.

[46] S. Taller, Z. Jiao, K. Field, G.S. Was, J. Nucl. Mater. (2019) 151831.

Chapter 3: Comparison of microstructure evolution in Fe^{2+} or neutron irradiated T91 at 500 °C

Abstract

The objective of this study is to evaluate dose rate effects on microstructure evolution in ferritic-martensitic alloy T91 following neutron or Fe^{2+} irradiation to a common dose (3 dpa) and temperature (500 °C). Characterization via TEM and APT is also conducted following Fe^{2+} irradiation to 100 dpa at 500 °C. Dislocation loop morphologies are consistent following each irradiation to 3 dpa, with only minor growth observed at 100 dpa. Each irradiation exhibits favorability for a<100> loops over a/2<111>. Si-Mn-Ni-rich and Cu-rich nanoclusters are more coarsely distributed following Fe^{2+} irradiation, while the same solutes exhibit strong evidence of segregation to grain boundaries, dislocation loops, and dislocation lines following both irradiations to 3 dpa. However, after 100 dpa, solutes are likely redistributed. While the invariance theory likely explains dislocation loop evolution with variations in dose rate, it is not sufficient to predict temperature shift requirements for solute cluster evolution at 3 dpa.

Introduction

The extreme conditions in advanced fission reactors will require the development of structural materials that exhibit phase and microstructural stability at high temperature (up to 700 °C) and high doses (several hundred dpa) [1–3]. Ferritic-martensitic (F/M) alloys, including the commercially available T91, are leading candidates for advanced nuclear reactors due to their low ductile-to-brittle transition temperature (DBTT) shift, high temperature creep resistance, thermal shock resistance, and low swelling [4–16]. However,

irradiation can cause microstructural changes and the evolution of precipitates which can lead to significant hardening or embrittlement [17–22], potentially rendering the alloys unsuitable for advanced reactor applications.

In order to expedite the understanding of the irradiation effects on alloys, charged particle irradiations are frequently used to emulate neutron irradiation in candidate materials [4,23–28]. Rapid damage rates enable shorter experimental timeframes, lower costs, and lack of residual radioactivity, all major factors favoring charged particle experiments to simulate irradiation damage. However, the dose rate and damage cascade morphologies differ widely between ions and neutrons, and there is a limited understanding of the significance of these physical differences and how they affect resultant microstructures with defect cluster and solute cluster morphologies.

Experimental evidence for the role of dose rate and damage cascades, including in b.c.c. Fe-based alloy microstructure evolution is limited due to the challenge of comparing neutron to charged particle irradiations on identical heats of archival alloys. In particular, it is important to match up prior irradiations experiments with the same alloy heats to ensure a controlled comparison of the results. This can be challenging if the availability of specific alloy heat materials are limited or exhausted through prior experimentation. However, a few recent studies of irradiation response in F/M alloys have provided significant insight into these relationships. One earlier study conducted by Was et al. [29] evaluated the F/M alloy HT9 following self-ion and neutron irradiations. Self-ion irradiation conditions were selected following the invariance theory [30,31] with 5 MeV Fe^{2+} ion irradiation at 460 °C to 188 dpa to emulate neutron irradiation at 443 °C to 155 dpa. This experiment successfully resulted in consistent void morphologies, but the Si-Mn-Ni-rich clustering (e.g. G-phase) and

dislocation loop morphologies were less consistent, suggesting the potential for additional mechanisms governing the evolution of these features. Another pair of studies conducted by Swenson and Wharry [6,23] compared different particle irradiations on identical heats of F/M alloys HCM12A and HT9. Each alloy was irradiated with fast neutrons (~10^{-7} dpa/s), protons (~10^{-5} dpa/s) or Fe^{2+} self-ions (~2 x 10^{-4} dpa/s). The evolution of dislocation loops and voids after ~3 dpa are statistically invariant between each irradiation, supporting the invariance theory for a recombination-dominant regime where only a relatively small temperature shift is required for higher dose rate irradiation to emulate lower dose rate neutron irradiation. However, contrary to their findings for *defect* clusters, a fixed dose with little to no temperature shift does not yield consistent nanocluster morphologies across all dose rates; the temperature dependencies appear to be inconsistent with the invariance theory for *solute* clusters.

A more recent study conducted by Taller et al. [32] evaluates the ability of dual ion irradiation (Fe^{2+} and He^{2+}) to successfully emulate microstructure evolution following neutron irradiation in the F/M alloy T91. Dual ion irradiation conditions (at 7 x 10^{-4} dpa/s) are selected across a range of positive temperature shifts following the invariance theory to identify the conditions which most closely emulate the results from a prior study of BOR-60 neutron irradiated (at 6-9 x 10^{-7} dpa/s) T91 conducted by Jiao, et al. [33]. They find very good agreement in the dislocation loop morphologies and cavity size distribution when using a temperature shift of ~+60-70 °C, closely matching the +50-60 °C shift prescribed by the Mansur invariance theory. However, a match in morphology is not achieved for solute RIS behavior and Ni-Si-rich cluster evolution, suggesting the possibility for different mechanisms

governing solute migration and clustering evolution and the need for an alternate temperature shift to account for these relationships.

Several additional studies have focused on irradiation-induced microstructure evolution in T91 following various isolated irradiation conditions. To our knowledge, the most comprehensive studies of dose dependence for cavity evolution were conducted by Getto, et al. [34] and more recently by Monterrosa, et al. [24]. Both of these studies conduct self-ion irradiations at 460 ℃ to high dose (>300 dpa), but the Monterrosa, et al. study also systematically evaluates the effects of He implantation on cavity evolution. Without He implantation, small voids appear at 130 dpa and display exponential growth with increasing dose [34]. However, with varying levels of pre-implanted He, cavities are observed as early as 45 dpa and the density of cavities appears to be enhanced with increasing He implantation [24]. Dislocation loop evolution in T91 is also reported in recent literature; a visual summary of the average loop size is provided in Fig. 3.1a. Generally, dislocation loops are <30 nm in average diameter regardless of irradiation temperature or dose, suggesting the dislocation loop microstructures saturate at a relatively low dose and remain reasonably stable up to higher doses.

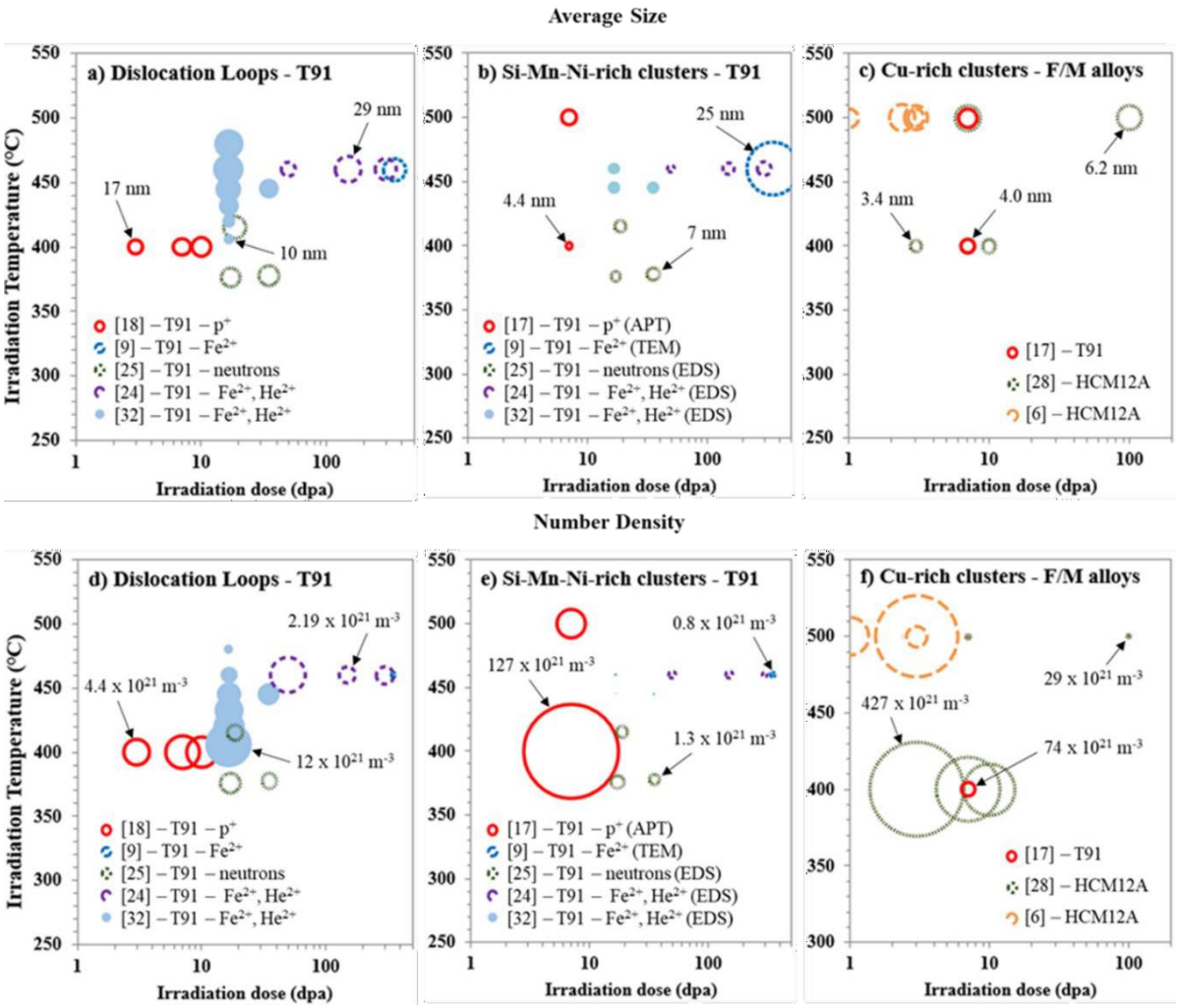

Figure 3.1. Archival literature results for F/M alloys illustrating relative size and number density for a) and d) dislocation loops in irradiated T91, b) and e) Si-Mn-Ni-rich nanoclusters in irradiated T91, and c) and f) Cu-rich nanoclusters in irradiated F/M alloys HCM12A and T91 (measured via APT). For b) and e), the method of characterization of the nanoclusters is provided in parenthesis. Size of bubbles represent relative size of features, with a few measurements indicated in each chart for reference.

A number of archival studies also evaluate irradiation-induced solute cluster evolution in T91; average nanoclusters sizes for Si-Mn-Ni-rich and Cu-rich clusters are

provided in Fig. 3.1b and Fig. 3.1c, respectively. Jiao, et al. [17] conducted proton irradiation on T91 to a dose of 7 dpa at both 400 °C and 500 °C, with Si-Mn-Ni-rich cluster size increasing from 4.4 nm to 8.0 nm as temperature increases, while the number density conversely decreases from 127 x 10^{21} m^{-3} to 14 x 10^{21} m^{-3} (characterized using atom probe tomography). Getto et al. also observed Si-Mn-Ni-rich clusters using transmission electron microscopy (TEM) following Fe^{2+} ion irradiation of commercial T91 to doses ranging 75 to 650 dpa at 460 °C, but they only measured the size of the clusters at 350 dpa. The measured cluster size and number density for T91 were 24.8 nm and 0.8 x 10^{21} m^{-3}, respectively [34]. The larger size and lower density may also be related to the limitation of TEM in detecting smaller clusters. In addition to the Jiao, et al. [33] and Taller, et al. [32] studies discussed earlier, the recent study by Monterossa, et al. [24] quantifies Si-Mn-Ni-rich cluster evolution upon Fe^{2+} irradiation at 460 °C. Clusters are found to increase in average diameter from 4.5 nm at 50 dpa to 7.0 nm at 150 dpa and to 7.6 nm at 300 dpa (all with 10 appm of pre-implanted He). For these same doses, cluster number density declines from 14.9 x 10^{20} m^{-3} to 13.3 x 10^{20} m^{-3} and 7.57 x 10^{20} m^{-3}, respectively. These results are consistent with general trends in T91 and other F/M alloys [6,34–38], with clusters generally exhibiting coarsening with higher temperatures or higher doses. In a few instances in literature, Cu-rich nanoclusters are also observed in F/M alloys. Cu-rich clusters are known to form prior to the Si-Mn-Ni-rich clusters and can create nucleation sites for both Cu-core/Si-Mn-Ni-shell structures [39] or Cu-cores with Si-Mn-Ni appendages [6]. To our knowledge, only one prior study of T91 has positively identified Cu-rich clustering. A summary of the average sizes of Cu-rich nanoclusters reported in F/M alloys from literature is provided in Fig. 3.1c, also demonstrating an overall trend of larger clusters at higher temperatures or higher doses. Their

formation is typically attributed to the low solubility limit of Cu in Fe, while there is evidence that Cu clusters likely nucleate before the Si-Mn-Ni-rich clusters and potentially provide a site for heterogeneous nucleation of Si-Mn-Ni-rich clustering. Swenson and Wharry observed the nucleation of Cu clusters in HCM12A before 1 dpa, followed by Si-Mn-Ni clusters at or near the Cu-cluster matrix interface between 1 and 2.4 dpa under proton irradiation [6]. Jiao et al. [28] also studied Cu-rich clustering in HCM12A following proton irradiation at 400 °C and 500 °C. The Cu clusters were observed to slightly coarsen at 400 °C as dose increased from 3 dpa (3.4 nm diameter) to 7 dpa (4 nm diameter) and to 10 dpa (3.8 nm diameter) while number density decreases from 4.27 x 10^{23} m^{-3} (3 dpa) to 2.96 x 10^{23} m^{-3} (7 dpa) and to 2.39 x 10^{23} m^{-3} at 10 dpa. In this same study, Cu clusters in HCM12A following proton irradiation at both 400 °C and 500 °C to 7 dpa were found to be more coarse at higher temperature. Average diameter increases from 4 nm to 6.6 nm and number density decreases from 2.96 x 10^{23} m^{-3} to 0.37 x 10^{23} m^{-3} at 400 °C and 500 °C, respectively. Similarly, in another study, Jiao, et al. [17] studied Cu clustering in T91 following proton irradiation to 7 dpa at both 400 °C and 500 °C. In this study, Cu clusters were also observed to coarsen at higher temperature, as size increases from 4 nm to 5 nm following irradiation at 400 °C and 500 °C, respectively, while number density declines from 0.74 x 10^{23} m^{-3} to 0.17 x 10^{23} m^{-3} at the same temperatures.

The archival literature offers good insight into the effects of dose and temperature on *defect* cluster evolution, with multiple studies appearing to corroborate the invariance theory for establishing irradiation conditions for ion irradiations to emulate neutron irradiations. However, the evolution of *solute* clusters (particularly Si-Mn-Ni-rich clustering) appears to be governed by different or additional mechanisms, suggesting the invariance theory may not

be able to solely explain their irradiation evolution behavior at higher dose rates. A few studies have attempted to model Si-Mn-Ni-rich cluster evolution in Fe-Cr alloys. Odette et al, carried out CALPHAD based thermodynamic calculations to describe the evolution of fine-scale microstructure features that cause irradiation embrittlement in RPV steels [40]. Based on the estimation of the pair-bond energy from CALPHAD, Lattice Monte Carlo was later used to predict the Cu-rich and Si-Mn-Ni rich precipitate structure [41]. The result suggested that high Ni concentration, low irradiation temperature, and small amounts of Cu enhances the formation of Si-Mn-Ni clusters. More recently, cluster dynamic modeling has been used to predict the nucleation and growth of Si-Mn-Ni phases in low-Cu RPV steels and F/M alloy T91 [42,43], comparing the simulation results with existing experimental data.

The evolution of Si-Mn-Ni solute clusters is potentially made kinetically possible by the high flux of point defects and the formation of point defect clusters under irradiation [44–46], and these clusters could be more stable at higher temperatures due to the synergy between Mn and Ni and the presence of Cu [46]. However, the thermodynamic stability of these solute nanoclusters is still under debate. Meslin, et al. [47] reported a high number density of Mn-Ni solute clusters following neutron irradiation of Fe-1.2Mn-0.7Mn alloy to 0.2 dpa. After annealing at 400 °C, partial dissolution of solute clusters was observed, suggesting that the driving force for the formation of solute clusters is more based on kinetics than thermodynamics. On the other hand, Almirall, et al. [48] investigated the stability of Si-Mn-Ni nanolcusters in neutron-irradiated RPV. These solute clusters were found to be thermodynamically stable upon post irradiation annealing at 425 °C, which is ~135 °C higher than typical RPV service conditions and is consistent with predictions of the CALPHAD thermodynamic database simulation carried out by Xiong, et al. [49].

The objective of this work is to characterize the evolution of microstructure in the commercial F/M alloy T91 following irradiation with either neutrons or Fe^{2+} ions to otherwise similar conditions (3 dpa at 500 °C), enabling isolation of the dose rate effects. Characterization is also conducted following Fe^{2+} irradiation to 100 dpa at 500 °C to evaluate effects at higher dose. TEM is used to quantify any changes in grains, carbides, or dislocation density, and any dislocation loop or void morphology following each irradiation. Clusters rich in Si-Mn-Ni solutes and Cu and any solute segregation to sinks are characterized using atom probe tomography (APT), providing a reasonable comparison of the irradiation-induced nanocluster evolution upon irradiation with each particle to a relatively low dose. The evolution of Si-Mn-Ni-rich nanoclusters at low dose conditions is then modeled using cluster dynamics, followed by a comprehensive sensitivity analysis for each input parameter for the model. The collection of additional experimental data coupled with cluster dynamics modeling provide additional insight into the irradiation-induced microstructures of T91.

Methods and Materials

Materials and Irradiations

The focus of this study is the commercial F/M alloy T91, with composition [50] (nominally 9Cr-MoVNb). The final heat treatment for T91 involves austenitizing at 1040 °C for 1 hour followed by air-cooling, then tempering at 760 °C for 60 min followed by air cooling. T91 exhibits a martensitic structure with small laths on the order of ~0.4 μm wide and ~0.8 μm long and dislocation densities of ~10^{15} m^{-2} (Table 3.2).

Table 3.1. Chemical composition of commercial F/M alloy T91 (balance Fe), from [50].

-	C	N	Al	Si	P	S	V	Cr	Mn	Ni	Cu	Nb	Mo
wt%	0.1	0.05	0.02	0.28	0.01	0.003	0.22	8.37	0.45	0.21	0.17	0.08	0.90
at%	0.46	0.19	0.045	0.55	0.016	0.005	0.23	8.90	0.45	0.20	0.15	0.05	0.52

Specimens were prepared from the same heat of alloy T91 for irradiation with fast neutrons to 3 dpa at ~10^{-7} dpa/s, and 5 MeV Fe^{2+} irradiation to 3 dpa and 100 dpa at 2.2 x 10^{-4} dpa/s. Each irradiation was carried out at 500 °C as part of the same campaign executed for a similar study of HCM12A, HT9, and a model Fe-9%Cr ODS alloy in [6,23]. For the Fe^{2+} irradiations, specimens were cut via electrical discharge machining into 1.5 mm x 1.5 mm x 20 mm bars. The bars were each mechanically polished using SiC paper up to 4000 grit and subsequently electropolished for ~20 seconds in a 10% perchloric acid +90% methanol solution at -40°C with an applied potential of 35 V between the specimen (anode) and platinum mesh cathode.

The Fe^{2+} irradiation was conducted at the Michigan Ion Beam Laboratory using a raster-scanned beam in the General Ionex Tandetron accelerator. The Stopping and Range of Ions in Matter (SRIM) software [51] was used to calculate displacement damage for the self-ion irradiation using a displacement energy of 40 eV. The full damage profile using the "Quick Calculation (K-P)" mode is found in Fig. 3.2 with the damage peak located at ~1.2 μm for Fe^{2+} irradiation. Microstructural characterization was targeted at depths of 400 - 600 nm in the Fe^{2+} irradiated specimens to avoid any surface effect and the steep irradiation dose gradient near the damage peak.

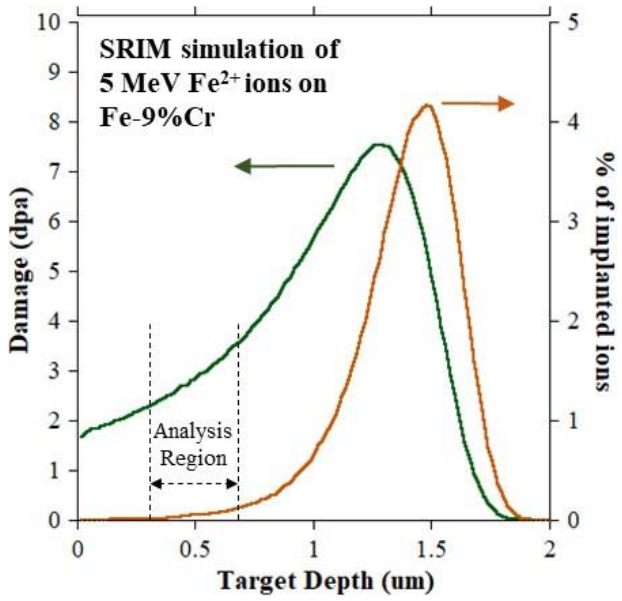

Figure 3.2. SRIM simulation of the damage and ion implementation profiles for 5 MeV Fe^{2+} ions incident to Fe-9%Cr in "Quick Calculation (K-P)" mode.

The neutron irradiation specimen was cut into a 3 mm diameter disc, approximately 150 - 200 μm thick. The disc was also mechanically polished through 4000 grit SiC paper, followed by electropolishing at -30 °C. The disc was irradiated to a dose of 3 dpa in a fast neutron spectrum (~10^{-7} dpa/s) in the Advanced Test Reactor (ATR) at Idaho National Laboratory. The irradiation temperature of 500 °C was determined with SiC electrical resistivity samples enclosed in experiment capsules; thermal models, in which the gas–gap distance was adjusted, correlated the SiC experimental data.

Transmission Electron Microscopy

TEM characterization is done to evaluate microstructure evolution following both Fe^{2+} and neutron irradiation. Grains, carbide precipitates, and dislocations networks are evaluated for any irradiation-induced evolution, while any irradiation-induced dislocation loops and voids are quantified for comparison. TEM lamellae are prepared from each specimen (including an as-received sample) using an FEI Quanta 3D FEG focused ion beam (FIB) at the Center for Advanced Energy Studies (CAES). Each specimen surface is coated with ~3 μm of platinum deposit prior to trenching and lifting out an ~2 μm thick x 20 μm long sample for mounting on a copper grid. The samples are then milled to ~100 nm thickness using 30 kV ions, before eventually milling each side with 5 kV ions to reduce the thickness to ~50-100 nm. Each side is finally cleaned with 2 kV ions to minimize any milling damage on the surface. TEM sample preparation and imaging are identical to the process used in [52] to ensure consistency in approaches for comparison.

Each specimen is imaged using an FEI Tecnai TF30-FEG scanning transmission electron microscope (STEM) at CAES. Grains, carbide precipitates, dislocations, loops, and any voids are imaged at varying magnifications to enable measurement of average size and number density. For statistical comparison, the standard deviation (σ) is determined for each size measurement and the standard deviation of the mean is determined ($\sigma/\sqrt{N}$), with N as the total number of a given feature measured. Microstructure features with a volumetric number density (carbides, dislocation loops, and voids) require an estimated thickness of the lamellae, which is measured using electron energy loss spectroscopy (EELS).

While all of the grains, carbides, and dislocations are imaged in bright field mode, dislocation loops are imaged using a combination of bright field imaging and STEM imaging using an accepted procedure outlined by Parish, et al. [53] with each grain of interest tilted to a low index zone axis. The STEM approach enables a “bright field” image with reduced contrast and without any hidden reflections. Identification of the loops within the images are aided by loop orientation maps developed by Yao, et al. [54], which also enables an analyst to distinguish which loops reside on the {001} and {111} habit planes, respectively. For loops imaged on edge, the longer dimension is taken as the loop diameter [54].

Atom Probe Tomography

Atom probe tomography (APT) is particularly suitable for characterizing the composition and morphology of nanoclusters within alloys, and has been shown to provide increased resolution of such nanoscale phases over TEM [55]. Needle shaped samples were prepared from the irradiated specimens using focused ion beam (FIB) milling on a Quanta 3D 200i dual beam scanning electron microscope at the Center for Advanced Energy Studies (CAES). The fabrication techniques including sample wedge liftout, mounting onto silicon posts, partitioning into 6-10 samples, and milling with annular ring patterns to a tip radius ≤50 nm, consistent with the methods described in [56].

Each APT needle was analyzed with a Cameca Instrument LEAP 4000X HR in laser pulsed mode with samples cooled to 50 K, a pulse repetition rate of 200 Hz, and laser pulse energy of 50 pJ. These parameters were selected based on similar sample experience from the LEAP operator at CAES with the goal to reduce risk of early fracture of the samples

during evaporation. The data from each evaporation is reconstructed and analyzed using the Integrated Visualization and Analysis Software (IVAS) Version 3.8.4. For reconstruction, values for the image compression factor (ICF) and the k-factor are often complicated to determine. The ICF values for each reconstruction are determined using the new pole indexing module in IVAS. In reality, automatic pole indexing from the detector histogram was typically unreliable, since there is typically not enough poles visible in each detector histogram. However, it is possible to achieve more accurate indexing through manually initiating the indexing by drawing bands on the visible detector histogram using the manual band option available in IVAS. Once a few bands are present, the software is more successful at indexing the crystallographic poles. The information obtained from the pole indexing enables identification of the ICF for reconstruction. A representative example of completed pole indexing in IVAS from a T91 APT data set is provided in Fig. 3.3. The ICF values used in this study ranged between 1.43 and 1.53, while field k-factors were 3.30 for each data set. Reconstruction of each data set is created using "Voltage" mode in IVAS, with each reconstruction visually compared to the corresponding SEM image of the sample tip to ensure the overall shape is consistent. The elements were identified via their mass-to-charge ratios and the overall isotope abundance of the species known to be present in the composition of the alloy. Peak overlap occurs in a number of places such as at a mass-to-charge ratio of 29, which is likely made up of a combination of $^{58}Fe^{2+}$ and $^{58}Ni^{2+}$ ions. In this case, the peak is identified at $^{58}Fe^{2+}$ since the majority of these ions are found to be of Fe using peak deconvolution. This approach enables consistent and repeatable ranging between each specimen. The size of the data sets ranged from ~4 – 24 million ion counts per needle.

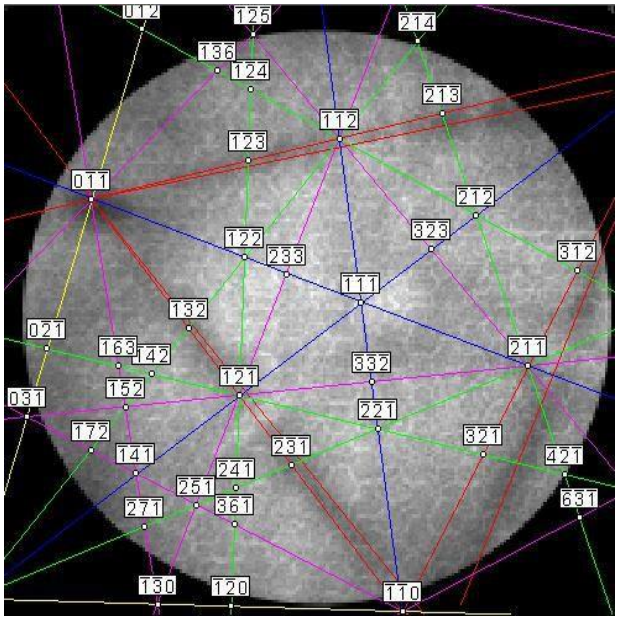

Figure 3.3. A representative example of pole indexing using the detector density map in IVAS version 3.8.4 for a T91 APT data set.

The maximum separation method was used [57] to perform cluster analysis in IVAS. The accuracy of cluster analysis depends primarily on the selection of two parameters, d_{max} and N_{min}. The approach used for this study follows those of [58,59]. While attempting to optimize the values for d_{max}, a common phenomenon is observed in which a bimodal distribution of possible cluster counts was observed. Too small of values for d_{max} will split a single cluster into multiple identified clusters, while too large of values for d_{max} provide a greater chance of spuriously identifying clusters in the matrix. Therefore, the optimum values for d_{max} and N_{min} are selected to identify only the clusters and not the nearby matrix, as well as to reduce the identification of random clusters in each reconstruction. The d_{max} and N_{min} values range from 0.4 – 0.95 and 10 – 90, respectively. Each result is visually inspected to confirm the identified clusters are consistent with those identified with isosurfaces created

with an ~3 - 6% concentration threshold, and those visible in the reconstruction images. In many cases, strong evidence of solute segregation to dislocations, dislocation loops, and grain boundaries are observed, and these features can also be spuriously identified as large clusters. When this occurs, false clusters due to segregation are removed from the cluster analysis and are not counted as clusters.

The cluster radii, number densities, and volume fraction of clusters under different irradiation conditions were obtained from the IVAS cluster analysis output .cvs files, which provide values for R_{gx}, R_{gy}, and R_{gz} from each cluster. The effective radius of gyration (R_g) for each cluster was calculated using [60]:

$$R_g = \sqrt{{R_{gx}}^2 + {R_{gy}}^2 + {R_{gz}}^2} \quad (1)$$

where R_{gx}, R_{gy}, and R_{gz} are radius of gyration in each coordinate direction. The Guinier diameter (D_G) for each cluster was determined using [60,61]:

$$D_G = 2\sqrt{\frac{5}{3}}R_g \quad (2)$$

The nanocluster number density (N_{nc}) is determined by:

$$N_{nc} = \frac{\sum N_c}{\sum V_T} \quad (3)$$

where $\sum N_c$ is the total number of clusters identified in all tips from a specific specimen and $\sum V_T$ is the total analyzed volume in all tips from that specimen. The volume fraction of clusters (f_v) is:

$$f_v = \frac{\sum N_{cl}}{N_{tot}} \quad (4)$$

Where N_{cl} is the total number of atoms in the measured clusters and N_{tot} is the total number of atoms in the combined reconstructed volumes from all samples [5]. The IVAS output file also includes detailed composition of each cluster and the matrix, enabling simple determination of the surrounding matrix composition (c_m^i) and the total specimen composition (C_i).

Results

Transmission electron microscopy

Typical microstructures for T91 with grains, carbide precipitates, and dislocation networks are illustrated in Fig. 3.4 for each specimen, while a summary of the TEM microstructure measurements are provided in Table 3.2. This data enables the comparison of microstructure evolution across two different particle irradiations to otherwise similar conditions (3 dpa at 500 °C) and across two dose levels (3 dpa and 100 dpa) for Fe^{2+} ion irradiation. Using EELS, TEM lamellae thicknesses were found to average 75 nm, 69 nm, 149 nm, and 80 nm for the as-received, neutron-irradiated, Fe^{2+} irradiated to 3 dpa, and Fe^{2+} irradiated to 100 dpa, respectively.

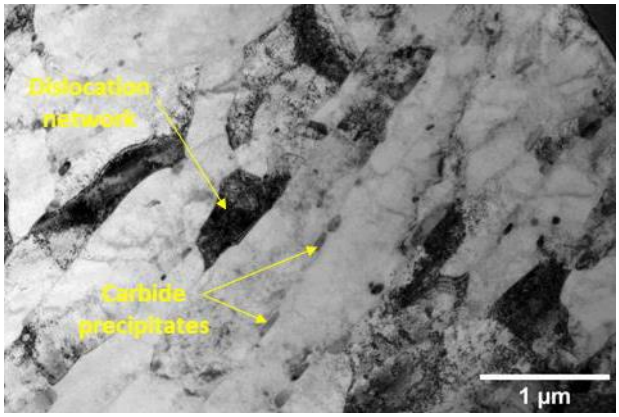

Figure 3.4. Representative bright field TEM image of T91 microstructure of grains, carbides, and dislocations in T91. The image shown is from the specimen irradiated with fast neutrons to 3 dpa at 500 °C.

Table 3.2. Summary of microstructure measurements in T91 for each specimen using TEM. All irradiations conducted at 500 °C.

Feature	**Measurement**	**As-received**	**Neutrons 3 dpa**	**Fe^{2+} ions 3 dpa**	**Fe^{2+} ions 100 dpa**
Grains	# of grains measured	20	152	104	104
	Effective diameter (x 10^{-6} m), d_g	0.59	0.60	0.60	0.61
	Std. deviation for d_g	0.17	0.23	0.12	0.11
	Std dev. of the mean for d_g	0.04	0.02	0.01	0.01
Dislocation lines	# of measurements	6	8	19	15
	Density (x 10^{14} m^{-2})	13.9 ± 6.2	16.0 ± 7.7	16.6 ± 6.6	17.2 ± 4.0
Carbide precipitates	# of carbides measured	45	97	115	146
	Effective diameter (x 10^{-6} m), d_c	0.10	0.09	0.08	0.09
	Std. deviation for d_c	0.04	0.04	0.03	0.04
	Std dev. of the mean for d_c	0.006	0.005	0.003	0.003
	Density (x 10^{20} m^{-3})	0.5 ± 0.3	0.3 ± 0.5	0.4 ± 0.1	0.6 ± 0.1
Voids	# of voids measured	0	0	0	0
Dislocation loops	# of loops measured	0	166	98	97
	Effective diameter (x 10^{-9} m), d_l	-	11.2	10.4	13.2

	Std. deviation for d_l	-	4.0	3.6	3.9
	Std dev. of the mean for d_l	-	0.31	0.32	0.40
	Density (x 10^{21} m^{-3})	-	1.2 ± 1.3	0.6 ± 0.1	1.6 ± 0.7
	½<111> loops %	-	38%	43%	44%

A minimum of 20 grains and the carbide precipitates within the grains are measured for each specimen, with grains and carbides exhibiting very little change upon irradiation. The grains and carbides are found to have effective diameters ranging 0.59 – 0.61 μm and 0.08 – 0.10 μm, respectively, while each of these effective diameter measurements are well within the standard deviation measurements. Dislocation line networks are also found to be statistically invariant, with densities ranging 13.2 – 17.7 x 10^{-4} m^{-2} and standard deviations as high as 7.2 x 10^{-4} m^{-2}. These results suggest these features have not tangibly evolved as a response to either neutron or self-ion irradiation. This observation is consistent with results found upon similar irradiations of F/M alloys HCM12A and HT9 [52]. No voids are observed in any of the irradiated specimens, including the Fe^{2+} ion-irradiated sample exposed to 100 dpa. This is plausible given that no He pre-implantation was conducted prior to this irradiation, and the irradiation temperature of 500 °C. For comparison, Getto et al. only found small voids in Fe^{2+} ion-irradiated T91 at an even lower temperature (460 °C) only after 130 dpa [34].

The average size of dislocation loops are relatively consistent after 3 dpa irradiations with neutrons (11.2 ± 4.0 nm) and Fe^{2+} ions (10.4 ± 3.6 nm). These standard deviations are large enough for significant overlap, while the standard deviation of the mean values are only

0.31 – 0.32 nm. Loop densities following neutron irradiation (1.2 x 10^{21} m^{-3}) are also higher than Fe^{2+} irradiation (0.6 x 10^{21} m^{-3}) to 3 dpa, but given a standard deviation of 1.3 x 10^{21} m^{-3}, it is not clear if there is any statistical difference. Meanwhile, dislocation loops after 100 dpa self-ion irradiation are slightly larger at 13.2 ± 3.9 nm (with a standard deviation of the mean of 0.40 nm) and have a density of 1.6 x 10^{21} m^{-3}. Micrographs of representative dislocation loop distributions are illustrated in Fig. 3.5, along with an illustrated summary of the dislocation loop size and number density results in Fig. 3.5d. For all irradiation conditions, dislocation loops with Burgers vectors a<100> and a/2<111> are identified, although in many cases it can be challenging to clearly distinguish between loops with oblong aspect ratios (as illustrated in Fig. 3.5b). In our estimation, the majority of the loops are found to be a<100>, which is consistent with HCM12A and HT9 following the same irradiations [52].

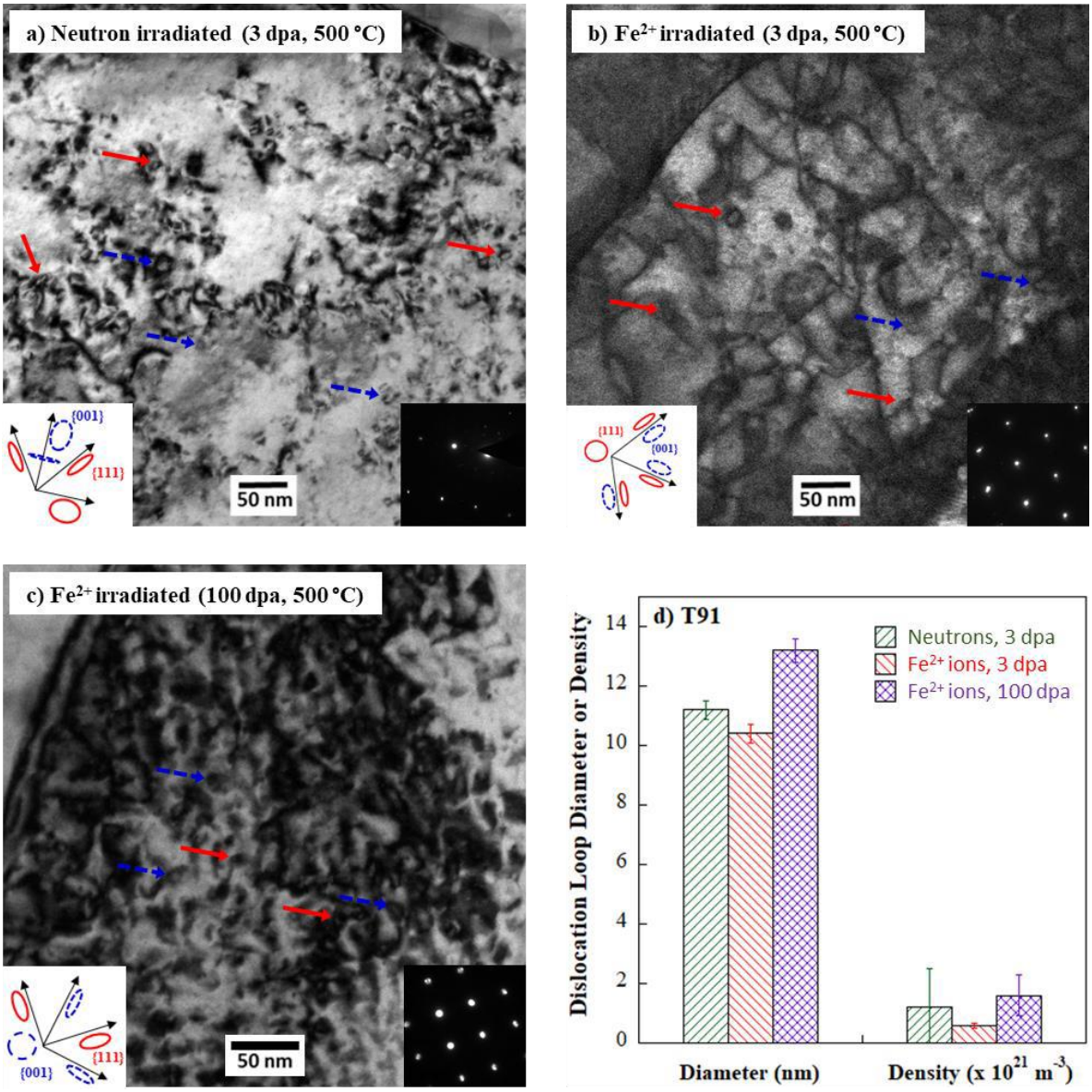

Figure 3.5. Representative dislocation loops in T91 for a) neutron-irradiated to 3 dpa imaged on the [011] zone axis, b) Fe2+ irradiated to 3 dpa imaged on the [111] zone axis, and c) Fe2+ irradiated to 100 dpa imaged on the [001] zone axis, plus d) comparison of loop diameter and density for each condition. Error bars for loop diameter are standard deviation of the mean.

Atom probe tomography

Representative solute distributions of Si, Mn, Ni, and Cu atoms for each specimen of T91 are presented in Fig. 3.6. The three dimensional reconstructions of T91 following Fe^{2+} and neutron irradiation to 3 dpa at 500 $^{\circ}$C each exhibit clustering of Si-Mn-Ni and Cu solutes at adjacent locations. The co-location of these clusters is consistent with prior studies of irradiated T91 [18] and HCM12A [6,17]. Each irradiation to 3 dpa reveals the presence of approximately spherical clusters as well as strong evidence of solute segregation to sinks including dislocation loops, dislocation lines, and grain boundaries. No clustering or segregation of Si-Mn-Ni is detected in any of the Fe^{2+} irradiated (100 dpa) samples, but evidence of Cu clustering is present on the edges of a few samples and one Cu-rich cluster is clearly identified in one of the samples. This lack of clustering at 100 dpa is consistent with the same irradiation conditions for HCM12A and HT9 [6]. However, HCM12A and HT9 also exhibited segregation to grain boundaries at 100 dpa, which is not observed here in T91. This lack of segregation in T91 may be due to the low analysis volume, with none of the 6 APT reconstructions coinciding with a grain boundary. Finally, no evidence of any Cr clustering (α') is observed in any of the specimens, consistent with [17] and not surprising given the concentration of Cr is less than the ~9% solubility limit for Cr in α-Fe.

a) Neutrons (3 dpa)

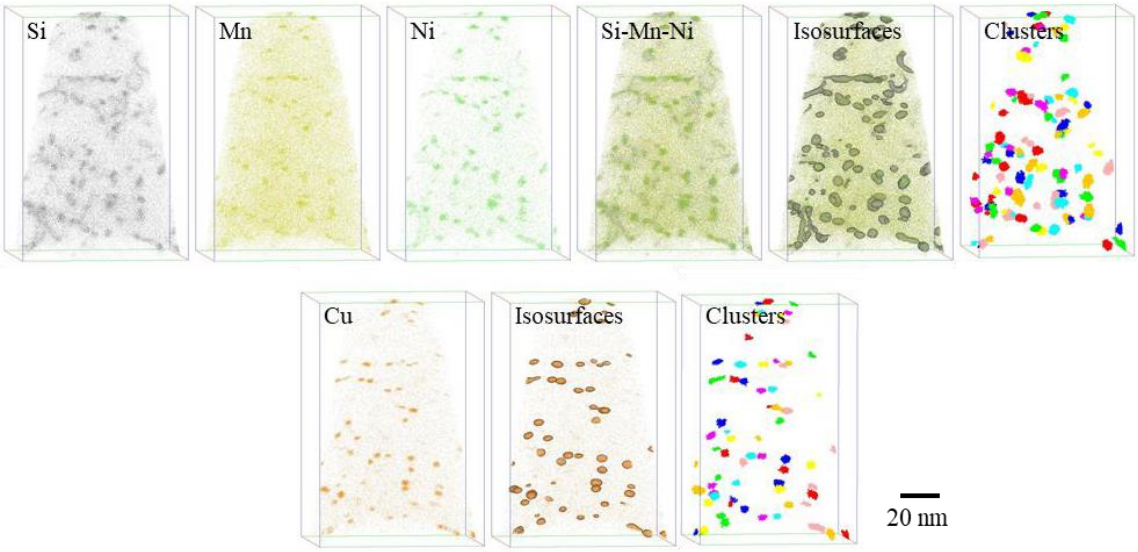

b) Fe^{2+} ions (3 dpa)

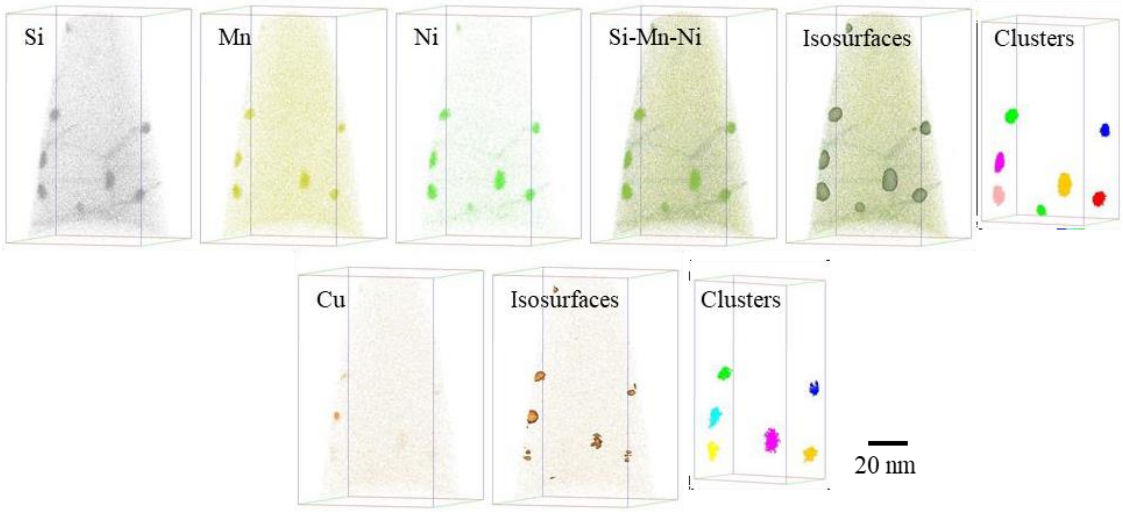

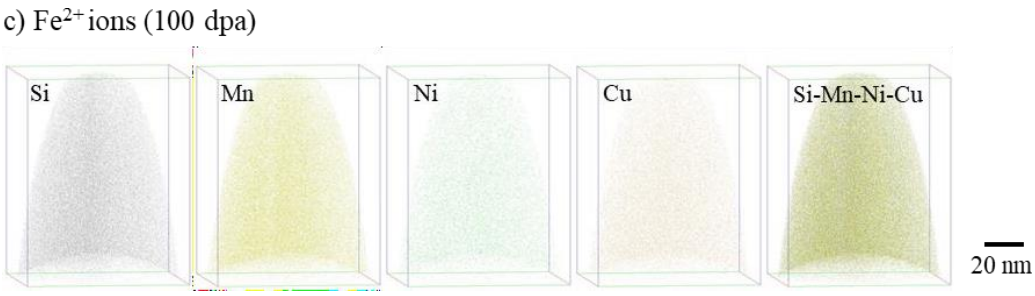

Figure 3.6. Atom probe distribution maps and cluster analysis results for Si-Mn-Ni and Cu solutes following a) neutron irradiation to 3 dpa, b) Fe2+ irradiation to 3 dpa, and c) Fe2+ irradiation to 100 dpa. All irradiations are at 500°C.

Quantitative cluster analysis results enabling comparison across each irradiation are provided in Table 3.3 and illustrated in Fig. 3.7. A total of 219 and 8 Si-Mn-Ni-rich clusters are identified and measured in the specimens irradiated with neutrons and Fe^{2+} ions (both at 3 dpa), respectively. Self-ion (Fe^{2+}) irradiation induces the largest average size of these nanoclusters at 7.59 ± 1.50 nm, while clusters after neutron irradiation are 4.78 ± 1.63 nm. Meanwhile, the number density of these clusters is lower after Fe^{2+} irradiation to 3 dpa (12 x 10^{21} m^{-3}) compared to neutrons irradiation (145 x 10^{21} m^{-3}). Additionally, a total of 151 and 9 Cu-rich clusters are identified following neutron irradiation and Fe^{2+} irradiation (both to 3 dpa), respectively. In a similar trend, Cu-rich clusters are larger following Fe^{2+} irradiation (7.54 ± 2.32 nm) than neutron irradiation (4.18 ± 1.07 nm), while number density after neutron irradiation is higher (100 x 10^{21} m^{-3}) than after Fe^{2+} irradiation (14 x 10^{21} m^{-3}). The combined matrix compositions of Si, Mn, and Ni (c_m^{SiMnNi}) solutes increase from 0.88 at% to 1.20 at% following neutron and Fe^{2+} irradiation to 3 dpa, respectively, and is inversely related to the corresponding volume fractions of clusters for each irradiation (Table 3.3),

confirming that the clustering elements have migrated from the matrix toward the clusters. Similarly, matrix compositions of Cu (c_m^{Cu}) increase from 0.10 at% to 0.14 at% following the same irradiations, respectively. The matrix compositions following Fe^{2+} irradiation to 100 dpa are 1.24 at% and 0.15 at% for Si-Mn-Ni and Cu solutes, respectively, and are a close match to the expected overall material compositions from Table 3.1, providing further evidence of solute redistribution and suggesting any possible segregation to grain boundaries after 100 dpa may not be significant.

Table 3.3. Summary of cluster analysis of T91 for each irradiation at 500 °C using APT.

Nanocluster Analysis	**Neutrons 3 dpa**	**Fe^{2+} ions 3 dpa**	**Fe^{2+} ions 100 dpa**
Analysis Volume, V_T (nm^3)	1,507,647	658,876	1,366,071
Si-Mn-Ni-rich clusters			
# of clusters measured, $\sum N_{cl}^{SiMnNi}$	219	8	-
Average diameter, D_G^{SiMnNi} (nm)	4.78	7.59	-
Standard deviation for D_G^{SiMnNi}	1.63	1.50	-
Std. dev. of the mean for D_G^{SiMnNi}	0.11	0.53	-
Density, N_{nc}^{SiMnNi} (x 10^{21} m^{-3})	145	12	-
Volume fraction, f_v	1.48%	0.48%	-
Solute matrix composition, c_m^{SiMnNi}	0.88 at%	1.20 at%	1.24 at%
Cu-rich clusters			
# of clusters measured, $\sum N_{cl}^{Cu}$	151	9	1
Average diameter, D_G^{Cu} (nm)	4.18	7.54	-
Standard deviation for D_G^{Cu}	1.07	2.32	-
Std. dev. of the mean for D_G^{Cu}	0.09	0.77	-
Density, N_{nc}^{Cu} (x 10^{21} m^{-3})	100	14	-
Volume fraction, f_v	0.70%	0.32%	-
Solute matrix composition, c_m^{Cu}	0.10 at%	0.14 at%	0.15 at%

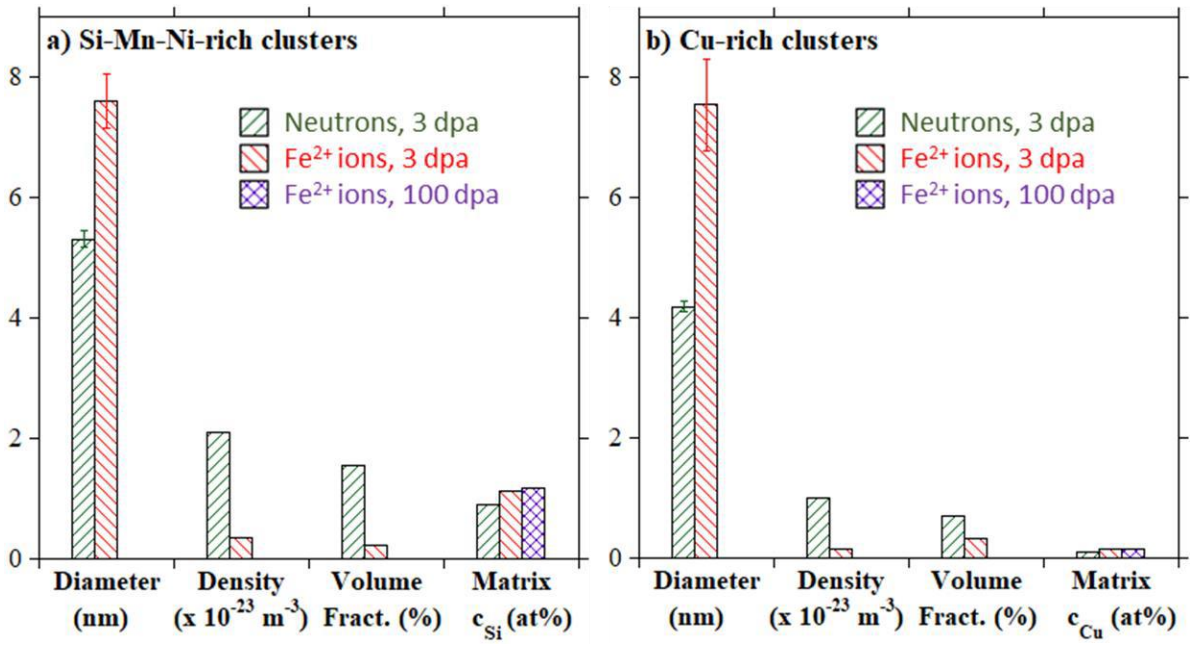

Figure 3.7. Summary of nanocluster morphologies and solute matrix compositions following neutron or self-ion irradiation of T91 for a) Si-Mn-Ni-rich nanoclusters, and b) Cu-rich nanoclusters.

Within the neutron-irradiated specimen, segregation is clearly visible on multiple dislocation loops and a grain boundary in the APT reconstructions. A representative scan across one dislocation loop in the neutron-irradiated specimen is illustrated in Fig. 3.8a, showing Si, Mn, Ni, and Cu enrichment with ΔSi~3.33 at%, ΔMn~0.62 at%, ΔNi~0.84 at%, and ΔCu~1.01 at%, while Fe is depleted with ΔFe~-6.3 at% at the dislocation loop. A linescan across a grain boundary (Fig. 3.8b) shows enrichment of Si, Ni, and Cu with ΔSi~2.16 at%, ΔNi~0.34 at%, and ΔCu~0.13 at%. Meanwhile, Mn and Fe are slightly depleted with ΔMn~-0.13 at%, and ΔFe~-1.9 at%. For each species, enrichment at the dislocation loop (or depletion of Fe) appears to be more pronounced than it is at the grain

boundary. Similar segregation to a grain boundary and multiple dislocation lines is observed in the Fe^{2+} (3 dpa) specimen. A linescan across a grain boundary (Fig. 3.8c) exhibits enrichment of Si, Ni, and Cu with ΔSi~2.57 at%, ΔNi~1.00 at%, and ΔCu~0.13 at%; Mn and Fe are depleted with ΔMn~-0.26 at% and ΔFe~-4.4 at%. Finally, a representative linescan across a dislocation line is shown in Fig. 3.8d. Enrichments of Si, Mn, Ni, and Cu are observed with ΔSi~3.04 at%, ΔMn~0.48 at%, ΔNi~0.69 at%, and ΔCu~2.39 at%, while Fe is depleted with ΔFe~-6.8 at%. In comparing the two grain boundaries, segregation is consistently more pronounced following Fe^{2+} irradiation. Meanwhile, enrichments of Si, Mn, and Ni at dislocations is more pronounced following neutron irradiation, but Cu enrichment and Fe depletion are more prominent after ion irradiation at the dislocations. Interestingly, Mn is enriched at dislocations, but is seen to deplete on the grain boundaries following both irradiations. From each of the four linescans, Cr appears to demonstrate local fluctuations in concentration at or near the sinks, but any specific enrichment or depletion at the boundaries or dislocations is not distinctly clear. Taller et al. reported a similar comparison of segregation of Si and Ni on grain boundaries following dual ion irradiation or neutron irradiation in BOR-60 at different irradiation conditions [32]. There is also evidence of denuded regions adjacent to the grain boundaries which is free of Si-Mn-Ni-rich and Cu-rich clusters (Fig. 3.8b and Fig. 3.8c). A summary of the segregation peak concentrations (in at%) and changes from matrix compositions is provided in Table 3.4.

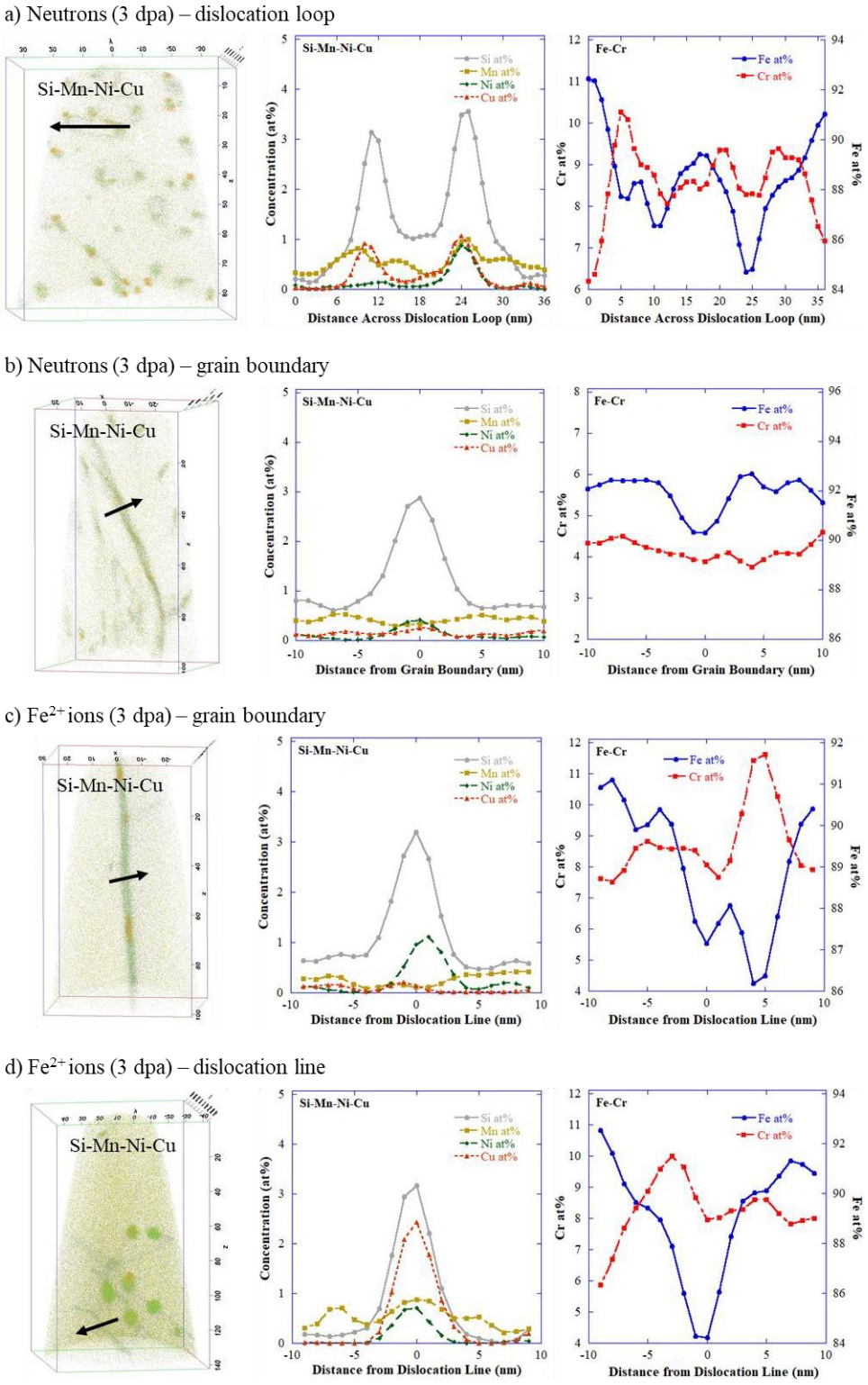

Figure 3.8. Representative linescans and radiation-induced segregation profiles following neutron irradiation to 3 dpa across a) dislocation loop, b) grain boundary, and across a c)

grain boundary, and d) dislocation line following Fe2+ irradiation to 3 dpa. All irradiations conducted at 500 °C.

Table 3.4. Summary of segregations measurements including peak concentrations (in at%) and changes from matrix compositions across different features in T91.

Irradiating particle	**Dose**	**Feature**	**Si**	**ΔSi**	**Mn**	**ΔMn**	**Ni**	**ΔNi**	**Cu**	**ΔCu**	**Fe**	**ΔFe**
Neutrons	3	Dislocation loop	3.55	3.33	1.00	0.62	0.88	0.84	1.07	1.01	84.7	-6.3
Neutrons	3	Grain boundary	2.88	2.16	0.30	-0.13	0.41	0.34	0.26	0.13	90.3	-1.9
Fe^{2+} ions	3	Grain boundary	3.20	2.57	0.09	-0.26	1.11	1.00	0.21	0.13	86.2	-4.4
Fe^{2+} ions	3	Dislocation line	3.17	3.04	0.88	0.48	0.71	0.69	2.43	2.39	84.2	-6.8

Discussion

Dislocation loop evolution

Dislocation loops are present after both neutron and Fe^{2+} irradiation to 3 dpa, with most loops observed to be relatively small ranging 6-18 nm in diameter, and consistent between the two irradiations. As dose for the Fe^{2+} irradiation increases to 100 dpa, loop size only increases ~25%, supporting the theory of defect cluster saturation from Whapham and Makin [62]. This result is also consistent with other F/M alloys [63,64], including HCM12A and HT9 following the same irradiation conditions [6]. The densities of loops following each 3 dpa irradiation are also comparable, with some wider variation in our measurements. This variation is likely due to differences in the TEM lamellae thickness, which influences the

quality of STEM imaging and thus, the visibility of loops. Evidence of this effect is found in Fig. 3.5b, in which a thicker lamellae produces less contrast and adversely affects loop detectability.

Consistent loop morphologies between Fe^{2+} and neutron irradiation to 3 dpa suggests that Fe^{2+} irradiation can produce results comparable to neutron irradiation at this low dose. At higher doses of ~17 dpa and ~35 dpa, Taller, et al. found that Fe^{2+} (plus He^{2+}) irradiation with a positive temperature shift of ~60 °C produced results comparable to neutron irradiation to the same doses [32]. Each of these outcomes suggest that nucleation and growth of loops are recombination-driven, requiring only a small temperature shift as prescribed by the invariance theory. Such a temperature shift may not yet be discernable from the results herein due to the low dose of only 3 dpa. Liu et al. [12] also observed that no temperature shift for 1 MeV Kr irradiation to emulate neutron irradiation hardening due to loop formation in T91 irradiations up to 7 dpa at temperatures ranging 300-500 °C. However, it is important to note their irradiations were conducted *in situ* on a thin TEM lamellae which could influence dislocation loop formation and also point defect and loop migration to the sample surfaces differently from bulk irradiated material.

For each of the irradiation conditions in this study, the majority of loops are a<100> (Table 3.2). Both Schaublin, et al. [65] and Yao, et al. [54] previously found that loop orientations transition to favoring a<100> at higher irradiation temperature, such as 500 °C in this study. Liu, et al. [12] confirmed this transition, with mostly a<100> loops following their *in situ* Kr irradiation of T91 at 500 °C to doses ranging 1-7 dpa. These results are also similar to Taller, et al. [32], who found that loops were mainly a<100> in both neutron and Fe^{2+} irradiation at 376-570 °C up to 35 dpa, and the favorability of a<100> loops in bcc Fe is

simulated effectively by Dudarev, et al [66]. In comparison with another F/M alloy (HT9), Zheng, et al. [38] found a<100> to be more favorable at higher temperatures. In another study, Zheng, et al. [37] observe that numbers of a<100> and a/2<111> loops were similar at low dose (~4 dpa) up to 470 °C, but were mostly a<100> as dose increased to 20 dpa. All of these observations are consistent with the results herein.

Solute clustering and segregation

Both irradiations with either neutrons or Fe^{2+} ions to 3 dpa demonstrate strong evidence of radiation-induced segregation (RIS) to sinks including grain boundaries, dislocation loops, and dislocation lines. The phenomena of RIS is also exhibited in prior studies of irradiated T91 [32,67]. In fact, irradiation-induced enrichment of Si, Mn, and Ni at nanocluster interfaces is previously observed in a model Fe-9%Cr ODS alloy with Y-Ti-O-rich oxides [23]. Vacancy solute drag is likely the dominant flux-coupling mechanism responsible for solute segregation to sinks as well as irradiation-enhanced or induced solute precipitation in F/M alloys. Because of the supersaturated point defects generated during irradiation, vacancies diffusing to sinks carry along with them solute atoms causing enrichment on features such as dislocation loops or grain boundaries [68,69]. Furthermore, it is likely that Cu solutes precipitate more readily in the matrix (due to its low solubility in Fe), followed by the Si, Mn, and Ni enrichments adjacent to the Cu-rich clusters, resulting in semi-spherical solute clusters thoughout the matrix.

Interestingly, the solutes are mostly redistributed after Fe^{2+} irradiation to 100 dpa. Wharry, et al. [18] also observed evidence of redistribution with proton irradiation, although

at a much lower dose of 10 dpa, at 400 °C. The trend for redistribution of nanoclusters at high dose is also consistent with prior studies of HCM12A and HT9 with the same irradiation conditions [6], although both HCM12A and HT9 still exhibit RIS to grain boundaries at the high dose. In any case, the redistribution of solutes suggest that any clustering at low dose may not represent steady-state for Fe^{2+} irradiation.

For evaluating dose rate dependence on nanocluster evolution within the matrix, we are limited to one comparison of data points at the same dose and temperature (3 dpa at 500 °C) with either Fe^{2+} ion (2.2×10^{-4} dpa/s) or fast neutrons ($\sim 10^{-7}$ dpa/s). Given the stark differences in both average size and number density (Table 3.3) following each irradiation, Fe^{2+} ions do not appear to emulate neutrons effectively at this low dose. The variance exhibiting coarser clusters following Fe^{2+} irradiation is consistent with the same irradiation conditions in both HCM12A and HT9 [6] as well. Furthermore, Zheng et al. [38] found that nanocluster coarsening appear to be directly dependent on temperature in neutron irradiated HT9, with larger, less dense clusters corresponding to higher irradiation temperatures. If this same relationship transfers to T91, it would follow that neutron irradiation at higher temperature or Fe^{2+} irradiation at lower temperature (both equating to a negative temperature shift) would be required to achieve more closely matching nanocluster evolution results. Clearly, there is not enough data here to make a definitive determination, but it is also worth noting that the data does not appear to fall in line with the invariance theory either.

Cluster Dynamics Simulations

For this study, we employ a cluster dynamics (CD) model to describe nucleation and evolution of Si-Mn-Ni precipitates in F/M alloys. Although it is not clear if the clusters observed in this study are specifically G-phase precipitates, the chosen CD model is identical to those previously used to describe cluster evolution in both neutron-irradiated RPV steels [42] and previously proton-irradiated T91 [43]. This model assumes Si-Mn-Ni have equilibrium composition of $Ni_{16}Si_7Mn_6$ which is similar to G-phase. This phase is predicted by CALPHAD thermodynamic database (TCAL3) and it is predicted to be stable up to 500 °C [43]. The model includes embedded routines for determining radiation-enhanced diffusion (RED) and thermodynamic heterogeneous nucleation. The cluster dynamic master equations are [42,43,70]:

$$\frac{\partial f}{\partial t} = R_{het}(n,t) + J_{n-1\rightarrow n} - J_{n\rightarrow n+1} \quad (5)$$

$$J_{n\rightarrow n+1} = \omega^{+}_{n,n+1} f(n.t) - \omega^{-}_{n+1,n} f(n+1,t) \quad (6)$$

which describe the evolution of the size distribution and mole fraction (*f*) of G-phase precipitates as a function of fluence, temperature, and alloy composition. The co-efficient $\omega^{(+)}_{n,n+1}$ is the rate at which clusters of size *n* absorb single atoms to grow to size *n+1*, while the co-efficient $\omega^{(-)}_{n+1,n}$ is the rate at which clusters of size *n+1* emit single particles to shrink to size *n* [42]. In this model, it is assumed that clusters grow and shrink by the absorption and emission of pseudo-monomer molecules consisting of Si, Mn, and Ni. The underlying mechanism is that the generation of a high concentration of point defects in the cascades leads to the formation of defect-solute cluster complexes as a result of defect-solute binding

energies and local radiation-induced segregation (RIS) [42]. Furthers details on this model as well as the parameters used can be found in refs [42,43].

Prior to simulating the irradiation conditions in this study, we used the CD model to recreate the simulation of J.H. Ke, et al. [43] modeling proton irradiation effects on T91. Successful duplication of these results ensured that our approach is consistent and comparable to prior literature. A summary of the parameters used for the CD model set up are presented in Table 3.5. The majority of these parameters are identical to those used in [42] for simulation of G-phase clusters in RPV steels upon neutron irradiation, with just a few exceptions. To adapt the model for simulating Fe^{2+} irradiation, a similar value for the cascade efficiency (i.e. fraction of vacancies and self-interstitial atoms created per dpa) of 0.4 is used on the basis of the multiple subcascades generated by high PKA energies produced by heavy ions and neutrons [71]. At the same time, a different value for the flux effect scaling exponential factor (p) was estimated. While we used $p = 0.2$ for neutron irradiation (consistent with [42]), we found that a value of $p = 0.3$ enabled successful duplication of the proton irradiation simulation results in [43]. Therefore, we initially estimated a higher value of $p = 0.5$ to account for the higher dose rate associated with Fe^{2+} irradiation while also considering the likely high rate of defect recombination [72]. The dislocation sink strength for T91 was chosen to be identical to the value used in [43] to enable recreation of previous results simulating proton-irradiated T91 from [17] and allow direct comparison with the results in this study. In addition, the respective solute compositions (Table 3.1) and irradiation dose rate were updated to reflect the conditions of our irradiation experiments. Finally, estimation of the equilibrium solute products of both the G-phase (T3) and Γ_2-phase (T6) of T91 were extrapolated from the CALPHAD data provided in [42,43] for our 500 °C

irradiation temperature. After simulation, these values were re-confirmed via comparison between predicted and measured cluster morphologies, which were found to be reasonably consistent.

Table 3.5. Parameters used in cluster dynamics model for T91 irradiated at 500 °C.

Parameter	**Units**	**Neutron irradiation**	**Fe^{2+} irradiation**	**Source(s)**
SIA – Vacancy recombination radius (r_v)	nm	0.57	0.57	[42]
Cascade efficiency (ξ)	-	0.4	0.4	[42]
Displacement per atom cross-section (σ_{dpa})	m^2	1.5×10^{-25}	1.5×10^{-25}	[42]
Atomic volume (Ω_a^3)	m^3	1.18×10^{-29}	1.18×10^{-29}	[42]
Vacancy diffusion pre-exponential (D_v)	m^2/s	1×10^{-4}	1×10^{-4}	[42]
Vacancy migration energy (E_v^m)	eV	1.1	1.1	[42]
Dislocation sink strength (k^2)	m^{-2}	6.25×10^{14}	6.25×10^{14}	[43]
Reference flux (ϕ_r)	$m^{-2}s^{-1}$	3×10^{15}	3×10^{15}	[42]
Flux effect scaling exponential factor (p)	-	0.2	0.5	[42,72]-est
Cascade cross-section (σ_{cas})	m^2	2×10^{-28}	2×10^{-28}	[42]
Reference solute product (K_{sp}^0)	-	2.4×10^{-3}	2.4×10^{-3}	[42]
Heterogeneous nucleation size (n_{het})	-	80	80	[42]
Cascade cluster production efficiency (α)	-	4.8×10^{-3}	4.8×10^{-3}	[42]
Interfacial energy of T3 phase (γ_{T3})	J/m^2	0.185	0.185	[42]
Interfacial energy of T6 phase (γ_{T6})	J/m^2	0.175	0.175	[42]
Flux	particle/m^2s	6.67×10^{17}	5.52×10^{15}	[42]-SRIM
Dose rate (reference)	dpa/s	1.0×10^{-7}	2.23×10^{-4}	Table 2
Diffusivity of Mn in Fe at 500 °C (D_{Mn}^{th})		2.29×10^{-20}	2.29×10^{-20}	[42]
Diffusivity of Ni in Fe at 500 °C (D_{Ni}^{th})	m^2/s	3.45×10^{-21}	3.45×10^{-21}	[42]
Diffusivity of Si in Fe at 500 °C (D_{Si}^{th})	m^2/s	1.76×10^{-20}	1.76×10^{-20}	[42]
Fe self-diffusivity at 500 °C (D_{Fe}^{th})	m^2/s	1.89×10^{-20}	1.89×10^{-20}	[42]
Equilibrium solute product - T3 phase (K_{sp}^{T3})	$\times 10^{-3}$	12.71	12.71	[42,43]-fit
Equilibrium solute product - T6 phase (K_{sp}^{T6})	$\times 10^{-3}$	13.07	13.07	[42,43]-fit

Composition of Si (C_{si})	at%	0.55	0.55	Table 1
Composition of Mn (C_{Mn})	at%	0.45	0.45	Table 1
Composition of Ni (C_{Ni})	at%	0.20	0.20	Table 1
Irradiation temperature	K	773	773	This study

The simulation results in Fig. 3.9 exhibit very reasonable consistency with the APT measured data for cluster size and number density following both irradiations in this study. This helps to confirm our *a priori* estimates for both the cascade efficiency (0.4) and flux effect scaling exponential factor (0.5) for simulating Fe^{2+} irradiation. After simulation, these values also appear to be reasonable considering the relatively close match between simulation and experiment. Notably, the CD simulation predicts larger clusters upon Fe^{2+} irradiation (i.e. higher dose rate) at relatively low dose (Fig. 3.9a). Meanwhile, in Fig. 3.9b, a rapid increase in density is observed beginning at a dose of 0.01 dpa for both irradiation conditions. At ~0.1 dpa (Fe^{2+} irradiation) and ~0.3 dpa (neutron irradiation) the densities rapidly decrease, giving rise to precipitate coarsening.

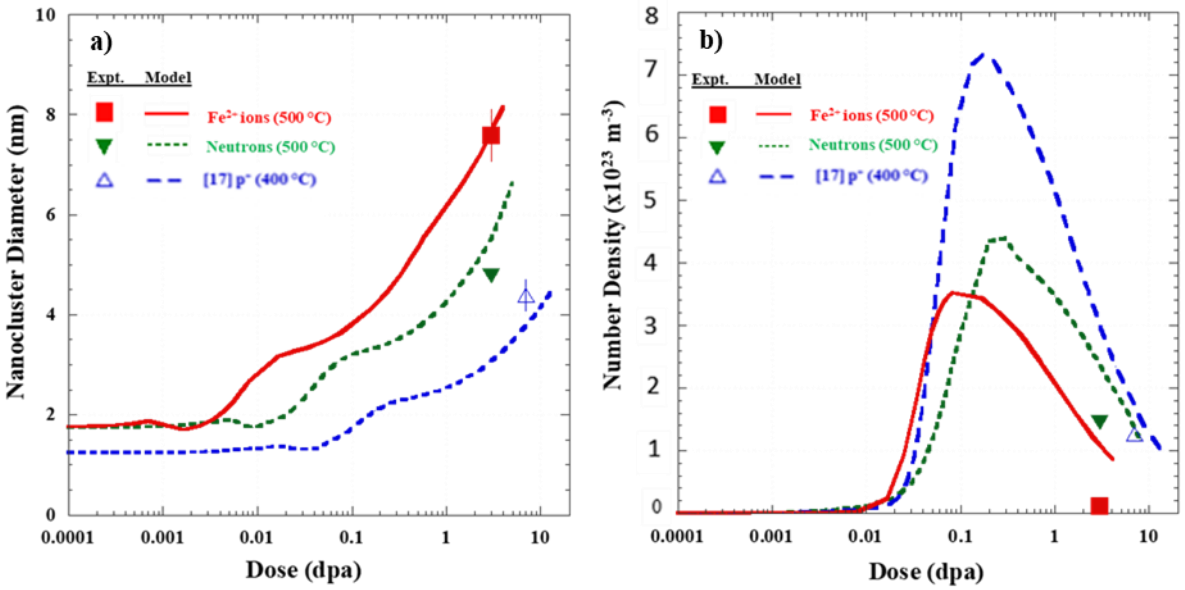

Figure 3.9. Cluster dynamics simulations of Si-Mn-Ni-rich nanocluster evolution in T91 showing a) nanocluster diameter and b) number density as a function of irradiation dose for several different irradiation conditions. Experimentally measured data of Si-Mn-Ni-rich nanoclusters in T91 following each irradiation condition are shown as symbols for comparison.

A complete sensitivity analysis of the cluster dynamics model is conducted to identify the relative influence of each input parameter, *P*, on the output of the model. For this exercise, the predicted size (d_3) of the nanoclusters after 3 dpa is used as the output of the model. Sensitivity analysis highlights those parameters to which d_3 are most sensitive. The sensitivity of the model is defined as the derivative of the output (d_3) as a function of the input parameter ($\frac{\delta d^3}{\delta P}$). The sensitivity is calculated by varying the input parameter close to its reference value and solve for the sensitivity using:

$$\frac{\delta d_3}{\delta P} = \frac{d_3' - d_3^{ref}}{P' - P^{ref}} \quad (7)$$

Where d_3^{ref} is the calculated cluster diameter (at 3 dpa) when the reference input parameter, P^{ref}, is used. Similarly, with P' as the varied parameter, d_3' is the new cluster diameter when P' is entered. The sensitivity is expressed as a significance, giving a more straightforward comparison of the relative influence of each input variable. The significance, S_P^d, is determined by:

$$S_P^d = \frac{d_3' - d_3^{ref}}{P' - P^{ref}} \cdot \frac{P^{ref}}{d_3^{ref}} \quad (8)$$

With this calculation, the model is most sensitive to the parameters having the highest significance.

The significance is calculated for each variable using the model for neutron irradiation of T91 irradiated to a dose of 3 dpa at 500 °C. The predicted cluster size at 3 dpa for neutron irradiation is 5.52 nm (d_3^{ref}). Each variable is altered by values higher than the reference value for the parameter. Using P', the revised output is recorded and the significance for each is calculated and tabulated in Table 3.6 and illustrated in Fig. 3.10. Variables with a positive significance value indicates an increase in the parameter value leads to a increase in the predicted output (i.e. cluster size).

Table 3.6. Significance of varied inputs in the cluster dynamic model for neutron-irradiated

Parameter, P	**Units**	P^{ref}	P'	d_3'**(nm)**	**Significance**
r_v	nm	0.57	0.60	5.52	0.00
ξ	-	0.40	0.42	5.52	0.00
σ_{dpa}	m^2	1.50×10^{-25}	1.52×10^{-25}	5.52	0.00
D_v	m^2/s	1.0×10^{-4}	1.1×10^{-4}	5.50	-0.04
E_v^m	eV	1.1	1.4	5.64	0.08
k^2	m^{-2}	6.25×10^{14}	9.25×10^{14}	5.50	-0.01
ϕ_r	$m^{-2}s^{-1}$	3×10^{15}	3.30×10^{15}	5.50	-0.04
p	-	0.2	0.5	5.31	-0.03
σ_{cas}	m^2	2.0×10^{-28}	2.3×10^{-28}	5.51	-0.01
K_{sp}^0	-	2.4×10^{-3}	2.8×10^{-3}	5.52	0.00
α	-	4.8×10^{-3}	5.1×10^{-3}	5.52	0.00
γ_{T3}	J/m^2	0.185	0.220	5.65	0.12
Flux	Particle/m^2s	6.67×10^{17}	8.00×10^{17}	5.51	-0.01
D_{Mn}^{th}	m^2/s	2.29×10^{-20}	2.52×10^{-20}	5.52	0.00
D_{Ni}^{th}	m^2/s	3.45×10^{-20}	3.80×10^{-20}	5.54	0.04
D_{Si}^{th}	m^2/s	1.76×10^{-20}	1.94×10^{-20}	5.54	0.04
D_{Fe}^{th}	m^2/s	1.89×10^{-20}	2.08×10^{-20}	5.52	-0.02
$\overline{K_{sp}}$	$\times 10^{-3}$	12.71	12.90	5.67	0.27
C_{si}	at%	0.55	0.61	5.20	-0.53
C_{Mn}	at%	0.45	0.50	5.36	-0.26
C_{Ni}	at%	0.2	0.22	4.71	-1.47
T	K	773	783	5.72	2.80

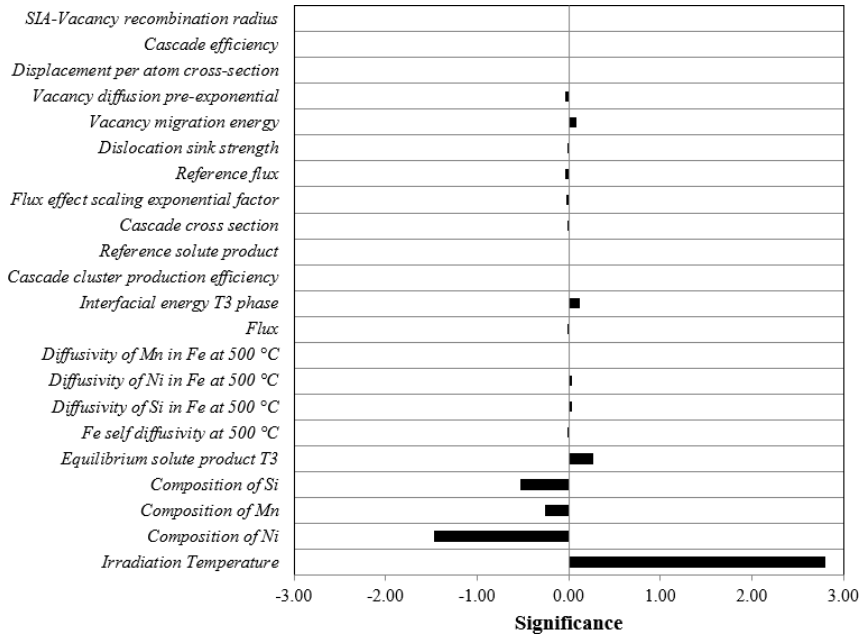

Figure 3.10. Significance of each input parameter in the cluster dynamics model on predicted G-phase nanocluster size for alloy T91 for a reference irradiation with neutrons at 500 °C to 3 dpa.

Interestingly, several of the input parameters for the CD model do not have any influence on the predicted cluster size at 3 dpa, including: the SIA-vacancy recombination radius (r_v), the cascade cross-section (σ_{cas}), the cascade cluster production efficiency (α), and the diffusivity of Manganese. Similarly, the concentration of Ni (C_{Ni}) is also shown to have greater sensitivity than the Si or Mn solutes. This observation appears to be consistent with the work of H. Ke et al. [42], where Ni is also found to be a dominant factor in the formation of Si-Mn-Ni-rich clusters in RPV steels. The fact that nanocluster evolution is mostly driven by a single element may be due to the CD model assumption that the nanoclusters are comprised of the stoichiometric G-phase, suggesting that Ni is the potential limiting reagent

in the formation of these precipitates. We also see that increasing the composition of either Si, Mn, or Ni also leads to reduced coarsening of the nanoclusters.

By far, the predicted cluster size evolution is most sensitive to the irradiation temperature in the cluster dynamics model. Furthermore, the significance of the irradiation temperature is positive, indicating that a higher irradiation temperature will result in larger (and more coarse) cluster morphology at 3 dpa. This predicted behavior is consistent with archival literature results for prior studies in T91 (Fig. 3.1b) and other F/M alloys. As a result, according to the cluster dynamics simulation, a negative temperature shift is likely required for the Fe^{2+} ion irradiation from this study to more accurately emulate the neutron irradiation resulting in a finer nanocluster morphology. While the direction of this shift is contradictory to Mansur's invariance theory, it is consistent with a model developed by Martin [73] to describe nanocluster evolution upon irradiation with different fluxes (or dose rates). Martin proposes that increased irradiation flux causes an increase in the configurational entropy of the system, analogous to a rise in temperature of the system. With this temperature dilation, higher rates of RED are expected, favoring nanocluster growth and coarsening. In the case of this study comparing neutron and heavy ion irradiation, the Fe^{2+} particle flux is not higher than the neutron flux, but the resulting dose rate for heavy ions is several orders of magnitude higher. As a result, the Martin theory suggests that higher dose rate irradiations may need to be conducted at lower temperatures than lower dose rate irradiations to limit solute mobility and attain more consistent nanocluster morphologies. To quantify the predicted temperature shift using the CD simulations, we iteratively evaluated several alternative temperature inputs into the CD model. Alternative temperatures not only affect the irradiation temperature parameter, but also the values for the respective solute

diffusivities and equilibrium solute product parameters in Table 3.5. Using this approach, it is found that an Fe^{2+} ion irradiation temperature of 380 °C is predicted to induce Si-Mn-Ni-rich nanocluster morphologies which are more consistent with those predicted for neutron irradiation at 500 °C (Fig. 3.11). As a follow up to this study, we have initiated a broader Fe^{2+} ion irradiation experiment at this revised temperature on several F/M alloys, with data analysis currently underway and reserved for a future manuscript.

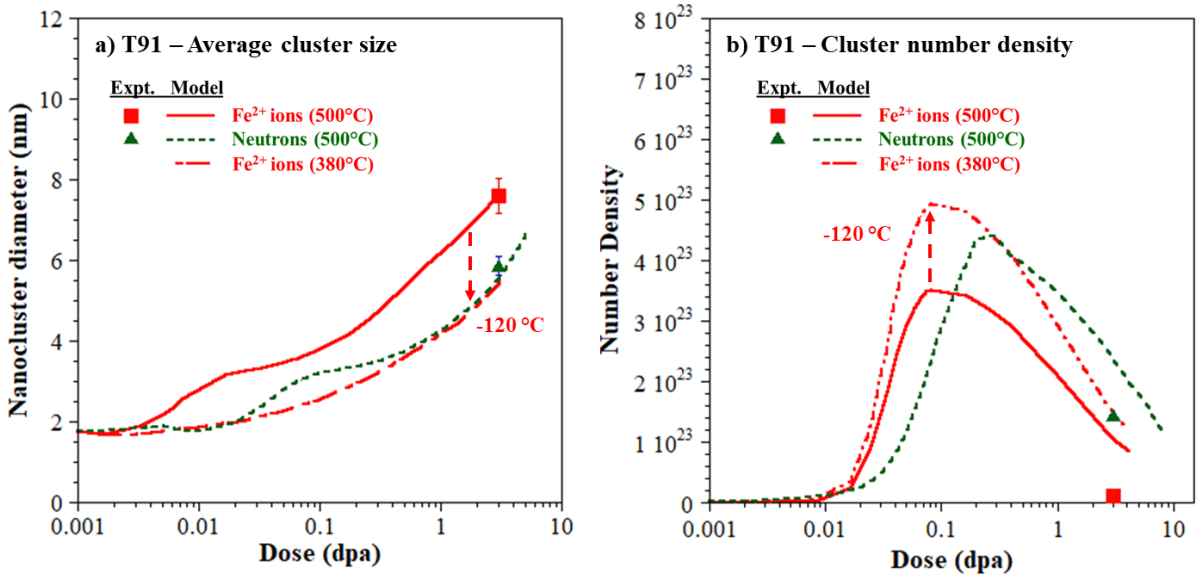

Figure 3.11. Cluster dynamics simulations of Si-Mn-Ni-rich nanocluster evolution in T91 for a) average cluster diameter, and b) cluster number density. The dashed line represents a simulation of Fe2+ irradiation applying a negative temperature shift (-120 °C) to more closely emulate neutron irradiation nanocluster evolution.

It is important to recognize that Martin's temperature dilation theory is developed to describe solute phase evolution upon irradiation, while the Mansur invariance theory is developed in the context of defect clusters (specifically voids). The basis of the invariance theory is to equate the concentration of vacancies within the microstructure, enabling the

formation of defect clusters to be comparable despite differences in irradiation dose rate. With higher dose rates producing a higher density of defects (in a shorter period of time), this effect must be offset by increasing the irradiation temperature. The higher temperature increases defect mobility, resulting in more trapping and annihilation at sinks in the microstructure and balancing the increase in defect production rate. As a result, the invariance theory (which predicts a positive temperature shift of +50-60 °C) likely still applies for defect clusters including dislocation loops and voids. In fact, Taller, et al. [32] already conducted a systematic study on T91 using a range of positive temperature shifts and found good agreement in dislocation loop morphologies and cavity size distribution using a temperature shift of ~+60-70 °C. Unfortunately, they did not observe the same match in nanocluster morphology, supporting the notion for needing feature-specific temperature shifts.

Literature Cited

[1] P. Yvon, F. Carré, Structural materials challenges for advanced reactor systems, J. Nucl. Mater. 385 (2009) 217–222. doi:10.1016/j.jnucmat.2008.11.026.

[2] T. Allen, J. Busby, M. Meyer, D. Petti, Materials challenges for nuclear systems, Mater. Today. 13 (2010) 14–23. doi:10.1016/S1369-7021(10)70220-0.

[3] S.J. Zinkle, J.T. Busby, Structural materials for fission & fusion energy, Mater. Today. 12 (2009) 12–19. doi:10.1016/S1369-7021(09)70294-9.

[4] C. Pareige, V. Kuksenko, P. Pareige, Behaviour of P, Si, Ni impurities and Cr in self ion irradiated Fe-Cr alloys - Comparison to neutron irradiation, J. Nucl. Mater. 456 (2015) 471–476. doi:10.1016/j.jnucmat.2014.10.024.

[5] M. Bachhav, G. Robert Odette, E.A. Marquis, α′ precipitation in neutron-irradiated Fe-Cr alloys, Scr. Mater. 74 (2014) 48–51. doi:10.1016/j.scriptamat.2013.10.001.

[6] M.J. Swenson, J.P. Wharry, Nanocluster irradiation evolution in Fe-9%Cr ODS and ferritic-martensitic alloys, J. Nucl. Mater. 496 (2017) 24–40. doi:10.1016/j.jnucmat.2017.08.045.

[7] B.H. Sencer, J.R. Kennedy, J.I. Cole, S.A. Maloy, F.A. Garner, Microstructural analysis of an HT9 fuel assembly duct irradiated in FFTF to 155 dpa at 443 ° C, J. Nucl. Mater. 393 (2009) 235–241. doi:10.1016/j.jnucmat.2009.06.010.

[8] F. Christien, A. Barbu, Modelling of copper precipitation in iron during thermal aging and irradiation, Journals Nucl. Mater. 324 (2004) 90–96. doi:10.1016/j.jnucmat.2003.08.035

[9] E. Getto, Z. Jiao, A.M. Monterrosa, K. Sun, G.S. Was, Effect of irradiation mode on the microstructure of self-ion irradiated ferritic-martensitic alloys, J. Nucl. Mater. 465 (2015) 116–126. doi:10.1016/j.jnucmat.2015.05.016.

[10] D.G. Park, C.G. Kim, H.C. Kim, J.H. Hong, I.S. Kim, Effect of neutron irradiation on magnetic properties in the low alloy Ni-Mo steel SA508-3, J. Appl. Phys. 81 (1997) 4125–4127. doi:10.1063/1.365101.

[11] E.M. Francis, A. Harte, P. Frankel, S.J. Haigh, D. Jädernäs, J. Romero, L. Hallstadius, M. Preuss, Iron redistribution in a zirconium alloy after neutron and proton irradiation studied by energy-dispersive X-ray spectroscopy (EDX) using an aberration-corrected (scanning) transmission electron microscope, J. Nucl. Mater. 454 (2014) 387–397. doi:10.1016/j.jnucmat.2014.08.034.

[12] X. Liu, Y. Miao, M. Li, M.K. Kirk, S.A. Maloy, J.F. Stubbins, Ion-irradiation-induced microstructural modifications in ferritic/martensitic steel T91, J. Nucl. Mater. 490 (2017) 305–316. doi:10.1016/j.jnucmat.2017.04.047.

[13] R. Schaeublin, T. Leguey, P. Spätig, N. Baluc, M. Victoria, Microstructure and mechanical properties of two ODS ferritic/martensitic steels, J. Nucl. Mater. 307–311 (2002) 778–782. doi:10.1016/S0022-3115(02)01193-5.

[14] M. Matijasevic, Behaviour of Fe-Cr based alloys under neutron irradiation, Ames. (2007) 1–6. http://scindeks.nb.rs/article.aspx?artid=0354-63060704245M.

[15] P. Ampornrat, G.S. Was, Oxidation of ferritic-martensitic alloys T91, HCM12A and HT-9 in supercritical water, J. Nucl. Mater. 371 (2007) 1–17. doi:10.1016/j.jnucmat.2007.05.023.

[16] E.R. Reese, M. Bachhav, P. Wells, T. Yamamoto, G.R. Odette, E.A. Marquis, On α′

precipitate composition in thermally annealed and neutron-irradiated Fe- 9-18Cr alloys, J. Nucl. Mater. 500 (2018) 192–198. doi:10.1016/j.jnucmat.2017.12.036.

[17] Z. Jiao, V. Shankar, G.S. Was, Phase stability in proton and heavy ion irradiated ferritic-martensitic alloys, J. Nucl. Mater. 419 (2011) 52–62. doi:10.1016/j.jnucmat.2011.08.020.

[18] J.P. Wharry, Z. Jiao, V. Shankar, J.T. Busby, G.S. Was, Radiation-induced segregation and phase stability in ferritic-martensitic alloy T 91, J. Nucl. Mater. 417 (2011) 140–144. doi:10.1016/j.jnucmat.2010.12.052.

[19] J.W.P. Schmelzer, A.S. Abyzov, J. Moller, Nucleation versus spinodal decomposition in phase formation processes in multicomponent solutions, J. Chem. Phys. 6900 (2004). doi:10.1063/1.1786914.

[20] G.R. Odette, G.E. Lucas, Embrittlement of Nuclear Reactor Pressure Vessels, J. Miner. Met. Mater. Soc. (2001) 18–22. doi:10.1007/s11837-001-0081-0.

[21] K. Fukuya, Current understanding of radiation-induced degradation in light water reactor structural materials, J. Nucl. Sci. Technol. 3131 (2013). doi:10.1080/00223131.2013.772448.

[22] J.E. Zelenty, Understanding thermally induced embrittlement in low copper RPV steels utilising atom probe tomography, Mater. Sci. Technol. (2016). doi:10.1179/1743284714Y.0000000718.

[23] M.J. Swenson, J.P. Wharry, The comparison of microstructure and nanocluster evolution in proton and neutron irradiated Fe-9%Cr ODS steel to 3 dpa at 500 °C, J. Nucl. Mater. 467 (2015) 97–112. doi:10.1016/j.jnucmat.2015.09.022.

[24] A.M. Monterrosa, Z. Jiao, G.S. Was, The influence of helium on cavity evolution in ion-irradiated T91, J. Nucl. Mater. 509 (2018) 707–721. doi:10.1016/j.jnucmat.2018.06.033.

[25] Z. Jiao, J. Michalicka, G.S. Was, Self-ion emulation of high dose neutron irradiated microstructure in stainless steels, J. Nucl. Mater. 501 (2018) 312–318. doi:10.1016/j.jnucmat.2018.01.054.

[26] R. Rayaprolu, S. Möller, C. Linsmeier, S. Spellerberg, Simulation of neutron irradiation damage in tungsten using higher energy protons, Nucl. Mater. Energy. 9 (2016) 29–35. doi:10.1016/j.nme.2016.09.008.

[27] G.S. Was, J.T. Busby, T. Allen, E.A. Kenik, A. Jenssen, S.M. Bruemmer, J. Gan, A.D. Edwards, P.M. Scott, P.L. Andresen, Emulation of neutron irradiation effects with protons : validation of principle, J. Nucl. Mater. 300 (2002) 198–216. doi:10.1016/S0022-3115(01)00751-6.

[28] Z. Jiao, G.S. Was, Precipitate evolution in ion-irradiated HCM12A, J. Nucl. Mater. (2012) 105–111. doi:10.1016/j.jnucmat.2011.12.017.

[29] G.S. Was, Z. Jiao, E. Getto, K. Sun, A.M. Monterrosa, S.A. Maloy, O. Anderoglu, B.H. Sencer, M. Hackett, Emulation of reactor irradiation damage using ion beams, Scr. Mater. 88 (2014) 33–36. doi:10.1016/j.scriptamat.2014.06.003.

[30] L.K. Mansur, Correlation of Neutron and Heavy-Ion Damage, J. Nucl. Mater. 78 (1978) 156–160. doi:10.1016/S0022-3115(01)00751-6.

[31] L.K. Mansur, Theory of transitions in dose dependence of radiation effects in structural alloys, J. Nucl. Mater. 206 (1993) 306–323. doi:10.1016/0022-3115(93)90130-Q.

[32] S. Taller, Z. Jiao, K. Field, G.S. Was, Emulation of fast reactor irradiated T91 using dual ion beam irradiation, J. Nucl. Mater. (2019) 151831. doi:10.1016/j.jnucmat.2019.151831.

[33] Z. Jiao, S. Taller, K. Field, G. Yeli, M.P. Moody, G.S. Was, Microstructure evolution of T91 irradiated in the BOR60 fast reactor, J. Nucl. Mater. 504 (2018) 122–134. doi:10.1016/j.jnucmat.2018.03.024.

[34] E. Getto, K. Sun, A.M. Monterrosa, Z. Jiao, M.J. Hackett, G.S. Was, Void swelling and microstructure evolution at very high damage level in self-ion irradiated ferritic-martensitic steels, J. Nucl. Mater. 480 (2016) 159–176. doi:10.1016/j.jnucmat.2016.08.015.

[35] O. Anderoglu, J. Van Den Bosch, P. Hosemann, E. Stergar, B.H. Sencer, D. Bhattacharyya, Phase stability of an HT-9 duct irradiated in FFTF, J. Nucl. Mater. 430 (2012) 194–204. doi:10.1016/j.jnucmat.2012.06.038.

[36] B.H. Sencer, J.R. Kennedy, J.I. Cole, S.A. Maloy, F.A. Garner, Microstructural stability of an HT-9 fuel assembly duct irradiated in FFTF, J. Nucl. Mater. 414 (2011) 237–242. doi:10.1016/j.jnucmat.2011.03.050.

[37] C. Zheng, E.R. Reese, K.G. Field, E. Marquis, S.A. Maloy, D. Kaoumi, Microstructure response of ferritic / martensitic steel HT9 after neutron irradiation : effect of dose, J. Nucl. Mater. 523 (2019) 421–433. doi:10.1016/j.jnucmat.2019.06.019.

[38] C. Zheng, E.R. Reese, K.G. Field, E. Marquis, S.A. Maloy, D. Kaoumi, Microstructure response of ferritic/martensitic steel HT9 after neutron irradiation: Effect of temperature, J. Nucl. Mater. (2019) 151845. doi:10.1016/j.jnucmat.2019.151845.

[39] S. Shu, P.B. Wells, N. Almirall, G.R. Odette, D.D. Morgan, Thermodynamics and kinetics of core-shell versus appendage co-precipitation morphologies: An example in the Fe-Cu-Mn-Ni-Si system, Acta Mater. 157 (2018) 298–306. doi:10.1016/j.actamat.2018.07.037.

[40] G.R. Odette., Radiation Induced Microstructural Evolution In Reactor Pressure Vessel Steels. In: Robertson IM, Rehn LE, Zinkle SJ, Phythian WJ, (Eds.). Materials Research Society Symposium Proceedings, vol. 373. Warrendale: Materials Research Society, 1995. p.137-148., 373 (1995) 137–148. doi:10.1557/PROC-373-137.

[41] C.L. Liu, G.R. Odette, B.D. Wirth, G.E. Lucas, A lattice Monte Carlo structures in irradiated simulation pressure of nanophase compositions and vessel Fe-Cu-Ni-Mn-Si steels, Mater. Sci. Eng. A. 238 (1997). doi:10.1016/S0921-5093(97)00450-4.

[42] H. Ke, P. Wells, P.D. Edmondson, N. Almirall, L. Barnard, G.R. Odette, D. Morgan, Thermodynamic and kinetic modeling of Mn-Ni-Si precipitates in low-Cu reactor pressure vessel steels, Acta Mater. 138 (2017) 1–51. doi:10.1016/j.actamat.2017.07.021.

[43] J.H. Ke, H. Ke, G.R. Odette, D. Morgan, Cluster dynamics modeling of Mn-Ni-Si precipitates in ferritic-martensitic steel under irradiation, J. Nucl. Mater. 498 (2018) 83–88. doi:10.1016/j.jnucmat.2017.10.008.

[44] L.T. Belkacemi, E. Meslin, B. Décamps, B. Radiguet, J. Henry, Radiation-induced bcc-fcc phase transformation in a Fe–3%Ni alloy, Acta Mater. 161 (2018) 61–72. doi:10.1016/j.actamat.2018.08.031.

[45] R. Ngayam-Happy, C.S. Becquart, C. Domain, L. Malerba, Formation and evolution of MnNi clusters in neutron irradiated dilute Fe alloys modelled by a first principle-

based AKMC method, J. Nucl. Mater. 426 (2012) 198–207. doi:10.1016/j.jnucmat.2012.03.033.

[46] G. Bonny, D. Terentyev, A. Bakaev, E.E. Zhurkin, M. Hou, D. Van Neck, L. Malerba, On the thermal stability of late blooming phases in reactor pressure vessel steels: An atomistic study, J. Nucl. Mater. 442 (2013) 282–291. doi:10.1016/j.jnucmat.2013.08.018.

[47] E. Meslin, B. Radiguet, P. Pareige, C. Toffolon, A. Barbu, Irradiation-Induced Solute Clustering in a Low Nickel FeMnNi Ferritic Alloy, Exp. Mech. 51 (2011) 1453–1458. doi:10.1007/s11340-011-9476-1.

[48] N. Almirall, P.B. Wells, H. Ke, P. Edmondson, D. Morgan, T. Yamamoto, G.R. Odette, On the elevated temperature thermal stability of nanoscale Mn-Ni-Si precipitates formed at lower temperature in highly irradiated reactor pressure vessel steels, Sci. Rep. 9 (2019) 1–12. doi:10.1038/s41598-019-45944-z.

[49] W. Xiong, H. Ke, R. Krishnamurthy, P. Wells, L. Barnard, G.R. Odette, D. Morgan, Thermodynamic models of low-temperature Mn–Ni–Si precipitation in reactor pressure vessel steels, MRS Commun. 4 (2014) 101–105. doi:10.1557/mrc.2014.21.

[50] H.J. MacLean, K. Sridharan, T.A. Hyde, Irradiation Test Plan for the ATR National Scientific User Facility - University of Wisconsin Pilot Project, (2008) 1–18.

[51] J.F. Ziegler, M.D. Ziegler, J.P. Biersack, SRIM – The stopping and range of ions in matter (2010), Nucl. Inst. Methods Phys. Res. B. 268 (2010) 1818–1823. doi:10.1016/j.nimb.2010.02.091.

[52] M.J. Swenson, J.P. Wharry, TEM characterization of irradiated microstructure of Fe-9 % Cr ODS and ferritic-martensitic alloys, J. Nucl. Mater. 502 (2018) 30–41. doi:10.1016/j.jnucmat.2018.01.062.

[53] C.M. Parish, K.G. Field, Application of STEM characterization for investigating radiation effects in BCC Fe-based alloys, J. Mater. Res. (2015) 1–15. doi:10.1557/jmr.2015.32.

[54] B. Yao, D.J. Edwards, R.J. Kurtz, TEM characterization of dislocation loops in irradiated bcc Fe-based steels, J. Nucl. Mater. 434 (2013) 402–410. doi:10.1016/j.jnucmat.2012.12.002.

[55] S. Lozano-Perez, Characterization techniques for assessing irradiated and ageing materials in nuclear power plant systems, structures and components (SSC), in: Underst. Mitigating Ageing Nucl. Power Plants, 2010. doi:10.1533/9781845699956.3.389.

[56] K. Thompson, D. Lawrence, D.J. Larson, J.D. Olson, T.F. Kelly, B. Gorman, In situ site-specific specimen preparation for atom probe tomography, Ultramicroscopy. 107 (2007) 131–139. doi:10.1016/j.ultramic.2006.06.008.

[57] J.M. Hyde, E.A. Marquis, K.B. Wilford, T.J. Williams, A sensitivity analysis of the maximum separation method for the characterisation of solute clusters, Ultramicroscopy. 111 (2011) 440–447. doi:10.1016/j.ultramic.2010.12.015.

[58] R.P. Kolli, D.N. Seidman, Comparison of Compositional and Morphological Atom-Probe Tomography Analysis for a Multicomponent Fe-Cu Steel, Microsc. Microanal. (2007). doi:10.1017/S1431927607070675.

[59] C.A. Williams, D. Haley, E.A. Marquis, G.D.W. Smith, M.P. Moody, Defining clusters in APT reconstructions of ODS steels, Ultramicroscopy. 132 (2013) 271–278. doi:10.1016/j.ultramic.2012.12.011.

[60] M.K. Miller, R. Forbes, Atom Probe Tomography: The Local Electrode Atom Probe, Springer, New York, 2014.

[61] C.A. Williams, E.A. Marquis, G.D.W.S. A. Cerezo, Nanoscale characterisation of ODS- Eurofer 97 steel: An atom-probe tomography study, J. Nucl. Mater. (2010) 37–45. doi:10.1016/j.jnucmat.2010.02.007.

[62] A.D. Whapham, M.J. Makin, The Hardening of Lithium Fluoride by Electron Irradiation, Met. Div. At. Energy Res. Establ. Harwell. (1959). doi:10.1080/14786436008235839.

[63] T. Allen, K. Djamel, J.P. Wharry, Z. Jiao, Characterization of microstructure and property evolution in advanced cladding and duct: Materials exposed to high dose and elevated temperature, J. Mater. Res. (2015). doi:10.1557/jmr.2015.99.

[64] C. Topbasi, D. Kaoumi, A.T. Motta, M.A. Kirk, Microstructural evolution in NF616 (P92) and Fe - 9Cr- 0.1C-model alloy under heavy ion irradiation, J. Nucl. Mater. 466 (2015) 179–186. doi:10.1016/j.jnucmat.2015.07.003.

[65] R. Schaublin, A. Ramar, N. Baluc, V. de Castro, M.A. Monge, T. Leguey, N. Schmid, C. Bonjour, Microstructural development under irradiation in European ODS ferritic / martensitic steels, Journals Nucl. Mater. 351 (2006) 247–260. doi:10.1016/j.jnucmat.2006.02.005.

[66] S.L. Dudarev, R. Bullough, P.M. Derlet, Effect of the α - γ Phase Transition on the Stability of Dislocation Loops in bcc Iron, 135503 (2008) 1–4. doi:10.1103/PhysRevLett.100.135503.

[67] J.P. Wharry, G.S. Was, The mechanism of radiation-induced segregation in ferritic-martensitic alloys, Acta Mater. 65 (2014) 42–55. doi:10.1016/j.actamat.2013.09.049.

[68] L. Messina, M. Nastar, N. Sandberg, Systematic electronic-structure investigation of substitutional impurity diffusion and flux coupling in bcc iron, 184302 (2016) 1–18. doi:10.1103/PhysRevB.93.184302.

[69] L. Messina, M. Chiapetto, P. Olsson, C.S. Becquart, L. Malerba, An object kinetic Monte Carlo model for the microstructure evolution of neutron-irradiated reactor pressure vessel steels, Phys. Status Solidi Appl. Mater. Sci. 213 (2016). doi:https://doi.org/10.1002/pssa.201600038.

[70] V.V. Slezov, Kinetics of first order phase transitions, Wiley-VCH, Weinheim, 2009.

[71] G.S. Was, Fundamentals of Radiation Materials Science, Springer, New York, 2007.

[72] E.D. Eason, C. Services, G.R. Odette, S. Barbara, R.K. Nanstad, O. Ridge, T. Yamamoto, S. Barbara, A Physically Based Correlation of Irradiation-Induced Transition Temperature Shifts for RPV Steels, J. Nucl. Mater. 433 (2013) 240–254. doi:10.1016/j.jnucmat.2012.09.012.

[73] G. Martin, Phase stability under irradiation: Ballistic effects, Phys. Rev. B. 30 (1984) 1424–1436. doi:10.1103/PhysRevB.30.1424.

Chapter 4: Temperature shift evaluation of nanoclusters evolution in ferritic-martensitic alloys

Abstract

The objective of this research is to evaluate the temperature shift requirement for ion irradiation to emulate neutron irradiation damage in three ferritic-martensitic alloys. Historically, the invariance theory has been the basis of choosing conditions for ion irradiation to emulate neutron irradiation damage for defect clusters. However, it is unclear if the same theory applies to solute clustering. A systematic characterization of Si-Mn-Ni rich and Cu rich nanoclusters have been conducted in T91, HCM12A, and HT9 using atom probe tomography after neutron or Fe^{2+} to 3 dpa at 500 °C. Two distinct models have been employed to simulate the prescribed temperature shift requirement and they both predicted that a negative temperature shift will be needed for Fe^{2+} ion to emulate Si-Mn-Ni rich nanocluster evolution resulting from neutron irradiation at 500 °C. APT analysis reveals that the size and number density of nanoclusters following Fe^{2+} irradiation at the prescribed temperature shift is comparable to the nanocluster morphology following neutron irradiation at 500 °C, thus validating the negative temperature shift prescription.

Introduction

The development of structural and cladding materials for Generation IV reactors requires materials that will be able to withstand reactors intense neutron fluxes, high operation temperature up to 700 °C, and contact with highly corrosive coolant such as molten salt [1]. Ferritic-Martensitic (F/M) alloys are seen as a leading candidates materials to meet

the reactors high- dose requirement due to their excellent swelling resistance, low ductile to brittle transformation temperature and high thermal conductivity [2,3,12,4–11]. In order to predict the behavior of these alloys after long term irradiation, it is important to understand the role of individual alloying elements on the evolution of microstructures under irradiation. Investigation have shown that the nucleation and growth of α', Si-Mn-Ni rich, and Cu rich nanoclusters in irradiated F/M alloys are capable of altering the mechanical properties of the F/M alloys. The formation of high number density of these irradiation induced solute clusters may lead to significant hardening or embrittlement which may limit the performance of materials of most nuclear reactors [11–16].

The evolution of Si-Mn-Ni clusters is potentially made kinetically possible by the high flux of point defects and the formation of point defect clusters under irradiation [17–19]. Irradiation temperature and dose have been reported to have a pronounce effect on the microstructure evolution in these alloys and the general trend is that the average size increases with increasing temperature and dose[11,20,21] . Zheng et al. [22] observed the formation of Si-Mn-Ni rich clusters in HT9 under self-irradiation to 20 dpa at 440 – 470 °C, the size of Si-Mn-Ni rich nanoclusters increases from 11.6 ± 2.8 nm to 16.54 nm as the temperature increases from 440 – 470 °C while the number density decreases from 10.68 x 10^{20} m^{-3} to 8.26 x 10^{20} m^{-3}. A similar trend was observed following neutron irradiation of HT9 to a dose ranging ~17.1 to 35.1 dpa at a temperature of 650K, the size of the Si-Mn-Ni nanoclusters increases from 6.1 nm to 7.2 nm as the dose increase, while the number density decreases from 4.3 x 10^{22} m^{-3} to 3.3 x 10^{22} m^{-3} [21]. In addition, Jiao et al. [11] also observed the nucleation and growth of Si-Mn-Ni and Cu-rich nanoclusters following proton irradiation of T91, HT9, and HCM 12A to a dose of 7 – 100 dpa at a temperature range of 400 -500 °C,

with Si-Mn-Ni rich cluster size increases from 4.4 nm to 6.6 nm as the temperature increases from 400 to 500 °C, while the number density decreases (2.69 - 0.08 x $10^{23}m^{-3}$). Similar trend was reported for Cu-rich nanoclusters at the same temperature sequence and it is generally believed that Cu-rich nanocluster are formed due to the very low Cu solubility in Fe matrix.

Cr-rich (α') phase are formed by the spinodal decomposition during thermal ageing especially in alloys with high Cr F/M alloys (>9 at%). High number density of α' phase has been reported to nucleate in HT9 and HCM 12A and its size and number density are found to be dependent on the alloy Cr content, irradiation dose and temperature just like the Si-Mn-Ni and Cu rich nanoclusters. Zheng, et al [21], observed the evolution of chromium rich α' phase after irradiation in BOR60 reactor at a temperature of 377 °, the size of α' precipitates is found to increase from 6.5 nm 7.2 nm as the dose increases from 17 to 35 dpa. Following similar irradiation on HT9 to a dose of 20 dpa, the size of the α' precipitates is also found to increase (6.5 – 10.4 nm) as the temperature is increased from 650 to 730 K [20]. Swenson, et al. [23] as well reported high number density of α' precipitates after neutron irradiation of HT9 and HCM12A to 3 dpa at 500 °C. However, these precipitates do not nucleate in these alloys after proton or Fe^{2+} irradiation which suggest that the precipitation of α' phase is time dependent. Additional study by Bachhav et al [24], reported nucleation of α' precipitates in a model Fe-Cr alloy containing 3 -18 at% Cr after neutron irradiation to 1.82 dpa at 563K. Finely dispersed α' precipitates was observed in alloys containing more than 9 at% Cr, the number density of these precipitates increases with increasing Cr content while the size decreases. Therefore, Bachhav suggested that the precipitation of α' precipitates requires Cr bulk concentration of more than 9 at%.

The evolution of irradiation induced microstructure in F/M alloys must be fully understood in order develop a more reliable materials that will be able to perform at high dose and temperatures. A lot of neutron and ion irradiation experiments have been conducted for years in order to gain detailed understanding of nanocluster evolution under irradiation, but there has been a challenge to compare studies that are conducted under different irradiation conditions, especially those using different types of irradiation particles. Charge particles irradiation can reach hundreds of dpa in a very short time saving the extremely high cost of irradiation and post-irradiation characterization as compared to neutron irradiation experiment. Charge particles irradiation are commonly used to emulate neutron irradiation effect in candidate materials. However, both irradiations differ by dose rate and damage cascade morphologies, and there is limited understanding of how these physical differences will manifest in the resultant microstructure or the mechanical properties of the target alloys. Till date, there is a knowledge gap on how to set irradiation conditions for charge particles irradiation to appropriately emulate neutron irradiation.

Historically, the invariance theory originally proposed by Mansur [25] has been the basis for selecting conditions for ion irradiation to emulate neutron irradiation. This theory predicts that a temperature adjustment will be needed for ion irradiation to produce equivalent defect clusters. However, some studies using modern computational techniques [26,27] support the invariance theory but also acknowledge that the development of irradiation damage cascade is critical to the accumulation of local defects and defect cluster morphologies, but the invariance theory did not take this into consideration. Most studies are comparing ion and neutron irradiations at similar conditions [11,23,28], at random conditions [11,29–32], or at conditions prescribed by the Mansur invariance theory [33]. But, the

Mansur theory is primarily focused on match defect cluster (voids & loops) morphologies. Recently, Swenson et al. [34] conducted irradiation on HCM 12A and HT9 to a dose of ~3 dpa using variable dose rate (neutrons (~10^{-7} dpa/s, protons (1.2 x 10^{-5} dpa/s, and Fe^{2+} ions (2.2 x 10^{-4} dpa/s). The evolution of dislocation loops and voids in the these alloys was statistically invariant between each irradiation, supporting the Mansur's theory where only a small temperature shift (in the recombination dominated regime) is required for a higher dose rate irradiation to emulate lower dose rate irradiation.

Meanwhile, several more advanced calculation models have been developed over the past few years, which attempt to model nanocluster evolution in F/M alloys. For example, the NHM model developed by Nelson, Hudson, and Mazey [35], a first order differential equations describing the change in cluster radius over time depending on the dominant dissolution mechanism between recoil dissolution and disordering dissolution. The NHM model focus on the diffusion of solutes through defects, suggesting growth and coarsening of nanoclusters (via radiation enhanced diffusion). Another model developed by Wagner [36] has been advanced by Chen et al [37] to simulate the evolution of nanoclusters in ODS alloy. The difference between this model and the NHM model is that it incorporates the effect of Gibb-Thompson and the contribution of interfacial energy between the clusters and the matrix on the growth and coarsening of nanoclusters. Cheng et al. validates the model with their experimental result which shows that coherent clusters experience little change in size, while incoherent clusters readily dissolves at lower temperature.

One of the more successful models is the cluster dynamic (CD) model developed by Ke et al [38] to simulate nucleation and growth of Si-Mn-Ni rich nanoclusters in low Cu RPV and in F/M alloy T91 [39]. The advantage of the CD model over other models is that it

has the capacity to predict both the cluster size and the number density. Adisa et al. [28] further advanced the CD model to confirm its sensitivity to temperature following neutron irradiation of T91 to 3 dpa at 500 °C, the sensitivity analysis reveals increasing cluster size with decreasing number density as the temperature increases.

Prior studies of F/M alloys T91, HCM12A, and HT9 have shown variable nanocluster evolution of Si-Mn-Ni-rich, Cu-rich, and Cr-rich nanocluster evolution following irradiation with protons, Fe^{2+} ions, or neutron irradiation to a common dose of ~ 3 dpa at 500 °C [23,28]. Therefore, the objective of this work is to evaluate the temperature shift requirements for Fe^{2+} ion irradiation to emulate solute nanoclusters evolution observed following neutron irradiation to 3 dpa at 500 °C. The irradiation condition for Fe^{2+} ions to emulate neutrons are established through temperature sensitivity analysis using both the CD and NHM models. Solute clusters are characterized at the prescribed temperature shift to evaluate the efficacy of the models. To date, authors are not aware of any prior study which uses one of the advanced models to specifically predict a temperature shift, and then conducted an irradiation experiment to directly evaluate the prediction.

Methods and Materials

Materials

This work focuses on three alloys, T91, HCM12A, and HT9. Alloy T91, nominally 9Cr-MoVNb, exhibit a martensitic structure with small laths on the order of ~0.4 μm wide and 0.8 μm long and dislocation densities of ~10^{15} m^{-2}. The final heat treatment involves austenitizing at 1040 °C for 1 hour followed by air cooling and then tempered at 760 °C for

60 min. Alloy HT9, nominally 12Cr-MoVW, exhibits a three-phase microstructure δ-ferrite, retained austenite and martensitic laths of 0.4 µm wide and 14.6 µm long. The alloy was austenitized at 1040 °C for 30 min followed by air cooling, tempered at 760 °C for 60 min and finally air cooled. Alloy HCM12A, nominally 12Cr-MoVNbWCu was austenitized at 1050 °C for 1 hour followed by air cooling, and then tempered at 770 °C for 45 min and finally air cooled. It exhibits two phase microstructures comprising of δ-ferrite and martensitic laths, both are 0.9 µm wide and 6.1 µm long. Complete chemical composition of the three alloys are provided in Table 4.1.

Table 4.1. Chemical composition of T91, HCM12A and HT9

Element	T91	HCM 12A	HT9
Cr	8.37	10.83	11.63
Mo	0.9	0.3	1
Mn	0.45	0.64	0.52
Ni	0.21	0.39	0.5
V	0.22	0.19	0.3
Cu	0.17	1.02	0.04
W	-	1.89	0.52
Si	0.28	0.27	0.22
Nb	0.08	0.054	-
C	0.1	0.11	0.2
N	0.05	0.063	0.047
Al	0.02	0.001	<0.01
P	0.01	0.016	0.02
S	0.003	0.002	0.006
Ti	-	-	0.002
Fe	Bal.	Bal.	Bal.

Modeling

It has been hypothesized that the evolution of solute nanocluster in F/M alloys is based on the conflicting effect of ballistic dissolution and radiation enhanced diffusion via Oswald ripening. Based on this hypothesis two distinct models (NHM and CD) was advanced to predict nanocluster evolution in T91, HCM12A, and HT9. The CD model includes embedded routines for determining radiation-enhanced diffusion (RED) and thermodynamic heterogeneous nucleation. Below are the cluster dynamic master equations employed in this study.

$$\frac{\partial f}{\partial t} = R_{het}(n,t) + J_{n-1\rightarrow n} - J_{n\rightarrow n+1} \quad (1)$$

$$J_{n\rightarrow n+1} = \omega^{+}_{n,n+1} f(n.t) - \omega^{-}_{n+1,n} f(n+1,t) \quad (2)$$

which describe the evolution of the size distribution and mole fraction (*f*) of Si-Mn-Ni rich phase as a function of fluence, temperature, and alloy composition. The co-efficient $\omega^{+}_{n,n+1}$ is the rate at which clusters of size *n* absorb single atoms to grow to size *n+1*, while the co-efficient $\omega^{-}_{n+1,n}$ is the rate at which clusters of size *n+1* emit single particles to shrink to size *n*. In this model, it is assumed that clusters grow and shrink by the absorption and emission of pseudo-monomer molecules consisting of Si, Mn, and Ni. The underlying mechanism is that the generation of a high concentration of point defects in the cascades leads to the formation of defect-solute cluster complexes as a result of defect-solute binding energies and local radiation-induced segregation (RIS) [38,39]. In Ref [28], we modified the parameters of the existing cluster dynamic (CD) model that have been successfully used to describe nucleation and growth of Si-Mn-Ni rich nanoclusters in RPV and T91 [38,39] to reflect our irradiation conditions (Fe^{2+} or neutron irradiation to 3 dpa at 500 °C). The CD model

reasonably simulates the nanocluster evolution up to 3 dpa (Fig. 3.9a and b), predicting larger nanoclusters with self-ion irradiation at a higher dose rate. Sensitivity analysis was carried out on cluster dynamic model following neutron irradiation of T91 at 500 °C to understand the response of the model to each of its input parameters, and we found out that alloy concentration especially Ni and irradiation temperature have the most significant influence on the cluster size. However, having understand that the model is sensitive to alloy composition and temperature, it is worthwhile to see if CD model will be effective in simulating the nucleation and growth of Si-Mn-Ni rich clusters in other b.c.c Fe based alloy and also predict the required temperature shift for ion irradiation to emulate neutron irradiation damage. Therefore, we carried out cluster dynamic simulation for HCM12A to predict the nucleation and growth of Si-Mn-Ni rich nanoclusters following Fe^{2+} ions or neutrons irradiation to 3dpa at 500 °C. From the existing CD model in [28], we modified the parameters that are specific to HCM12A such as the composition of Si, Mn, and Ni as well as the sink strength. A summary of the parameters used for the CD model set up for T91 and HCM12A are presented in Table 4.2 and Table 4.3.

Table 4.2. Parameters used in cluster dynamics (CD) calculation for T91 at 370 °C

Parameter	**Units**	**Fe^{2+} irradiation**	**Source(s)**
SIA – Vacancy recombination radius (r_v)	nm	0.57	[28]
Cascade efficiency (ξ)	-	0.4	[28]
Displacement per atom cross-section (σ_{dpa})	m^2	1.5×10^{-25}	[28]
Atomic volume (Ω_a^3)	m^3	1.18×10^{-29}	[28]
Vacancy diffusion pre-exponential (D_v)	m^2/s	1×10^{-4}	[28]
Vacancy migration energy (E_v^m)	eV	1.1	[28]

Dislocation sink strength (k^2)	m^{-2}	6.25×10^{14}	[28]
Reference flux (ϕ_r)	$m^{-2}s^{-1}$	3×10^{15}	[28]
Flux effect scaling exponential factor (p)	-	0.5	[28]
Cascade cross-section (σ_{cas})	m^2	2×10^{-28}	[28]
Reference solute product (K^0_{sp})	-	2.4×10^{-3}	[28]
Heterogeneous nucleation size (n_{het})	-	80	[28]
Cascade cluster production efficiency (α)	-	4.8×10^{-3}	[28]
Interfacial energy of T3 phase (γ_{T3})	J/m^2	0.185	[28]
Interfacial energy of T6 phase (γ_{T6})	J/m^2	0.175	[28]
Flux	$Particle/m^2s$	5.52×10^{15}	[28]
Dose rate (reference)	dpa/s	2.23×10^{-4}	[28]
Diffusivity of Mn in Fe at 370 °C (D^{th}_{Mn})	m^2/s	1.46×10^{-23}	[38,39]
Diffusivity of Ni in Fe at 370 °C (D^{th}_{Ni})	m^2/s	1.52×10^{-24}	[38,39]
Diffusivity of Si in Fe at 370 °C (D^{th}_{Si})	m^2/s	1.21×10^{-23}	[38,39]
Fe self-diffusivity at 370 °C (D^{th}_{Fe})	m^2/s	6.42×10^{-24}	[38,39]
Equilibrium solute product - T3 phase (K^{T3}_{sp})	$\times 10^{-3}$	4.82	[28]
Equilibrium solute product - T6 phase (K^{T6}_{sp})	$\times 10^{-3}$	5.20	[28]
Irradiation temperature	K	643	This study
Composition of Si (C_{si})	at%	0.55	Table 4.1
Composition of Mn (C_{Mn})	at%	0.45	Table 4.1

Table 4.3. Parameters used in cluster dynamics (CD) calculation for HCM12A.

Parameter	**Units**	**Neutron irradiation (500 °C)**	**Fe^{2+} irradiation (500 °C)**	**Fe^{2+} irradiation (370 °C)**	**Source(s)**
SIA – Vacancy recombination radius (r_v)	nm	0.57	0.57	0.57	[28,38]
Cascade efficiency (ξ)	-	0.4	0.4	0.4	[28,38]
Displacement per atom cross-section (σ_{dpa})	m^2	1.5×10^{-25}	1.5×10^{-25}	1.5×10^{-25}	[28,38]
Atomic volume (Ω_a^3)	m^3	1.18×10^{-29}	1.18×10^{-29}	1.18×10^{-29}	[28,38]
Vacancy diffusion pre-exponential (D_v)	m^2/s	1×10^{-4}	1×10^{-4}	1×10^{-4}	[28,38]
Vacancy migration energy (E_v^m)	eV	1.1	1.1	1.1	[28,38]
Dislocation sink strength (k^2)	m^{-2}	2.9×10^{15}	2.9×10^{15}	2.9×10^{15}	[28,38]
Reference flux (ϕ_r)	$m^{-2}s^{-1}$	3×10^{15}	3×10^{15}	3×10^{15}	[28,38]
Flux effect scaling exponential factor (p)	-	0.2	0.5	0.5	[28,38]
Cascade cross-section (σ_{cas})	m^2	2×10^{-28}	2×10^{-28}	2×10^{-28}	[28,38]
Reference solute product (K_{sp}^0)	-	2.4×10^{-3}	2.4×10^{-3}	2.4×10^{-3}	[28,38]
Heterogeneous nucleation size (n_{het})	-	80	80	80	[28,38]

Cascade cluster production efficiency (α)	-	4.8×10^{-3}	4.8×10^{-3}	4.8×10^{-3}	[28,38]
Interfacial energy of T3 phase (γ_{T3})	J/m^2	0.185	0.185	0.185	[28,38]
Interfacial energy of T6 phase (γ_{T6})	J/m^2	0.175	0.175	0.175	[28,38]
Flux	particle $/m^2s$	6.67×10^{17}	5.52×10^{15}	5.52×10^{15}	[28,38]
Dose rate (reference)	dpa/s	1.0×10^{-7}	2.23×10^{-4}	2.23×10^{-4}	[23,28]
Diffusivity of Mn in Fe (D^{th}_{Mn})		2.29×10^{-20}	2.29×10^{-20}	1.46×10^{-23}	[38,39]
Diffusivity of Ni in Fe (D^{th}_{Ni})	m^2/s	3.45×10^{-21}	3.45×10^{-21}	1.52×10^{-24}	[38,39]
Diffusivity of Si in Fe (D^{th}_{Si})	m^2/s	1.76×10^{-20}	1.76×10^{-20}	1.21×10^{-23}	[38,39]
Fe self-diffusivity (D^{th}_{Fe})	m^2/s	1.89×10^{-20}	1.89×10^{-20}	6.42×10^{-24}	[38,39]
Equilibrium solute product - T3 phase (K^{T3}_{sp})	$\times 10^{-3}$	12.71	12.71	4.82	[28,38,39]
Equilibrium solute product - T6 phase (K^{T6}_{sp})	$\times 10^{-3}$	13.07	13.07	5.20	[28,38,39]
Composition of Si (C_{si})	at%	0.55	0.55	0.55	Table 4.1
Composition of Mn (C_{Mn})	at%	0.45	0.45	0.45	Table 4.1

Composition of Ni (C_{Ni})	at%	0.20	0.20	0.20	Table 4.1
Irradiation temperature	K	773	773	643	This study

Just like the cluster dynamic model, another model based on rate theory and the work of Nelson, Hudson, and Mazey (NHM) [35] was also developed to simulate nanocluster evolution in F/M alloys. This model describes nanocluster radius (r) evolution over time (t) as [40]:

$$\frac{dr}{dt} = -\frac{\phi}{N} - lfK + \frac{3D^{irr}C}{4\pi pr} - D^{irr}r^2n \qquad (3)$$

This relationship depends on multiple conditions: 1) the irradiation time defined by the flux (ϕ) and dose rate (K), 2) the target alloy, defined by the atomic density (N), solute matrix concentration (C), and solute clustering amount (p), and 3) the existing nanocluster average size (r) and number density (n). Since the target alloy is b.c.c Fe based, we estimate the value of N to be 85.2 atoms/m^3. An estimate for *l*, the effective cascade diameter for different irradiating particles has been outline in [23], to be ~6.6 nm and ~ 9.3 nm for Fe^{2+} and neutron irradiation respectively. Nelson et al [35], suggested the disordering efficiency, *f*, could be used as a fitting parameters with the available data. The value of C and p can be obtained from the atom probe analysis while diffusion parameters are obtained from the literatures. A value for *dr/dt* is calculated for each irradiation and its applied over a define time increment, Δt, after which an evolved nanocluster radius is determined. The value of Δt ranges from 1.2 x 10^3 seconds for irradiation dose rates ~2 x 10^{-4}dpa/sec to 1.44 x 10^6 seconds for irradiation dose rates ~10^{-7} dpa/sec, such that each time step represents a

consistent dose increment, regardless of dose rate. An estimate for the sink strength and more details about the NHM model can be found in [41]. A summary of the initial parameters used in the modeling of the F/M alloys for each irradiation are provided in Table 4.4

Table 4.4. Initial parameters in the NHM model for T91 and HCM12A

Parameter	Units	HCM12A		T91		Source
		Fe^{2+} irradiation	**Neutron irradiation**	**Fe^{2+} irradiation**	**Neutron irradiation**	
K	dpa/s	2.23×10^{-4}	1×10^{-7}	2.23×10^{-4}	1×10^{-7}	[23]
$\phi = K(10^{14})$	atoms/cm^2-s	2.23×10^{10}	1.00×10^{7}	2.23×10^{10}	1.00×10^{7}	[23]
N	atoms/nm^3	85.2	85.2	85.2	85.2	[40]
Ψ	nm	0.58	1.21	0.58	1.21	[40]
k^2	cm^{-2}	2.90×10^{11}	2.90×10^{11}	1.05×10^{11}	1.05×10^{11}	[40]
T	K	773	773	773	773	[23,28]
$Q^m_{Si,Mn,Ni}$	eV	2.48	2.48	2.48	2.48	[40]
Q^m_{Cu}	eV	2.78	2.78	2.78	2.78	[40]
$D^0_{Si,Mn,Ni}$	cm^2/s	1.4×10^{-4}	1.4×10^{-4}	1.4×10^{-4}	1.4×10^{-4}	[40]
D^0_{Cu}(cm^2/s)	cm^2/s	3.0×10^{-2}	3.0×10^{-2}	3.0×10^{-2}	3.0×10^{-2}	[40]
E^f_v	eV	1.65	1.65	1.65	1.65	[40]
E^m_v	eV	0.68	0.68	0.68	0.68	[53]
r	nm	0.0	0.0	0.00	0.00	-
n	m^{-3}	0.0	0.0	0.00	0.00	-
$p_{Si,Mn,Ni}$	-	0.001	0.001	0.08	0.18	[40]
p_{Cu}	-	0.001	0.001	0.07	0.10	[40]
$C_{Si,Mn,Ni}$	-	0.0212	0.0212	0.01	0.01	[40]
C_{Cu}	-	0.0132	0.0132	0.001	0.001	[40]
Δt	s	1200	1440000	1200	1440000	This study

The outcome of the two models suggest the need for an experimental temperature shift when irradiating with charge particles at higher dose rate to accurately emulate neutron

irradiation. To quantify the predicted temperature shift using the CD and NHM simulations, we iteratively evaluated several alternative temperature inputs into the two models. In the CD model, alternative temperatures not only affect the irradiation temperature parameter, but also the values for the respective solute diffusivities and equilibrium solute product parameters. Interestingly, both the NHM and CD models predict that a revised temperature of 360 – 380 °C will be needed for Fe^{2+} to closely emulate neutron-irradiation at 500 °C, suggesting a negative temperature shift for Fe^{2+} to emulate neutron irradiation (Fig. 4.1).

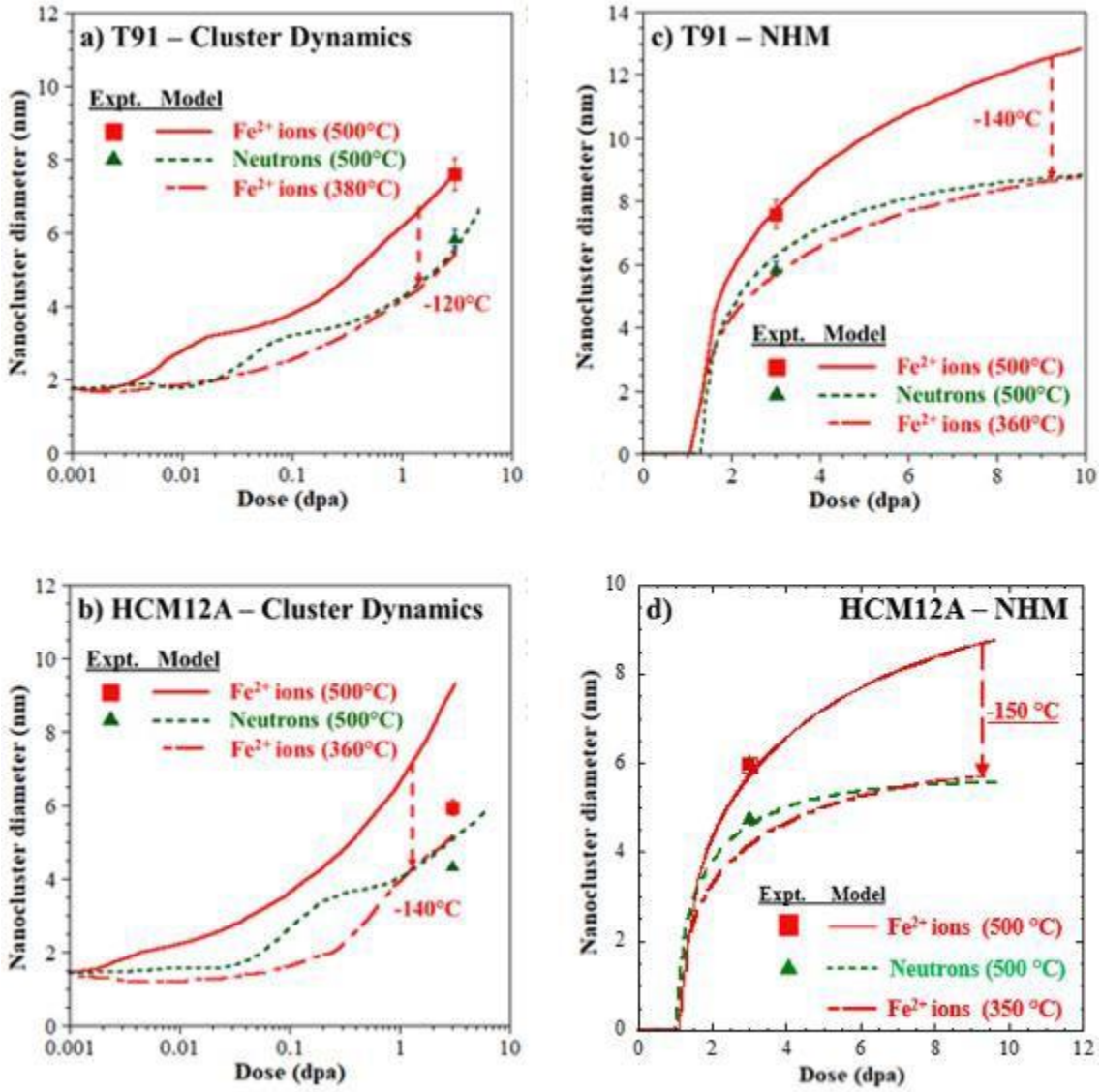

Figure 4.1. Experimental results compared with model simulations of Si-Mn-Ni-rich nanocluster evolution in alloys T91 and HCM12A using cluster dynamics and NHM models.

It is important to note that the cluster dynamic model is not programmed to simulate Cu rich nanoclusters, and neither of them are developed for Cr rich (α') clusters, but we will nevertheless evaluate the predicted temperature shift for these types of clusters, too.

Irradiation

To evaluate the efficacy of the cluster dynamic and NHM predictions, we carried out Fe^{2+} irradiation at the prescribed temperature of 370 °C (3 dpa). Specimens were prepared from the same heat of alloy T91, HCM12A, and HT9 for 5 MeV Fe^{2+} irradiation to 3 dpa at 370 °C. We added HT9 to the experiment because we believe the prescribed temperature shift will be applicable to all bcc Fe based alloys. In prior study [23], no nanocluster was observed in HT9 after Fe^{2+} irradiation to 3 dpa at 500 °C but high number density of Si-Mn-Ni clusters were observed following neutron irradiation to 3 dpa at 500 °C. Therefore, it will be interesting to see if Fe^{2+} irradiation of HT9 to 3 dpa at the prescribed temperature shift will induce Si-Mn-Ni rich nanoclusters. Prior to irradiation, specimens were cut via electrical discharge machining into 1.5 mm x 1.5 mm x 20 mm bars. The bars were each mechanically polished using SiC paper up to 4000 grit and subsequently electropolished for ~20 seconds in a 10% perchloric acid +90% methanol solution at -40°C with an applied potential of 35 V between the specimen (anode) and platinum mesh cathode. The Fe^{2+} irradiation was conducted at the Michigan Ion Beam Laboratory using a raster-scanned beam in the General Ionex Tandetron accelerator. The Stopping and Range of Ions in Matter (SRIM) software [42] was used to calculate displacement damage for the self-ion irradiation using a displacement energy of 40 eV. The full damage profile using the "Quick Calculation (K-P)" mode is found in Figure 4.2 with the damage peak located at ~1.2 μm for Fe^{2+} irradiation. Microstructural characterization was targeted at depths of 400 - 600 nm in the Fe^{2+} irradiated specimens to avoid any surface effect and the steep irradiation dose gradient near the damage peak. The result of Fe^{2+} irradiation irradiation at 370 °C will be compared to those obtained in the same alloy after Fe^{2+} and neutron irradiation at 500 °C

Atom probe tomography

Evaporation of each APT needles was performed at the center for advanced energy studies (CAES) using Cameca instrument LEAP 4000X HR. Prior to atom probe analysis, the samples were sharpened to needle shape using the focused ion beam (FIB) milling on a Quanta 3D 200i dual beam scanning electron microscope. The fabrication techniques including sample wedge liftout, mounting onto silicon posts, partitioning into 6-8 samples, and milling with annular ring patterns to a tip radius ≤50 nm, consistent with the methods described in [43].

After sample preparation, evaporation was conducted in laser mode. The sample temperature was cooled to 50K, the repetition rate was 200 Hz, and the laser pulse energy at 50 pJ. Reconstruction of atom maps and analysis of precipitates from the data was done using the Integrated Visualization and Analysis Software (IVAS) Version 3.8.4. The ICF values for each reconstruction are determined using the new pole indexing module in IVAS using the method described in [28], the adjusted ICF was used in the reconstruction of the dataset. The elements were identified via their mass-to-charge ratios and the overall isotope abundance of the species known to be present in the composition of the alloy. Peak overlap occurs in a number of places such as at a mass-to-charge ratio of 29, which is likely made up of a combination of $^{58}Fe^{2+}$ and $^{58}Ni^{2+}$ ions. In this case, the peak is identified at $^{58}Fe^{2+}$ since the majority of these ions are found to be of Fe using peak deconvolution. This approach enables consistent and repeatable ranging between each specimen. The size of the data sets ranged from ~9 – 20 million ion counts per needle.

For cluster analysis, maximum separation method was used [44]. This method gives detailed information about clusters, and also gather information about their numbers, composition, and density. The accuracy of cluster analysis depends primarily on the selection of two parameters, d_{max} and N_{min}. The approach used for this study follows those of [45,46]. While attempting to optimize the values for d_{max}, a common phenomenon is observed in which a bimodal distribution of possible cluster counts was observed. Too small of values for d_{max} will split a single cluster into multiple identified clusters, while too large of values for d_{max} provide a greater chance of spuriously identifying clusters in the matrix. Therefore, the optimum values for d_{max} and N_{min} are selected to identify only the clusters and not the nearby matrix, as well as to reduce the identification of random clusters in each reconstruction. The d_{max} and N_{min} values range from 0.60 – 0.86 and 18 – 50, respectively. Each result is visually inspected to confirm the identified clusters are consistent with those identified with isosurfaces created with an ~3 - 6% concentration threshold, and those visible in the reconstruction images.

The cluster radii, number densities, and volume fraction of clusters under different irradiation conditions were obtained from the IVAS cluster analysis output .cvs files, which provide values for R_{gx}, R_{gy}, and R_{gz} from each cluster. For each cluster, the Guinier diameter was calculated using accepted techniques in [23,47,48]. The nanocluster number density (N_{nc}) was determined by dividing the total number of clusters identified in all tips by the total analyzed volume in all characterized tips from that specimen. The volume fraction of clusters (f_v) is found by counting the total number of atoms in the measured clusters and dividing by the total number of atoms in the combined reconstructed volumes. The IVAS output file also

includes detailed composition of each cluster and the matrix, enabling simple determination of the surrounding matrix composition () and the total specimen composition (C_i).

Results

Si, Mn, Ni, and Cu-rich atom distribution of each specimen of T91, HCM12A, and HT9 following Fe^{2+} ion irradiation to a dose of 3 dpa at 370 °C is represented in Figure 4.2. Each specimen of T91 and HCM12A exhibit nucleation and clustering of Si-Mn-Ni and Cu-rich nanoclusters following Fe^{2+} irradiation to a common dose of 3 dpa at 370 °C. HT9 also exhibit nucleation and clustering of Si-Mn-Ni-rich clusters after irradiation to a dose of 3 dpa at 370 °C, there is no evidence of Cu clustering because of the low concentration of Cu in HT9. The average size, number density, and composition of nanoclusters in alloys T91, HCM 12A, and HT9 following irradiation to various conditions are provided in Table 4.5 and plotted in Figure 4.3.

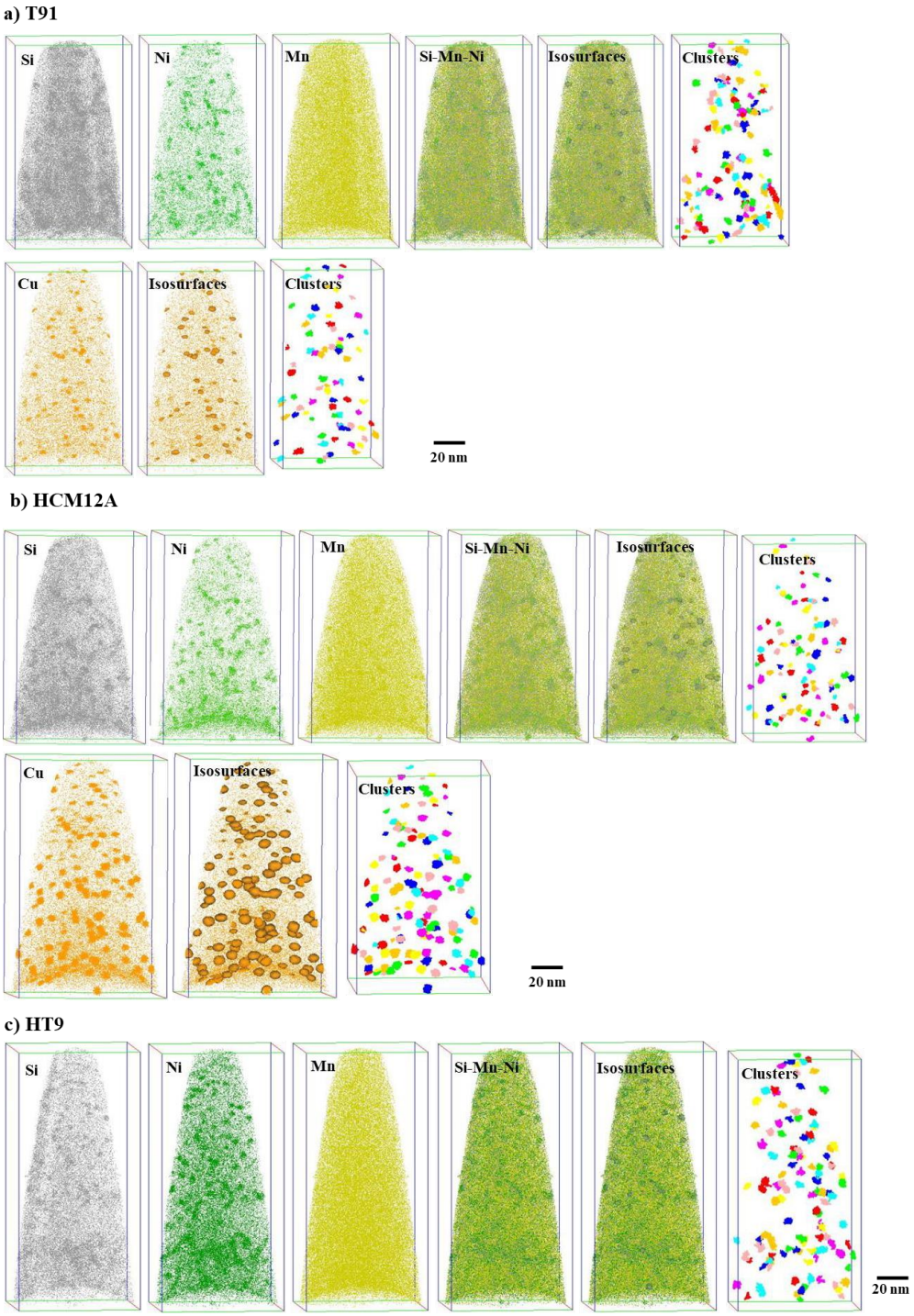

Figure 4.2. Atom probe distribution maps of Si-Mn-Ni and Cu solutes in following Fe2+ irradiation to 370 °C a) T91 b) HCM12A, and c) HT9. All irradiations are at a dose of 3 dpa.

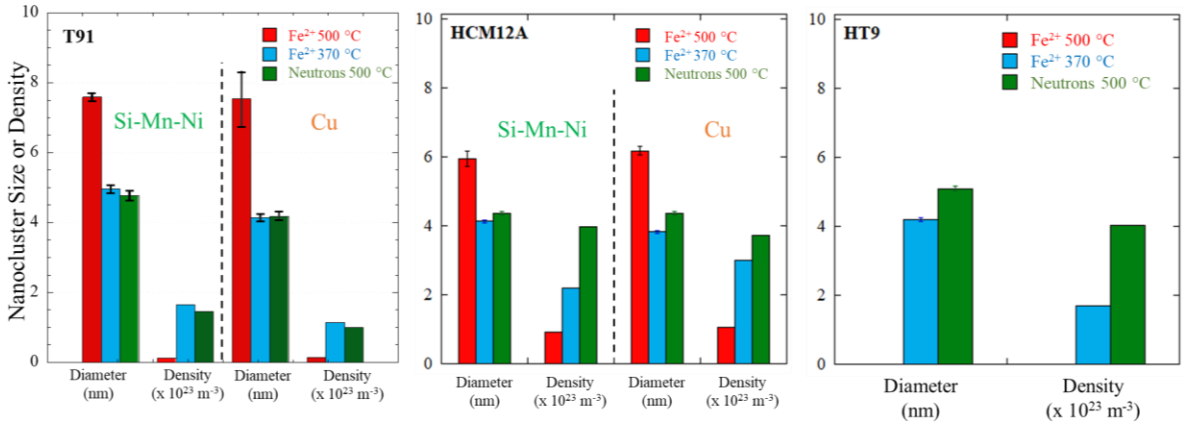

Figure 4.3. Summary of Si-Mn-Ni-rich and Cu-rich nanocluster morphologies and solute matrix compositions following neutron or self-ion irradiation in a) T91, b) HCM12A, and c) HT9

Table 4.5. Summary of cluster analysis of T91, HCM12A, and HT9 for each irradiation condition using APT.

Nanocluster Analysis		**Fe^{2+} ions 3 dpa (500 °C)**	**Fe^{2+} ions 3 dpa (370 °C)**	**Neutrons 3 dpa (500 °C)**
T91	Analysis Volume, V_T (nm^3)	658,876	2,866,932	1,507,647
	Si-Mn-Ni-rich clusters			
	# of clusters measured, $\sum N_{cl}^{Si}$	8	473	219
	Average diameter, D_G^{Si} (nm)	7.59	4.96	4.78
	Standard deviation for D_G^{Si}	1.50	1.46	1.63
	Std. dev. of the mean for D_G^{Si}	0.53	0.07	0.11
	Density, N_{nc}^{Si} (x 10^{21} m^{-3})	12	165	145
	Volume fraction, f_v	0.48%	0.81	1.48%
	Solute matrix composition, c_m^{Si}	1.2 at%	1.03%	0.88 at%
	Cu-rich clusters			
	# of clusters measured, $\sum N_{cl}^{Cu}$	9	331	151

	Average diameter, D_G^{Cu} (nm)	7.54	4.14	4.18
	Standard deviation for D_G^{Cu}	2.32	1.63	1.07
	Std. dev. of the mean for D_G^{Cu}	0.77	0.09	0.09
	Density, N_{nc}^{Cu} (x 10^{21} m^{-3})	14	115	100
	Volume fraction, f_v	0.32%	0.57%	0.70%
	Solute matrix composition, c_m^{Cu}	0.14 at%	0.12%	0.10 at%
HCM12A	Analysis Volume, V_T (nm^3)	811,282	1,836,900	572,186
	Si-Mn-Ni-rich clusters			
	# of clusters measured, $\sum N_{cl}^{Si}$	75	402	228
	Average diameter, D_G^{Si} (nm)	5.95	4.13	4.36
	Standard deviation for D_G^{Si}	2.01	1.07	0.80
	Std. dev. of the mean for D_G^{Si}	0.23	0.05	0.05
	Density, N_{nc}^{Si} (x 10^{21} m^{-3})	92	219	398
	Volume fraction, f_v	1.10%	1.41	2.8%
	Solute matrix composition, c_m^{Si}		1.25%	
	Cu-rich clusters			
	# of clusters measured, $\sum N_{cl}^{Cu}$	87	551	213
	Average diameter, D_G^{Cu} (nm)	6.18	3.83	4.59
	Standard deviation for D_G^{Cu}	1.26	0.94	0.90
	Std. dev. of the mean for D_G^{Cu}	0.13	0.04	0.06
	Density, N_{nc}^{Cu} (x 10^{21} m^{-3})	107	300	372
	Volume fraction, f_v	2.50%	2.47%	3.10%
	Solute matrix composition, c_m^{Cu}	-	0.2%	-
HT9	Analysis Volume, V_T (nm^3)	643,426	1,572,925	1,275,897
	Si-Mn-Ni-rich clusters			
	# of clusters measured, $\sum N_{cl}^{Si}$	-	268	515
	Average diameter, D_G^{Si} (nm)	-	4.12	5.09
	Standard deviation for D_G^{Si}	-	0.78	4.19
	Std. dev. of the mean for D_G^{Si}	-	0.05	0.18
	Density, N_{nc}^{Si} (x 10^{21} m^{-3})	-	170	404
	Volume fraction, f_v	-	0.62%	3.80%
	Solute matrix composition, c_m^{Si}	-	0.98%	-

Fe^{2+} irradiation was also conducted at 500 °C to 3dpa to allow for direct comparison of nanoclusters at different temperatures [23,28]. Si-Mn-Ni rich and Cu rich clusters are observed following Fe^{2+} ion irradiation of T91 and HCM12A to a dose of 3 dpa at a temperature of 370 °C and 500 °C. HT9 also exhibit nucleation and clustering of Si-Mn-Ni-rich clusters after irradiation to a dose of 3 dpa at 370 °C. For T91 specimen, a total of 473 and 8 Si-Mn-Ni rich nanoclusters are identified and analyzed following Fe^{2+} irradiation to 370 °C and 500 °C respectively. The average size of the nanoclusters increases from 4.96 nm to 7.59 nm while the number density decreases from 165 x 10^{21} m^{-3} to 12 x 10^{21} m^{-3} as the irradiation temperature increases from 370 °C to 500 °C respectively. Cu-rich nanoclusters are also seen to coarse as the irradiation temperature increases, the size increases from 4.14 nm to 7.54 nm, while the number density decreases from 116 x 10^{21} m^{-3} to 14 x 10^{21} m^{-3}.

In HCM12A, a total of 402 and 75 Si-Mn-Ni rich nanoclusters are analyzed following Fe^{2+} irradiation to 370 °C and 500 °C respectively. Similar effect of temperature on nanocluster size and number density as in T91 was also observed in HCM12A. The average size of Si-Mn-Ni rich clusters increases from 4.13 nm to 5.95 nm as the irradiation temperature increases from 370 °C to 500 °C, while the number density decreases from 219 x 10^{21} m^{-3} to 92 x 10^{21} m^{-3}. For Cu rich nanoclusters, a total of 551 and 87 clusters are identified and analysed following irradiation to 370 °C and 500 °C respectively. At 500 °C, the average size of the clusters increases to 6.18 nm from 3.83 nm at 370 °C, the number density decreases to 107 x 10^{21} m^{-3} from 300 x 10^{21} m^{-3} at 370 °C.

In HT9 specimen, a total of 551 Si-Mn-Ni rich clusters are analyzed after Fe^{2+} irradiation to 370 °C (3 dpa). The size and number density of Si-Mn-Ni rich nanoclusters is 4.19 nm and 170 x 10^{21} m^{-3} respectively. There was no clustering of Cu in this alloy because

of the low Cu content in HT9, and also there is no evidence of Si-Mn-Ni rich clusters at irradiation temperature of 500 °C but solute segregation is observed on the grain boundary as reported in [23].

Nanoclusters are seen to be more finely distributed after Fe^{2+} irradiation at 370 °C. This observation is in agreement with the report of Jiao et al. [49] who also observed increase size and decreasing number density of Ni/Si nanoclusters as the temperature increases from 376–415 °C following neutron irradiation of T91 to ~18 dpa.

Discussion

Effect of temperature on the evolution of Si-Mn-Ni and Cu rich nanoclusters

In this study, Si-Mn-Ni rich and Cu rich nanoclusters are observed to be present at the irradiation temperature between 370-500 °C in all the three alloys investigated. Irradiation temperature have shown to have a strong influence on the size and number density of Si-Mn-Ni and Cu rich nanoclusters. The present work shows the size of the nanoclusters increases as the temperature increases, while the number density decreases. This trend is consistent with the prediction of the cluster dynamic modeling, the model predicts larger clusters size as the irradiation temperature increases. Increased temperature increases the radiation enhanced diffusion of solutes i.e solutes have more energy to move freely through the vacancies thus increasing the growth and coarsening of solute nanoclusters via Oswald ripening. The temperature effect is the same across the three alloys investigated. This solute clustering behavior in the three alloys is a consistent with result of Jiao et al [11], who conducted proton irradiation on T91, HCM 12A, and HT9, to a dose of 7 dpa at irradiation temperature of 400

°C and 500 °C. He also observed the nucleation of Si-Mn-Ni in the three alloys just as in this study, and the size of the Si-Mn-Ni clusters is observed to increase with increase temperature while the number density decreases.

Comparison with neutron irradiation

T91, HCM12A, and HT9 alloys were also neutron irradiated to 3 dpa at 500 °C, full APT characterization is available in [23,28]. Figure 4.2 and 4.4 include the 3D reconstruction of neutron and Fe^{2+} irradiated T91, HCM12A, and HT9 making a direct comparison possible between neutron at 500 °C and Fe^{2+} ion irradiation at 370 °C. The present work showed that the size and number density of Si-Mn-Ni rich and Cu rich nanolcusters following Fe^{2+} irradiation at 370 °C in the investigated alloys is comparable to the properties of the Si-Mn-Ni and Cu rich nanoclusters after neutron irradiation at 500 °C. This result validates the negative temperature shift prescription of the cluster dynamic and the NHM models. However, this result is inconsistent with the positive temperature shift predicted by Mansur, the idea of Mansur invariance theory [25] is that in the diffusion dominated regime, higher dose rate irradiation induces higher number density of defect compared to lower dose rate irradiation. To offset this effect, irradiation should be conducted at a higher temperature so as increase the mobility of defects as well as defect recombination and annihilation at sink. Mansur's theory only focus on defect cluster and not solute clusters. But, this result is consistent with the Martin's temperature dilation theory. According to Martin [50], higher dose rate irradiation causes a rise in the temperature of the system giving solutes more energy and space to move freely through the vacancies as a result of the increased effect of radiation

enhanced diffusion thus favoring coalesce and growth of solute nanoclusters. To reduce the effect of radiation enhanced diffusion, irradiation at higher dose rate needs to be conducted at lower temperature so as to reduce the mobility of solutes and defects in order to attain a comparable nanocluster morphology to that of lower dose rate irradiation. This idea has also been supported by Zinkle and Snead [51] who also believes that a single temperature shift cannot be applied to compensate for the effect of dose rate.

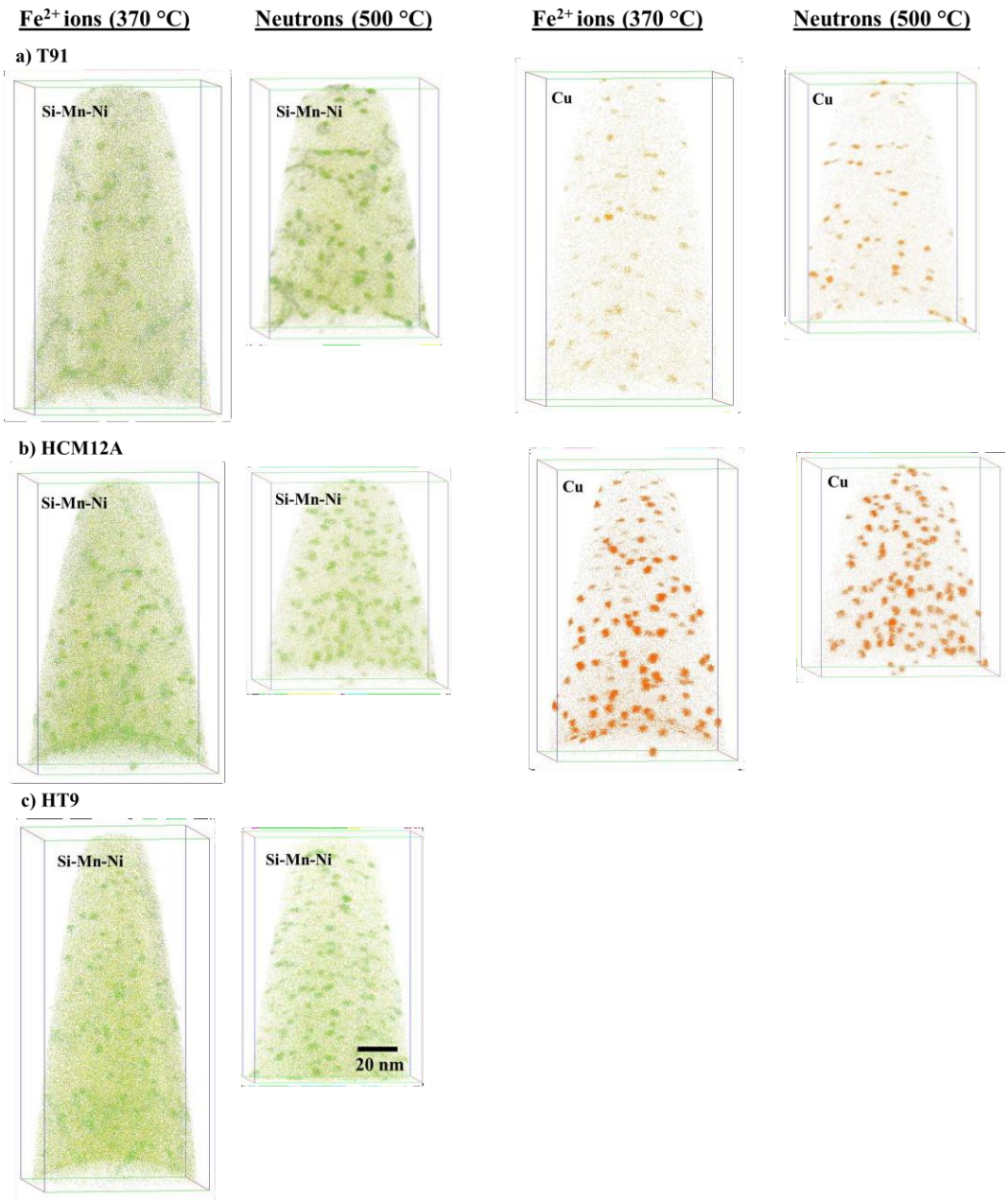

Figure 4.4. APT reconstruction of a) T91, b) HCM12A, and c) HT9 after ion irradiation at 370 °C and neutron irradiation at 500 °C. All irradiation is at a dose of 3 dpa.

Cr rich prcipitates

A high number density of α'clusters are seen to precipitate following neutron irradiation of HCM12A and HT9 to 3 dpa at 500 °C as shown in Figure 4.5. For HCM12A, the average size and number density are 3.17 ± 0.03 nm and 355 x $10^{21}m^{-3}$ respectively and in HT9, the average size and number density of Cr rich precipitates are 4.27±0.02 nm and 1273 x 10^{21} m^{-3} respectively [23]. The larger size and higher number density of Cr rich precipitates observed in HT9 is due to its high Cr content. This is in total agreement with the finding of Bachhav et al [24] who also confirmed that the size and number density of Cr rich precipitates increases with increasing Cr content. However, no α' cluster was observed after Fe^{2+} ion irradiation of HCM12A and HT9 to 3 dpa at 370 °C, this is likely due to Fe^{2+} ion irradiation is conducted at a short experimental time frame (in few hours) while it takes neutrons irradiation months to reach the same damage level as Fe^{2+}irradiation, so a longer irradiation time is needed for the nucleation and growth of Cr rich nanoclusters. This confirms that the evolution of Cr-rich precipitates is time dependent. The absence of α' in T91 after neutron or Fe^{2+} irradiation is because it has a lower Cr content than HCM12A and HT9, and again its Cr content falls within the solubility limit of Cr in Fe.

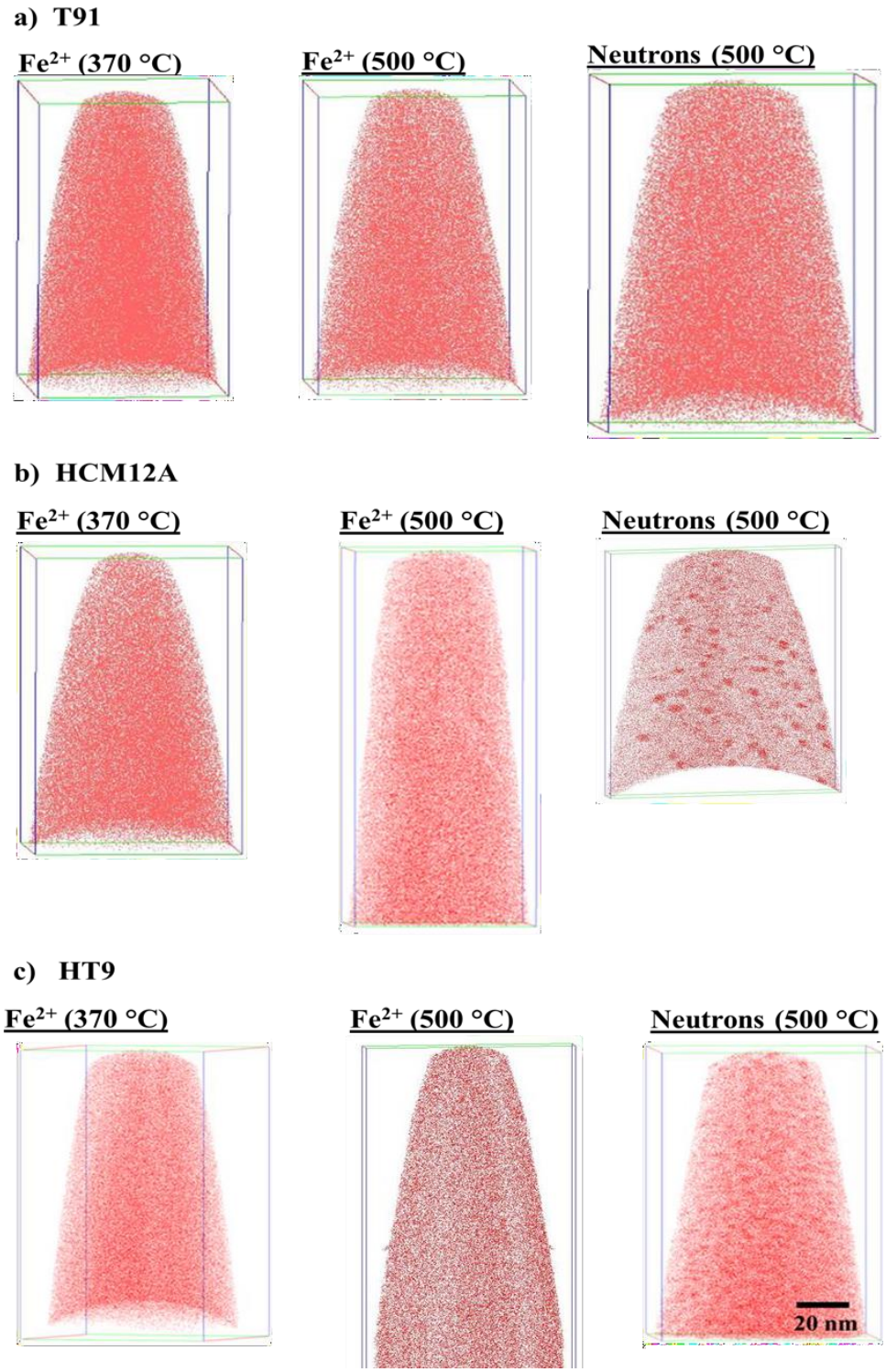

Figure 4.5. APT reconstruction showing distribution of α' precipitate after neutron or Fe2+ irradiation in a) T91 b) HCM12A, and c) HT9

Literature Cited

[1] J. Henry, S.A. Maloy, Irradiation-resistant ferritic and martensitic steels as core materials for Generation IV nuclear reactors, Elsevier Ltd, 2017. https://doi.org/10.1016/B978-0-08-100906-2.00009-4.

[2] T. Allen, K. Djamel, J.P. Wharry, Z. Jiao, Characterization of microstructure and property evolution in advanced cladding and duct: Materials exposed to high dose and elevated temperature, J. Mater. Res. (2015). https://doi.org/10.1557/jmr.2015.99.

[3] B.H. Sencer, J.R. Kennedy, J.I. Cole, S.A. Maloy, F.A. Garner, Microstructural stability of an HT-9 fuel assembly duct irradiated in FFTF, J. Nucl. Mater. 414 (2011) 237–242. https://doi.org/10.1016/j.jnucmat.2011.03.050.

[4] X. Jia, Y. Dai, Microstructure in martensitic steels T91 and F82H after irradiation in SINQ Target-3, J. Nucl. Mater. 318 (2003) 207–214. https://doi.org/10.1016/S0022-3115(03)00101-6.

[5] P. Ampornrat, G.S. Was, Oxidation of ferritic-martensitic alloys T91, HCM12A and HT-9 in supercritical water, J. Nucl. Mater. 371 (2007) 1–17. https://doi.org/10.1016/j.jnucmat.2007.05.023.

[6] J.J. Kai, R.L. Klue, Microstructural analysis of neutron-irradiated martensitic steels, J. Nucl. Mater. 230 (1996) 116–123. https://doi.org/10.1016/0022-3115(96)00165-1.

[7] J. Van Den Bosch, O. Anderoglu, R. Dickerson, M. Hartl, P. Dickerson, J.A. Aguiar, P. Hosemann, M.B. Toloczko, S.A. Maloy, SANS and TEM of ferritic – martensitic

steel T91 irradiated in FFTF up to 184 dpa at 413 °C, J. Nucl. Mater. 440 (2013) 91–97. https://doi.org/10.1016/j.jnucmat.2013.04.025.

[8] P. Dubuisson, D. Gilbon, J.L. Seran, Microstructural evolution of ferritic-martensitic steels irradiated in the fast breeder reactor Phénix, J. Nucl. Mater. 205 (1993) 178–189. https://doi.org/10.1016/0022-3115(93)90080-I.

[9] O. Anderoglu, J. Van Den Bosch, P. Hosemann, E. Stergar, B.H. Sencer, D. Bhattacharyya, Phase stability of an HT-9 duct irradiated in FFTF, J. Nucl. Mater. 430 (2012) 194–204. https://doi.org/10.1016/j.jnucmat.2012.06.038.

[10] E.R. Reese, M. Bachhav, P. Wells, T. Yamamoto, G.R. Odette, E.A. Marquis, On α′ precipitate composition in thermally annealed and neutron-irradiated Fe- 9-18Cr alloys, J. Nucl. Mater. 500 (2018) 192–198. https://doi.org/10.1016/j.jnucmat.2017.12.036.

[11] Z. Jiao, V. Shankar, G.S. Was, Phase stability in proton and heavy ion irradiated ferritic-martensitic alloys, J. Nucl. Mater. 419 (2011) 52–62. https://doi.org/10.1016/j.jnucmat.2011.08.020.

[12] G. Gupta, Z. Jiao, A.N. Ham, J.T. Busby, G.S. Was, Microstructural evolution of proton irradiated T91, J. Nucl. Mater. 351 (2006) 162–173. https://doi.org/10.1016/j.jnucmat.2006.02.028.

[13] J.E. Zelenty, Understanding thermally induced embrittlement in low copper RPV steels utilising atom probe tomography, Mater. Sci. Technol. (2016). https://doi.org/10.1179/1743284714Y.0000000718.

[14] J.W.P. Schmelzer, A.S. Abyzov, J. Moller, Nucleation versus spinodal decomposition in phase formation processes in multicomponent solutions, J. Chem. Phys. 6900 (2004). https://doi.org/10.1063/1.1786914.

[15] G.R. Odette, G.E. Lucas, Embrittlement of Nuclear Reactor Pressure Vessels, J. Miner. Met. Mater. Soc. (2001) 18–22. https://doi.org/10.1007/s11837-001-0081-0.

[16] J.P. Wharry, Z. Jiao, V. Shankar, J.T. Busby, G.S. Was, Radiation-induced segregation and phase stability in ferritic-martensitic alloy T 91, J. Nucl. Mater. 417 (2011) 140–144. https://doi.org/10.1016/j.jnucmat.2010.12.052.

[17] L.T. Belkacemi, E. Meslin, B. Décamps, B. Radiguet, J. Henry, Radiation-induced bcc-fcc phase transformation in a Fe–3%Ni alloy, Acta Mater. 161 (2018) 61–72. https://doi.org/10.1016/j.actamat.2018.08.031.

[18] R. Ngayam-Happy, C.S. Becquart, C. Domain, L. Malerba, Formation and evolution of MnNi clusters in neutron irradiated dilute Fe alloys modelled by a first principle-based AKMC method, J. Nucl. Mater. 426 (2012) 198–207. https://doi.org/10.1016/j.jnucmat.2012.03.033.

[19] G. Bonny, D. Terentyev, A. Bakaev, E.E. Zhurkin, M. Hou, D. Van Neck, L. Malerba, On the thermal stability of late blooming phases in reactor pressure vessel steels: An atomistic study, J. Nucl. Mater. 442 (2013) 282–291. https://doi.org/10.1016/j.jnucmat.2013.08.018.

[20] C. Zheng, E.R. Reese, K.G. Field, E. Marquis, S.A. Maloy, D. Kaoumi, Microstructure response of ferritic/martensitic steel HT9 after neutron irradiation: Effect of

temperature, J. Nucl. Mater. (2019) 151845. https://doi.org/10.1016/j.jnucmat.2019.151845.

[21] C. Zheng, E.R. Reese, K.G. Field, E. Marquis, S.A. Maloy, D. Kaoumi, Microstructure response of ferritic / martensitic steel HT9 after neutron irradiation : effect of dose, J. Nucl. Mater. 523 (2019) 421–433. https://doi.org/10.1016/j.jnucmat.2019.06.019.

[22] C. Zheng, M.A. Auger, M.P. Moody, D. Kaoumi, Radiation induced segregation and precipitation behavior in self-ion irradiated Ferritic/Martensitic HT9 steel, J. Nucl. Mater. 491 (2017) 162–176. https://doi.org/10.1016/j.jnucmat.2017.04.040.

[23] M.J. Swenson, J.P. Wharry, Nanocluster irradiation evolution in Fe-9%Cr ODS and ferritic-martensitic alloys, J. Nucl. Mater. 496 (2017) 24–40. https://doi.org/10.1016/j.jnucmat.2017.08.045.

[24] M. Bachhav, G. Robert Odette, E.A. Marquis, α′ precipitation in neutron-irradiated Fe-Cr alloys, Scr. Mater. 74 (2014) 48–51. https://doi.org/10.1016/j.scriptamat.2013.10.001.

[25] L.K. Mansur, Correlation of Neutron and Heavy-Ion Damage, J. Nucl. Mater. 78 (1978) 156–160. https://doi.org/10.1016/S0022-3115(01)00751-6.

[26] A. Dunn, B. Muntifering, R. Dingreville, K. Hattar, L. Capolungo, Displacement rate and temperature equivalence in stochastic cluster dynamics simulations of irradiated pure α-Fe, J. Nucl. Mater. 480 (2016) 129–137. https://doi.org/10.1016/j.jnucmat.2016.08.018.

[27] D. Xu, G. Vancoevering, B.D. Wirth, Defect microstructural equivalence in molybdenum under different irradiation conditions at low temperatures and low doses, Comput. Mater. Sci. 114 (2016) 47–53. https://doi.org/10.1016/j.commatsci.2015.11.045.

[28] S.B. Adisa, R. Blair, M.J. Swenson, Comparison of microstructure evolution in Fe2+ or neutron-irradiated T91 at 500 °C, Materialia. (2019) 17. https://doi.org/10.1016/j.mtla.2020.100770.

[29] G.S. Was, Z. Jiao, E. Getto, K. Sun, A.M. Monterrosa, S.A. Maloy, O. Anderoglu, B.H. Sencer, M. Hackett, Emulation of reactor irradiation damage using ion beams, Scr. Mater. 88 (2014) 33–36. https://doi.org/10.1016/j.scriptamat.2014.06.003.

[30] Z. Jiao, J. Michalicka, G.S. Was, Self-ion emulation of high dose neutron irradiated microstructure in stainless steels, J. Nucl. Mater. 501 (2018) 312–318. https://doi.org/10.1016/j.jnucmat.2018.01.054.

[31] C. Pareige, V. Kuksenko, P. Pareige, Behaviour of P, Si, Ni impurities and Cr in self ion irradiated Fe-Cr alloys - Comparison to neutron irradiation, J. Nucl. Mater. 456 (2015) 471–476. https://doi.org/10.1016/j.jnucmat.2014.10.024.

[32] G.S. Was, J.T. Busby, T. Allen, E.A. Kenik, A. Jenssen, S.M. Bruemmer, J. Gan, A.D. Edwards, P.M. Scott, P.L. Andresen, Emulation of neutron irradiation effects with protons : validation of principle, J. Nucl. Mater. 300 (2002) 198–216. https://doi.org/10.1016/S0022-3115(01)00751-6.

[33] S. Taller, Z. Jiao, K. Field, G.S. Was, Emulation of fast reactor irradiated T91 using dual ion beam irradiation, J. Nucl. Mater. (2019) 151831. https://doi.org/10.1016/j.jnucmat.2019.151831.

[34] M.J. Swenson, J.P. Wharry, TEM characterization of irradiated microstructure of Fe-9 % Cr ODS and ferritic-martensitic alloys, J. Nucl. Mater. 502 (2018) 30–41. https://doi.org/10.1016/j.jnucmat.2018.01.062.

[35] R.S. Nelson, J.A. Hudson, D.J. Mazey, The Stability of Precipitates in an Irradiation Environment, Journals Nucl. Mater. 44 (1972) 318–330. https://doi.org/10.1016/0022-3115(72)90043-8.

[36] C. Wagner, Theory of the ageing of precipitates by redissolution (Ostwald maturing), Z. Elektrochemie. 65 (1961) 581 – 591.

[37] T. Chen, J.G. Gigax, L. Price, D. Chen, S. Ukai, E. Aydogan, S.A. Maloy, F.A. Garner, L. Shao, Temperature dependent dispersoid stability in ion-irradiated ferritic-martensitic dual-phase oxide-dispersion-strengthened alloy: Coherent interfaces vs. incoherent interfaces, Acta Mater. 116 (2016) 29–42. https://doi.org/10.1016/j.actamat.2016.05.042.

[38] H. Ke, P. Wells, P.D. Edmondson, N. Almirall, L. Barnard, G.R. Odette, D. Morgan, Thermodynamic and kinetic modeling of Mn-Ni-Si precipitates in low-Cu reactor pressure vessel steels, Acta Mater. 138 (2017) 1–51. https://doi.org/10.1016/j.actamat.2017.07.021.

[39] J.H. Ke, H. Ke, G.R. Odette, D. Morgan, Cluster dynamics modeling of Mn-Ni-Si precipitates in ferritic-martensitic steel under irradiation, J. Nucl. Mater. 498 (2018) 83–88. https://doi.org/10.1016/j.jnucmat.2017.10.008.

[40] M.J. Swenson, J.P. Wharry, Rate theory model of irradiation-induced solute clustering in b.c.c. Fe-based alloys, (n.d.).

[41] M.J. Swenson, The Mechanism of Radiation-Induced Nanocluster Evolution in Oxide Dispersion Strenthened and Ferritic-Martensitic Alloys, 2017.

[42] J.F. Ziegler, M.D. Ziegler, J.P. Biersack, SRIM – The stopping and range of ions in matter (2010), Nucl. Inst. Methods Phys. Res. B. 268 (2010) 1818–1823. https://doi.org/10.1016/j.nimb.2010.02.091.

[43] K. Thompson, D. Lawrence, D.J. Larson, J.D. Olson, T.F. Kelly, B. Gorman, In situ site-specific specimen preparation for atom probe tomography, Ultramicroscopy. 107 (2007) 131–139. https://doi.org/10.1016/j.ultramic.2006.06.008.

[44] J.M. Hyde, E.A. Marquis, K.B. Wilford, T.J. Williams, A sensitivity analysis of the maximum separation method for the characterisation of solute clusters, Ultramicroscopy. 111 (2011) 440–447. https://doi.org/10.1016/j.ultramic.2010.12.015.

[45] R.P. Kolli, D.N. Seidman, Comparison of Compositional and Morphological Atom-Probe Tomography Analysis for a Multicomponent Fe-Cu Steel, Microsc. Microanal. (2007). https://doi.org/10.1017/S1431927607070675.

[46] C.A. Williams, D. Haley, E.A. Marquis, G.D.W. Smith, M.P. Moody, Defining clusters in APT reconstructions of ODS steels, Ultramicroscopy. 132 (2013) 271–278. https://doi.org/10.1016/j.ultramic.2012.12.011.

[47] M.K. Miller, R. Forbes, Atom Probe Tomography: The Local Electrode Atom Probe, Springer, New York, 2014.

[48] C.A. Williams, E.A. Marquis, G.D.W.S. A. Cerezo, Nanoscale characterisation of ODS- Eurofer 97 steel: An atom-probe tomography study, J. Nucl. Mater. (2010) 37–45. https://doi.org/10.1016/j.jnucmat.2010.02.007.

[49] Z. Jiao, S. Taller, K. Field, G. Yeli, M.P. Moody, G.S. Was, Microstructure evolution of T91 irradiated in the BOR60 fast reactor, J. Nucl. Mater. 504 (2018) 122–134. https://doi.org/10.1016/j.jnucmat.2018.03.024.

[50] G. Martin, Phase stability under irradiation: Ballistic effects, Phys. Rev. B. 30 (1984) 1424–1436. https://doi.org/10.1103/PhysRevB.30.1424.

[51] S.J. Zinkle, L.L. Snead, Opportunities and limitations for ion beams in radiation effects studies: Bridging critical gaps between charged particle and neutron irradiations, Scr. Mater. 143 (2018) 154–160. https://doi.org/10.1016/j.scriptamat.2017.06.041.

[52] E.D. Eason, C. Services, G.R. Odette, S. Barbara, R.K. Nanstad, O. Ridge, T. Yamamoto, S. Barbara, A Physically Based Correlation of Irradiation-Induced Transition Temperature Shifts for RPV Steels, J. Nucl. Mater. 433 (2013) 240–254. https://doi.org/10.1016/j.jnucmat.2012.09.012.

[53] C. Hofer, E. Stergar, S.A. Maloy, Y.Q. Wang, P. Hosemann, An intermetallic forming steel under radiation for nuclear applications, J. Nucl. Mater. 458 (2015) 361–368. https://doi.org/10.1016/j.jnucmat.2014.12.099.

Chapter 5: Conclusion and Future Work

In this dissertation, ions or neutrons irradiation are conducted in T91, HCM12A, HT9, and Zr-1 %Nb alloys. In ferritic-martensitic alloys, Fe^{2+} or neutrons irradiation were carried out to a dose of 3 dpa at 370 °C and 500 °C while Kr^{2+} or neutron irradiation were executed to a dose of 5 dpa at 310 °C. Atom probe tomography is used to characterize Si-Mn-Ni rich, Cu-rich, Cr-rich, and Nb rich nanoclusters in each alloys after irradiation. Cluster dynamic and NHM model are advanced to simulate irradiation induced Si-Mn-Ni rich nanocluster in F/M alloys, which causes irradiation embrittlement. Validation of the two models with experimental data, make the model a potent tool to predict nanocluster evolution in T91, HCM12A, and HT9 and also to prescribe the required temperature shift for ion irradiation to emulate neutron irradiation.

The major conclusions obtained from this study is:

1. Radiation-induced Nb-rich nanoclusters are present following each irradiation, which could serve as a barrier to irradiation growth. Evidence of solute migration suggests that Nb is redistributed in the matrix upon irradiation, then coalesce into Nb-rich nanoclusters. Finally, in the context of Nb-rich nanoclusters, Kr^{2+} irradiation induces nanoclusters that is similar in size, density, composition, and aspect ratio to those observed following neutron irradiation at similar dose and temperature, suggesting that Kr^{2+} irradiation is a reasonable emulation of neutron irradiation. Simple evaluation of dose rate sensitivity using the invariance theory predicts that only a small temperature shift may be needed for Kr^{2+} to accurately emulate neutron irradiation.

2. Dislocation loops are statistically comparable following both Fe^{2+} or neutron irradiation to 3 dpa at 500 °C, suggesting a requirement for only a small temperature shift as prescribed by the invariance theory.
3. Dislocation loops are observed with Burgers vectors of a<100> and a/2<111>, with each irradiation exhibiting favorability for a<100> oriented loops, consistent with archival literature.
4. Solutes Si, Mn, Ni and Cu exhibit strong evidence of segregation to multiple types of sinks including grain boundaries, dislocation loops, and dislocation lines following irradiations to 3 dpa. However, solutes appear to likely be homogeneously redistributed after Fe^{2+} irradiation to 100 dpa.
5. Si-Mn-Ni-rich and Cu-rich nanoclusters have coarser morphology following Fe^{2+} irradiation than after neutron irradiation, suggesting that the invariance theory is likely insufficient in predicting the temperature shift needed to emulate solute clustering effects with varying dose rates.
6. The cluster dynamics model provides a reasonable prediction of Si-Mn-Ni-rich cluster evolution in T91 under a variety of irradiation conditions, enabling evaluation of sensitivity to different irradiation conditions and potentially predicting temperature shift requirements.
7. The magnitude and direction of temperature shift predicted by cluster dynamic model is consistent with that predicted by NHM model for F/M alloys.
8. The size of Si-Mn-Ni rich and Cu rich nanoclusters increases with increasing temperature while the number density decreases.

9. The nanocluster size and number density following Fe^{2+} irradiation at 370 °C is comparable to the nanocluster morphology after neutron irradiation at 500 °C in F/M alloys. This suggest a negative temperature shift is required to emulate neutron effect in F/M alloys. The temperature shift predicted by the cluster dynamic and NHM models are validated by the experimental data obtained following irradiation of F/M alloys.
10. α' phase does not form due to the short time duration of Fe^{2+} irradiation. The precipitation of Cr rich precipitates does not follow the temperature dilation theory, suggesting that α' phase formation is more time dependent.

We would like to acknowledge the mistake done on our Fe^{2+} irradiation at 370 °C at the Michigan ion laboratory, the sample was left to anneal in the reactor after irradiation experiment, but we believed the anneal condition do not have much impact on the morphology of the irradiation induced nanoclusters and defects. However, another sample of T91, HCM12A, and HT9 have been prepared and sent to Michigan to repeat the Fe^{2+} irradiation at 370 °C.

In the future, we will want to characterize the morphology of the nanoclusters in F/M alloys after Fe^{2+} ions irradiation (3dpa at 500 °C) with and without annealing so as to confirm the thermodynamic stability of the solute's nanoclusters. In addition, it will be beneficial to carry out nano-indentation on T91, HCM12A, and HT9 following Fe^{2+} irradiation to 3 dpa at 500 °C and 370 °C to understand the effect irradiation induced nanoclusters on their mechanical properties.

Appendix A

The output of the data from APT are all in excel file. These files are used for chemical and cluster analysis. The links to the analysis is provided in Table A.

Table A: Summary of the specimens characterized with APT, with links to data files

Alloys	Irradiating Particles	Dose	Irradiation Temperature (°C)	Link to Analysis File
T91	Neutrons	3 dpa	500	N3-500
	Fe^{2+} ions		370	Fe3-370
HCM12A	Fe^{2+} ions	3 dpa	370	Fe3-370
HT9	Fe^{2+} ions	3 dpa	370	Fe3-370
Zr- 1 % Nb	Kr^{2+}	5 dpa	310	Kr5-310
	Neutrons			N5-310